AN INVESTIGATION OF ENHANCEMENT AND RESTORATION OF SUSCEPTIBILITY BASED FEATURES IN AUTOCALIBRATING TYPE ACQUISITION OF SUSCEPTIBILITY-WEIGHTED PARALLEL MRI

SREEKANTH M

Ph.D. THESIS
2020

INDIAN INSTITUTE OF INFORMATION TECHNOLOGY AND MANAGEMENT-KERALA
Thiruvananthapuram

THE SREE CHITRA TIRUNAL INSTITUTE FOR MEDICAL SCIENCE AND TECHNOLOGY, TRIVANDRUM
Thiruvananthapuram

AN INVESTIGATION OF ENHANCEMENT AND RESTORATION OF SUSCEPTIBILITY BASED FEATURES IN AUTOCALIBRATING TYPE ACQUISITION OF SUSCEPTIBILITY-WEIGHTED PARALLEL MRI

A THESIS PRESENTED BY

SREEKANTH M

TO

THE SREE CHITRA TIRUNAL INSTITUTE
FOR
MEDICAL SCIENCE AND TECHNOLOGY, TRIVANDRUM
Thiruvananthapuram

IN PARTIAL FULFILMENT OF THE REQUIREMENTS
FOR THE AWARD OF
DOCTOR OF PHILOSOPHY

2020

CERTIFICATE

I Sreekanth M hereby certify that I had personally carried out the work depicted in the thesis “An investigation of enhancement and restoration of susceptibility based features in autocalibrating type acquisition of susceptibility-weighted parallel MRI”. No part of the thesis has been submitted for the award of any degree or diploma prior to this date.

Sreekanth M

Date:

CERTIFICATE BY GUIDE

Name of the guide : **Dr Joseph Suresh Paul**

Division/Department : Electronics and Computer Science

This is to certify that **Mr.Sreekanth M** in the Department of Electronics and Computer Science, Indian Institute of Information Technology and Management-Kerala, Trivandrum has fulfilled the requirements prescribed for the Ph.D. degree of Sree ChitraTirunal Institute for Medical Science and Technology, Trivandrum.

The thesis entitled "An investigation of enhancement and restoration of susceptibility based features in autocalibrating type acquisition of susceptibility-weighted parallel MRI " was carried out under my direct supervision. No part of this work has been submitted for the award of any other degree or diploma prior to this date.

Signature : 

Date :

CERTIFICATE BY Co-GUIDE

Name of the guide : **Dr C Kesavadas**

Division/Department : Imaging Science and Interventional Radiology

This is to certify that **Mr.Sreekanth M** in the Department of Electronics and Computer Science, Indian Institute of Information Technology and Management-Kerala, Trivandrum has fulfilled the requirements prescribed for the Ph.D. degree of Sree ChitraTirunal Institute for Medical Science and Technology, Trivandrum.

The thesis entitled "An investigation of enhancement and restoration of susceptibility based features in autocalibrating type acquisition of susceptibility-weighted parallel MRI " was carried out under my direct supervision. No part of this work has been submitted for the award of any other degree or diploma prior to this date.

Signature :

Date :

THESIS EVALUATION FORM

The thesis entitled

An investigation of enhancement and restoration of susceptibility based features in autocalibrating type acquisition of susceptibility-weighted parallel MRI

Submitted by

Sreekanth M

for the degree of
Doctor of Philosophy

of

SREE CHITRATIRUNAL INSTITUTE
FOR
MEDICAL SCIENCE AND TECHNOLOGY, TRIVANDRUM
Thiruvananthapuram

Is evaluated and approved by

Name of the Guide

Name of thesis examiner

Acknowledgements

To begin with, I sincerely express my deepest appreciation to my supervisor, Dr. Joseph Suresh Paul for his enduring support and persistent inspiration. The advices and encouragements I received at key moments during the thesis have always been highly appreciated.

I would like to express my sincere gratitude to my co-guide Dr. C Kesavadas who gave me inspirations, advices and support throughout the years of my Ph.D. study.

I thank my doctoral advisory committee members, Dr. Bejoy Thomas and Dr. Ramesh Venkatesan for their valuable guidance and comments.

My sincere thanks to all my friends and colleagues for their support and making my long stay memorable and creating a homely atmosphere away from home.

I acknowledge the various source of financial support during the Ph.D work- Department of Science and Technology, Kerala state planning board and Counsil of scientific and industrial research, Govt. of India.

All of this would not have been possible without the tremendous support from my parents and family who are with me day after day. My heartfelt thanks to my better half Dr. Deepa S V for her support and valuable help in various aspects of my academic and personal life.

And finally, The Almighty, for His choicest blessings that have helped me achieves whatever I could.

Sreekanth M

TABLE OF CONTENTS

LIST OF FIGURES

LIST OF TABLES

LIST OF ABBREVIATIONS

ADMM	Alternating direction method of multiplier
AM	Alternating minimization
BOLD	blood oxygen level depended
CNR	Contrast-to-noise ratio
CSF	Cerebro-spinal fluid
DAI	Diffuse axonal injury
GM	Gray matter
GP	Globus palidus
GRAPPA	Generalized autocalibrating partially parallel acquisition
GRADER	Granularity controlled adaptive edge-preserving regularization
GRE	Gradient Echo
HCSF	Human Contrast Sensitivity Function
HHP	Homodyne high-pass
IR-GRADER regularization	Imaginary-real granularity controlled adaptive edge-preserving
LBV	Laplacian boundary value
mIP	minimum Intensity Projection
MIR	Multi-component imaginary-real
MRA	Magnetic Resonance Angiography
MRI	Magnetic resonance imaging
NLM	Non-Local Means
NMR	Nuclear magnetic resonance
PDF	Projection onto dipole field
pMRI	parallel MRI

PT	Putamen
RF	Radio frequency
SE	Spin Echo
SHARP	Sophisticated harmonic artifact reduction for phase data
SNR	Signal-to-noise ratio
SuR	Susceptibility-related
SVD	Singular value decomposition
SVT	Singular value thresholding
SWAN	Susceptibility weighted angiography
SWI	Susceptibility weighted imaging
TOF	Time –of-Flight
URA	Unity rank approximation
VB-CNR	Vein based CNR
WHP	weighted high-pass
WHPC	Weighted high-pass with compensation
WM	White matter

SYNOPSIS

Susceptibility weighted imaging (SWI) is a Magnetic Resonance Imaging (MRI) method to enhance the susceptibility related contrast attained from a Gradient Echo (GRE) acquisition. To facilitate diagnostic interpretation and improved visualization of susceptibility sources in MRI, SWI uses the intrinsic nature of gradient echo phase images. Unlike other MRI technique where only the signal magnitude are used, the phase and magnitude information are combined to create a new susceptibility weighted magnitude image in SWI. SWI offers information about deoxygenated blood, hemosiderin, ferritin, and calcium which possess different susceptibility than its surrounding structures. Monitoring the susceptibility changes due to iron and mineral deposition benefits the diagnosis of numerous neurologic disorders which includes, stroke, trauma, vascular malformations etc.

However, contrast enhancement is not straight forward as the phase image contains information about the microscopic and macroscopic changes in the magnetic field. To be more specific, the phase image contains components due to inhomogeneity in the main magnetic field, coil sensitivity, global geometry of the object and local field deviation caused by susceptibility changes between tissues. In order to improve the susceptibility related (SuR) contrast in the magnitude SWI, field components other than the local field is to be removed from the phase image. Since the background field contains only low spatial frequency contents, the conventional method to remove the background field uses a homodyne high-pass filter. High-pass filtering to remove the background field is performed by first obtaining a low pass image by truncating the original k-space and zero filling the outside elements. On

dividing the original image with the low pass filtered image, the resultant new image generated will have a high-pass filtered effect. For an image of size 512×512, a window of size 64×64 from the k-space centre is used to create the low-pass filtered image. Using a mapping function, phase mask (susceptibility weighting mask) is created from the high pass filtered phase. This mask is repeatedly multiplied with the original magnitude image to create a contrast enhanced magnitude SWI. Although the contrast improves with number of multiplications, the ensuing noise amplification and resultant reduction in contrast-to-noise ratio (CNR) sets an upper limit on the number of phase mask multiplications. For a better visualization of venous structures, minimum intensity projections of the resultant magnitude SWI images over a minimum of 4 slices are typically used.

Even though SWI processing is technically straight forward, methods to improve the accuracy and quality of the post processing are required. One among the key steps in post processing the phase is the background suppression of the phase images. Traditionally, background fields are removed using homodyne filtering. Besides the advantage of simplicity in implementation without the need of phase unwrapping algorithms, homodyne filter have certain disadvantages. In homodyne, the window size for truncating the central k-space acts as a filter parameter. Since the intrinsic susceptibility component in the phase image is spatially varying, the selection of global filter strength can result in magnitude SWI images with low CNR. Therefore, a filtering method which can automatically control the artifacts and simultaneously increase the CNR of the SWI image is important. Another major issue in SWI processing is the effect of granularities in the background suppressed

phase which becomes critical when the structural contrast needs to be improved by emphasizing the iron carrying regions with a high-pass filter, followed by exponential weighting of the high-pass filtered phase. Apart from these, imperfections in background suppression in regions with low signal-to-noise ratio (SNR) may cause under estimation of local susceptibility distribution and information loss in the magnitude SWI. So a robust method to restore the SuR information in the background suppressed phase is important.

In this thesis, these limitations are addressed through the following objectives

(1) Development of post-processing methods for SWI/SWAN.

(2) Evaluation of a novel filtering method to enhance the clinically relevant features in Susceptibility Weighted Imaging.

(3) Enhancement of susceptibility related features using GRE signal model.

Increasing the contrast between structures with intrinsic susceptibility differences for SWI requires sufficient phase information after suppression of the background field induced phase components. This in turn requires high-resolution acquisition leading to low SNR. The ubiquitous presence of acquisition noise in GRE phase often results in the mis-representation of venous structures. Alternatively, attempts to reduce noise using standard denoising methods result in reduced susceptibility-based contrast due to excessive blurring. In this context, it is highly desirable to develop a denoising filter capable of generating high SNR images with sufficient contrast between regions exhibiting local susceptibility differences.

In contrast to the feature-preserving approaches, our filter works on variational edge-preserving methods which uses local information, namely the image gradients, to preserve edges that bound image features while denoising. One of the key aspects of the proposed method is to adaptively tune the regularization term. The latter often takes the form of a sum of potentials evaluated over the cliques of a neighborhood system, in which the potentials are defined as positive valued, symmetric and continuously differentiable convex functions of the phase differences between the central and neighboring pixels of each clique. A second notable aspect of the current application is that the same potential function also serves as the high-pass filter, with the denoised phase as its input. The inbuilt automatic tuning feature for selection of scale parameter, makes the proposed method for granularity controlled adaptive edge-preserving regularization (GRADER) algorithm a convenient and attractive tool for processing and combining noisy channel images in multi-channel SWI processing pipeline. On processing the real and imaginary components of complex channel images using GRADER results in enhanced SuR contrast of the magnitude SWI, leading to improved visualization of superficial veins and deep gray matter structures.

To emphasize the SuR information for increased blooming and higher CNR it is required to vary the high-pass filter strength spatially. Due to the fixed cut-off frequency of the homodyne filter, there always exist a direct relationship between the filtering artifacts and SuR contrast. In order to introduce a spatially varying filtering effect, we synthesize a set of non-linear weights such that 1) the weight is an increasing function of the phase difference and 2) the weights change more rapidly

with smaller phase differences and more or less saturates to unity as the phase differences become large. This is achieved by using a non-linear function such as the error function, whose magnitude is near to unity for large phase differences. The slope of the weight function decreases with increase in the scale parameter. By adjusting this parameter, it is possible to tune the filter so as to retain maximum possible SuR information by simultaneously reducing the artifacts due to filtering. By weighting the phase differences between the central and the neighboring voxels and summing these across all neighborhood directions, the Weighted High Pass (WHP) filtered phase is obtained. To further increase the CNR noise compensation weights are deduced from the channel phase distribution, conditioned on the channel magnitude and noise variance. Using in vivo SWI data acquired at 1.5 T and 3.0 T, the magnitude SWI processed using the noise compensated WHP (WHPC) filter is shown to provide an average CNR improvement of 68% over that of a homodyne filter.

Although refinements in phase pre-processing have resulted in minimizing the signal errors, it is impossible to recover the lost information without introducing corrections in the signal model. Therefore, a major challenge in SWI is to recover the lost information in regions with high phase wraps and bulk field inhomogeneity. To address this, the predictable components sampled across the echo direction in a multi-echo GRE sequence are recovered by rank minimizing a Hankel matrix formed using the complex exponential of the background suppressed phase in each echo. The voxel-wise signal model can be conceived to be one consisting of a single complex exponential representing the frequency relating to the susceptibility induced field.

Thus by fitting a complex exponential with only a single frequency, it is possible to apply a unity rank approximation (URA) of the structured matrix along the temporal dimension. This is formulated as an optimization problem and implemented using alternating direction method of multiplier (ADMM). Tweaking the signal model after phase pre-processing, enables the visualization of venous structures in the cerebral peduncle and choroid plexus. Due to the bulk field variations introduced by the interpeduncular cistern, these venous structures are usually not enhanced in standard SWI. Additional venous structures between the superior and middle temporal gyrus near to the sinus regions are also seen enhanced in the magnitude SWI using the corrected signal model.

In conclusion, the post processing methods required for enhancement and restoration of SuR features in the parallel MRI is investigated. The granularity controlled edge-preserved denoising method applied to multi-channel SWI data result in denoised high-pass filtered phase without penalizing the resolution of the structural elements. The convergence of the scale parameter to a final steady state value was illustrative of a tuning mechanism for the high-pass filter, required to enhance the true iron carrying structures in the magnitude SWI. To emphasize the local SuR phase information, new high pass filtering scheme is designed for SWI, with spatially varying filter strength. Incorporation of noise compensation weights in the filtering process using prior information about the magnitude intensity and the noise level serves to further improve the CNR and enhances the SuR contrast of magnitude SWI for evaluation of mild cognitive impairments, brain tumor and haemorrhagic stroke. Restoration of the obscured information in the phase due to the

imperfection in the background suppression is made possible by tweaking the signal model and enforcing a unity rank approximation in the multi echo phase signal at each voxel.

CHAPTER 1

INTRODUCTION

1.1 Background of the thesis

Magnetic resonance imaging (MRI) is a non-invasive imaging modality used in clinical radiology that provides structural as well as the functional information of tissues in biological objects. The basic principle behind the MRI is the Nuclear magnetic resonance (NMR) discovered by Felix Bloch and Edward Purcell in 1946 (Abragam and Abragam, 1961). Later in the 1970s, Paul Lauterbur, Raymond Damadian and Richard Ernst develop NMR as medical imaging tool. Since then MRI has advanced tremendously with technology, enabling improvement in image contrast and acquisition speed. With major research efforts, MRI technology has developed the ability to explore the chemical composition, fiber directionality and functional activities of the brain (Brown et al., 2014).

Advancement in technology and development in pulse sequence design enables MRI a popular tool in radiology. Application of high field strength in MRI results in MR images with high resolution. Conventionally, magnitude of the complex signal is used in most of the MR imaging methods to get the tissue contrast. Later, MR scientists and radiologists came to understand that the phase information from pulse sequences like Gradient Echo sequence contains information related to tissue susceptibility (Reichenbach et al., 1997). Since the signal phase in MR acquisition relates directly to the change in field, tissue susceptibility can directly influence the phase values. However the phase images are subjected to artifacts caused by main

magnetic field inhomogeneities and macroscopic susceptibility due to by air-tissue interface, which prevents the direct usage of phase images for clinical application. Later, researchers came to understand that high-pass filtering of measured data can remove the macroscopic fields effect in the MR phase image (Reichenbach et al., 1997). The resultant phase image will have the components only due to the local field deviation. The mineral depositions in tissues and deoxygenated hemoglobin in the blood constitute the local field deviation, representative of the tissue information in the phase image. This filtered phase image can enable contrast improvement of susceptibility-related (SuR) information in the magnitude image through the processing technique popularly known as Susceptibility weighted imaging (SWI) (Haacke et al., 2004).

SWI has extensive clinical applications as a tool for assessing hemorrhages, tumors, stroke, neurodegenerative disorders and cardiovascular physiology. Due to the wide range of clinical applications, there is continuous demand of increase in the quality of SWI. In order to enhance the contributions of susceptibility imaging in clinical radiology, it is required to introduce advances in the processing methods. The nature of the processing steps involved in SWI consist of estimating the local phase from the raw phase image by phase unwrapping, followed by a background suppression method through which the field components due to the main field inhomogeneities and bulk field variation are removed from the phase (Haacke et al., 2004). However, estimation of the local phase due to susceptibility of tissues is no-trivial, due to the constraint of preserving the fine structural details of the phase image. Since the background field contains only low spatial frequency contents, the conventional

method to remove the non-local macroscopic field variations is by using a homodyne filter which filters the low frequency components (Haacke et al., 2004).

Although several modifications of SWI has been proposed in terms of post processing and acquisition technique, the studies have lagged behind certain important aspects of SWI, such as edge preserved denoising for SWI, enhances local susceptibility contrast while reducing filtering artifacts and more importantly restoration of obscured information in the phase image. The aim of this thesis is to address these challenges by modifying the post processing scheme in SWI.

Organization of thesis chapters

This chapter is followed by a chapter devoted to literature review of SWI, and three individual chapters pertaining to methods used, results and discussion of the main contributions of this thesis. Conclusion of this work is included in the last chapter.

Chapter 2: Literature review

A review of the state of the art methods used to enhance the quality of SWI is included in this chapter.

Chapter 3: This chapter covers the development of post-processing methods and algorithms for the enhancement of SWI. The three main contributions of this thesis inclusive of granularity controlled edge preserved denoising of GRE phase image, spatial high-pass filtering with noise compensation and unity rank enforced multi-echo GRE phase processing are described in this chapter.

Chapter 4: Results obtained with the newly developed methods are presented in this chapter.

Chapter 5: Discussion of the significant observations is described in this chapter along with the limitations, future scope and suggestions for other potential applications of this work.

Chapter 6: This chapter presents the summary and conclusions of the study.

1.2 Fundamentals of Magnetic Resonance Imaging

1.2.1 Signal Generation

MRI works on the principle of nuclear magnetic resonance. This relays on the application of magnetic field which causes the nucleus of the atom to resonate. The resonance occurs in the atom due to its spins and angular moment that are determined by a quantity called the spin quantum number (I_s). A non-zero value of the spin quantum number indicates that the nucleus is NMR active. In MRI, the role of Hydrogen atom with a spin quantum number of $\frac{1}{2}$, is considered to be important due to its rich availability in the body. The proton or the nucleus of the hydrogen atom possesses unit positive electric charge and spins about its axis. The spin angular moment can be quantized as

$$\mathbf{S} = \mathbf{I}\hbar. \tag{1.1}$$

where $\hbar = {}^{h}/_{2\pi}$, h is the Plank constant, $|\mathbf{I}| = \hbar\sqrt{I_s(I_s+1)}$ and I_s is the spin quantum number.The number of possible states of the nuclear magnetic moment can be determined from the spin quantum number as $2I_s + 1$. For a proton with spin number $\frac{1}{2}$, the possible spin orientation corresponds to $-\frac{1}{2}$ and $+\frac{1}{2}$. Due to the non-zero spin of the nucleus, a magnetic dipole moment (μ), is created and can be expressed as

$$\mu = \gamma\mathbf{S} \tag{1.2}$$

where, $\gamma = 2\pi \times 42.57$ Mhz/T is the gyromagnetic ratio. Since the applied field B_0 is in the z-direction, the discrete energy levels of the spin in the z-direction is defined as

$$E = \pm\frac{1}{2}\gamma\hbar B_0 \tag{1.3}$$

This defines the existence of two discrete energy levels of the proton which aligns both parallel and anti-parallel in the quantum model with an energy difference $\Delta E = \gamma\hbar B_0$. Here the one which align in parallel corresponds to the lower energy state. Since the lower energy state has more protons, there exists a small field that aligns parallel to the applied field. This macroscopic field generated due to nuclear magnetism while applying a static field, is considered as the bulk magnetization $\overline{M}$. This magnetization will induce a torque on the spin angular moment**,** resulting in rotational motion known as precession. The frequency of precession termed as the Larmor frequency(ω_0), is given by

$$\omega_0 = \gamma B_0 \tag{1.4}$$

1.2.2 Magnetic Fields in MRI

In addition to the large external static field B_0, there are three gradient fields G_x, $G_y$and G_z, and a radio frequency (RF) excitation field B_1. Superconducting magnets or permanent magnets are used to create a homogeneous static magnetic field B_0. A human MR scanner is designed to have a cylindrical bore and placed horizontally. The applied magnetic field direction is horizontal and parallel to the bore. In the Euclidean coordinate system, y direction is vertically upward, and the magnetic field along the horizontally placed bore is the z -direction. The direction of x is

perpendicular to both y and z direction. The magnetic field $B(r)$ after superimposing the static filed B_0 with the gradient field at each location r can be given by

$$B(r) = B_0 + \boldsymbol{G}.r, \tag{1.5}$$

where, $\boldsymbol{G} = G_x + G_y + G_z$. Since the precessions of magnetic moment are of random phase, the net transverse component of $\bar{M}$ is zero. As mentioned earlier, when an external field is applied, the magnetic moment precesses about the direction of the applied field. Upon application of an external RF pulse B_1 with a frequency equivalent to Larmor frequency, a transverse component of $\bar{M}$ is generated due to the transfer of energy to the magnetic spins. In summary, a transverse field is observed after flipping the longitudinal magnetization using an RF pulse or excitation pulse. The flip angle is set by the energy of the RF pulse.

1.2.3 Free Precession and Relaxation

Once the excitation pulse is removed, the transverse field has a tendency to relax and return to equilibrium state. This will result in a phenomenon called free precession, where the $\bar{M}$ precesses around the B_0 field, so as to reach the equilibrium state. The longitudinal component M_z gains strength due to longitudinal relaxation and the transverse component M_{xy} simultaneously loses its strength due to transverse relaxation (Bottomley et al., 1984). The mathematical equations for longitudinal and transverse relaxation are given by

$$M_z(t) = M_{z,0}\left(1 - exp\left(\frac{-t}{T_1}\right)\right) + M_z(0_+)\exp\left(\frac{-t}{T_1}\right) \tag{1.6}$$

$$M_{xy} = M_{xy}(0_+)e^{-t/T_2}, \tag{1.7}$$

where $M_{z,0}$is the longitudinal magnetization before excitation,$M_{xy}(0_+)$ and $M_z(0_+)$ are the transverse and longitudinal relaxation immediately after $t = 0$, T_1 and T_2 represent the longitudinal and transverse relaxation time constants, respectively. In general, the transverse relaxation rate is more when compared to the longitudinal relaxation. As illustrated in Fig. 1.1, the relaxation time constants$T_1$and T_2can be defined as the time taken by $M_z$to regain 63% of the longitudinal magnetization before excitation, and the time for M_{xy} to drop 63% of the initial transverse magnetization after excitation. Besides that due to tissue susceptibility, presence of magnetic field inhomogeneites causes additional dephasing with time constant T_2'. This is usually combined with T_2 to form T_2^* relaxation, as given by

$$\frac{1}{T_2^*} = \frac{1}{T_2} + \frac{1}{T_2'} \tag{1.8}$$

The Bloch equation describes the relationship between the change in magnetization and time. According to Bloch equation the $\overline{M}$ in the presence of field B which includes the static field B_0 and the excitation field B_1 is given by

$$\frac{dM}{dt} = \gamma \bar{M} \times B - \frac{M_x\hat{x} + M_y\hat{y}}{T_2} - \frac{(M_z - M_{z,0})\hat{z}}{T_1}, \tag{1.9}$$

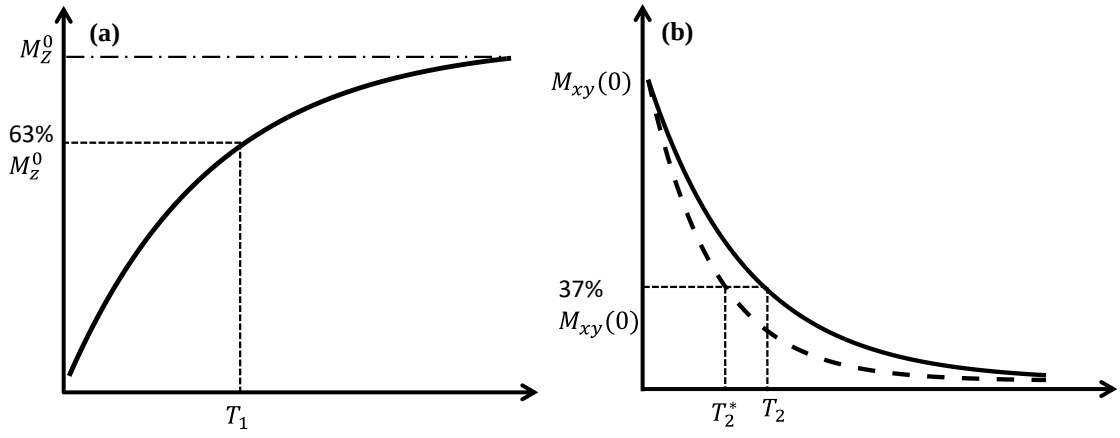

Fig.1.1: Relaxation time profile (a) T_1relaxation (b) T_2 and T_2^* relaxation.

where, $\hat{x}$, $\hat{y}$, $\hat{z}$ denote the Cartesian coordinates.The components of Bloch equation in Cartesian coordinates are

$$\begin{aligned}\frac{dM_x}{dt} &= -\gamma\left(B_y M_z - M_y B_z\right) - M_x/T_2 \\ \frac{dM_y}{dt} &= -\gamma(B_z M_x - M_z B_x) - M_y/T_2 \\ \frac{dM_z}{dt} &= -\gamma\left(B_x M_y - M_x B_y\right) - (M_0 - M_z)/T_1\end{aligned} \tag{1.10}$$

The solution of the above equation approaches to precession of M in the direction of field B. On assuming $T_2 = T_1 \to \infty$ and $B = \hat{z}B_0$ be the magnetic field along z axis, the magnetization can be written as

$$\frac{dM}{dt} = \gamma B_0(\hat{x}M_y - \hat{y}M_x). \tag{1.11}$$

When M is not align in the z direction, the solution for Bloch equation can be expressed as

$$M_x + jM_y = \left[M_x(0) + jM_y(0)\right]e^{-j\omega_0 t} \tag{1.12}$$

$$M_z = M_z(0) \tag{1.13}$$

where, $M_x + jM_y$ is the complex transverse component rotating at angular velocity of ω_0 in the xy-plane. If there is relaxation rate, the solution of Bloch equation can be written as

$$M_x + jM_y = \left[M_x(0) + jM_y(0)\right]e^{-j\omega_0 t}e^{-t/T_2} \tag{1.14}$$

$$M_z = M_0 + [M_z(0) - M_0]e^{-t/T_1} \tag{1.15}$$

While the transverse component rotates about the main magnetic field direction, its magnitude decays exponentially with time. Whereas the longitudinal magnetization gains strength and reaches the equilibrium value of M_0.

1.2.4 Detection of MRI signal

Signal detection using coils is governed by the law of electromagnetic induction and principle of reciprocity (Hoult and Chen, 1989, Hinshaw and Lent, 1983). The change in magnetic field due to precession of bulk magnetization induces a voltage in the conducting loop placed orthogonal to the magnetic field direction. The signal generated in the receiver coil is given by

$$S(t) = \frac{\partial \Phi(t)}{\partial t} = -\frac{\partial}{\partial t}\int_{object} \bar{C}(r) \cdot \bar{M}(r,t)dr\,, \tag{1.16}$$

where $\Phi(t)$ be the magnetic flux, $C(r)$ is the coil sensitivity at location r and $M(r)$is the magnetic field.

1.2.5 Spatial Encoding

MRI signal received in receiver coil contains sum of signal generated from the whole imaging object in relation to its spin density. Therefore, a spatial encoding is required to obtain localized information about the spin density. In MRI, this is achieved by field gradients generated using gradient coils (Kumar et al., 1975). As shown in Fig. 1.2, there are three gradients coils G_x, G_y, and G_z that corresponds to x −direction, y −direction and z −direction. In terms of the three field gradients, the magnetic field $\bar{B}$ and resonance frequency ω can be expressed as

$$\bar{B} = \big(B_0 + (G_x x + G_y y + G_z z)\big)\bar{k} \tag{1.17}$$

$$\omega(z,y,z) = \omega_0 + \gamma\big(G_x x + G_y y + G_z z\big) \tag{1.18}$$

Slice Selection

Slice selection generally involves selection of a particular region with pre-determined thickness that has to be imaged. A shaped RF pulse with frequency ω_{rf} and a gradient field are commonly used to select the slice by exciting only the spins

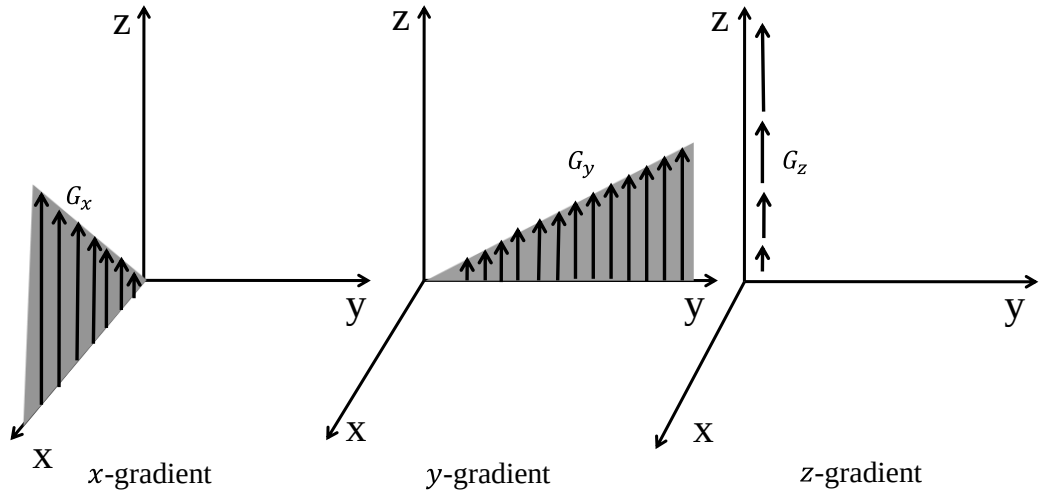

Fig.1.2: The gradient fields G_x, G_y and G_z along x, y and z direction.

in the region of interest as shown in Fig. 1.3. By spatially adjusting the resonance frequency, the excitation pulse becomes selective with respect to the position. This is made possible at the time of RF pulse. On excitation, only the spins which are in the slice $z_s = (\omega_{rf} - \omega_0)/\gamma G_z$ and having resonance frequency $\omega_{rf} = \omega_0 + \gamma G_z z_s$ are excited. The thickness of the slice Δz is controlled by the RF pulse through the relation $\Delta z = \Delta\omega/\gamma G_z$, where $\Delta\omega$ represents the bandwidth of excitation pulse.

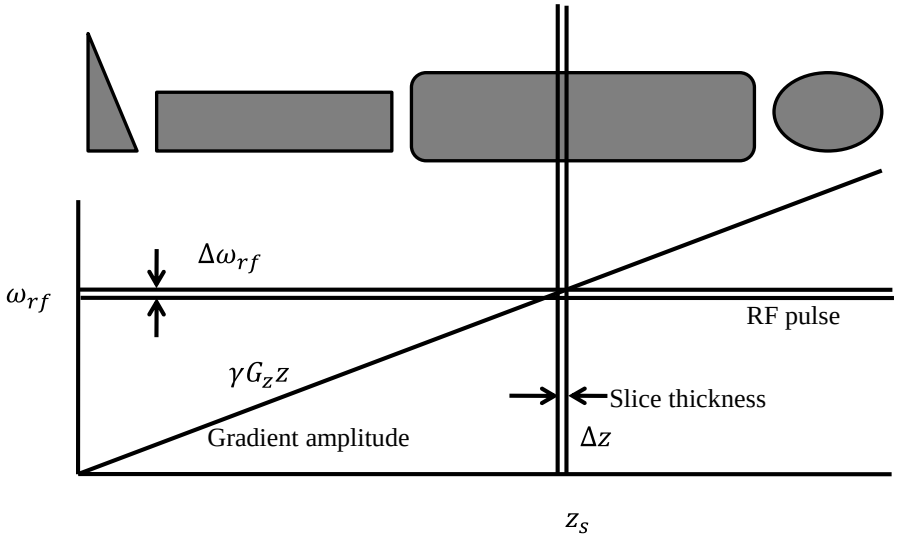

Fig.1.3: Slice selection enabled by gradient G_z and RF pulse ω_{rf}

Frequency Encoding

The frequency encoding gradients traditionally makes the MR signal position dependent based on the frequency. With the x-gradient turned on, the resonance frequency at position x is given by

$$\omega(x) = \omega_0 + \gamma G_x x \tag{1.19}$$

On applying the frequency encoding gradient, the detected signal in the coil due to transverse field is

$$S(t) = \left[\int_{object} C_{xy}\rho(x)e^{-\gamma G_x xt}\right] e^{-i\omega_0 t} \tag{1.20}$$

After removal of RF frequency components, the baseband detected signal takes the form

$$S(t) = \int_{object} C_{xy}\rho(x)e^{-\gamma G_x xt}\, dx \tag{1.21}$$

Phase Encoding

Similar to the function of frequency encoding gradients, phase encoding gradients makes the signal phase position depended. By turning on the phase encoding G_y for duration of T_{pe}, the signal received in 1D acquisition can be represented as

$$dS(y,t) = \rho(y)e^{-i\gamma G_y y T_{pe}} e^{-i\gamma B_0 t} \;\; for t > T_{pe} \tag{1.22}$$

Thus the phase encoding is made possible by applying a linear phase gradient, so that at each position, the received signals have different phase.

The spatially encoded received signal can be represented as

$$S(t) = \int_{object} C_{xy}(x,y)\,\rho(x,y)e^{-\gamma\left(G_x xt + G_y y T_{pe}\right)} dx\, dy \tag{1.23}$$

1.3 Generation of k-space

K-space is the space where the measured signal in Fourier domain is encoded using the spatial encoding gradient. The spatial frequency information of the imaging

object is represented in k-space. In general, the k-space and image data can be related with a Fourier transform operation. Each location in the k-space is related to the encoding gradients being applied (Liang and Lauterbur, 2000). For each G_y, one row is filled in the k-space with varying G_x. The signal received in the receiver coils is proportional to the sum of signals from all the excited spins generated by the excitation pulse. The k-space signal is expressed as

$$S(t) = \int_v M(r,t) e^{-i\Delta\phi(r,t)} d^3 r \,, \tag{1.24}$$

where $\Delta\phi(r,t) = -\gamma \int_0^t \Delta B(r,\tau) d\tau$ is the phase accumulated due to the gradient field at each position r and time t, ΔB represents the change in magnetic field and τ is the time duration of applied field. On the assumption that at position r, the field inhomogeneities are lower than the encoding gradients,

$$\Delta\phi(r,t) = k(t).r, \tag{1.25}$$

where $k(t) = -\gamma \int_0^t G(\tau)\, d\tau$. K-space positions can be defined in terms of the spatial encoding parameters, so as to determine the spatial frequencies k_x along frequency encoding direction and k_y along phase encoding.

$$k_x = \frac{\gamma G_x \tau}{2\pi} \tag{1.26}$$

$$k_y = \gamma G_y T_{pe}/2\pi \tag{1.27}$$

With this representation, Fourier approximation can be used to express the k-space signal as an invertible function of the spatial frequencies. Using Fourier approximation, the signal generated at the position (k_x, k_y) can be expressed as

$$S(k_x, k_y) = \iint_{x,y} C_{xy}(x,y)\rho(x,y) e^{-i2\pi(k_x x + k_y y)} dx dy \tag{1.28}$$

1.4 MRI pulse sequence

To acquire the desired signals in k-space, it is required to suitably design the RF pulse and time duration for the application of encoding gradients. The sequence of arrangement of excitation and encoding gradients along with signal sampling is called a pulse sequence. The two most commonly encountered pulse sequences are the Spin Echo (SE) and the Gradient Echo (GRE) sequence (Edelstein and Bottomley, 1984, Vlaardingerbroek and Boer, 2013).

1.4.1 Spin Echo sequence

In a SE sequence, a 90° pulse is first used to obtain a transverse magnetization by flipping magnetization into the x-y plane. The excitation pulse is designed so as to excite only a pre-determined cross section of the imaging object. This is made possible by introducing a slice selection gradient which increases the precessional frequency along the slice encoding direction. Depending on the frequency of excitation pulse, a cross section of the imaging object is excited. This will generate transverse magnetization in the x-y plane. Due to T_2 relaxation caused by spin-spin interaction, the transverse magnetization starts dephasing. Another RF pulse is used to refocus the dephasing magnetization with a 180° flip. This causes a rephasing of the dephasing transverse magnetization. The magnetization will recover completely and an echo will be produced after a time delay which is same as that of the time between the initial RF pulse and the refocusing pulse. The time period between the excitation pulse and time at which the rephasing is completed is called echo time (TE). The signal is measured at this time by application of a readout gradient G_x. Before the next excitation, a time delay has to be given to restore the equilibrium state. This time delay is called repetition time (TR). The magnitude of the

longitudinal magnetization is therefore dependent on TR and can be used to alter the contrast of MR image. The same steps are repeated for another value of $G_y$till the whole k-space is measured. The pulse sequence diagram is shown in Fig. 1.4.

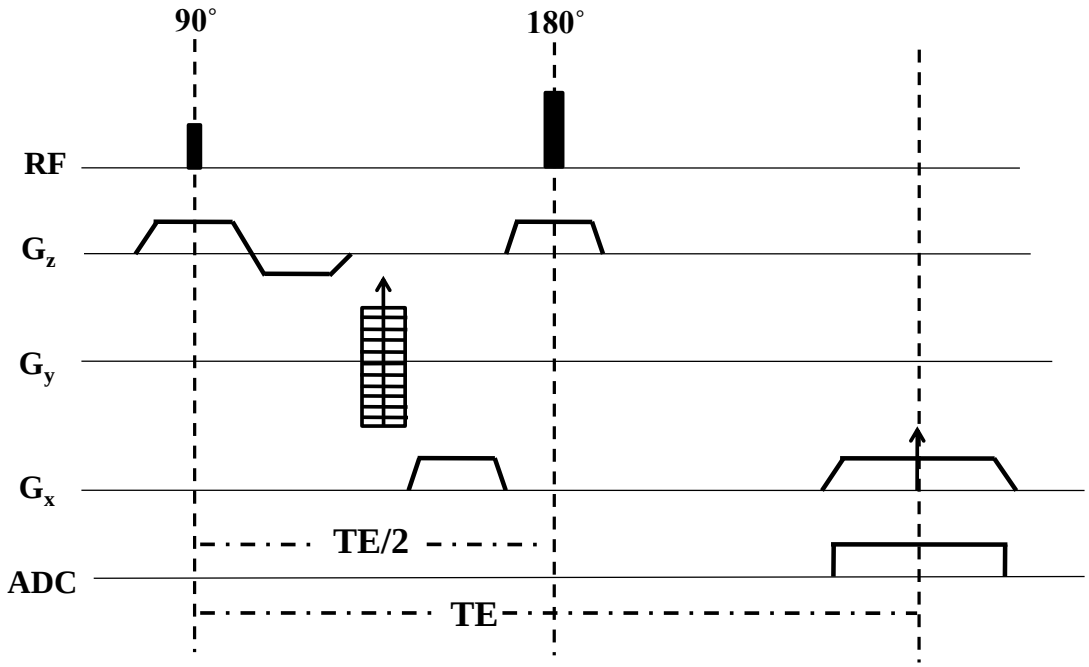

Fig. 1.4: Pulse sequence diagram for a SE sequence

1.4.2Gradient Echo pulse sequence

One primary difference between SE and GRE sequence is that, in GRE sequence, gradient fields are used to rephase the magnetization unlike in SE sequences where a 180° RF pulse is used. As in the SE sequence, an excitation pulse should be applied initially to flip the field component into the x-y plane. But in GRE sequence, the flip angle can be less than 90° which allows a shorter TR and reduced acquisition time. Once the magnetization starts dephasing after excitation, phase coherence is achieved by gradient reversal, resulting in echo generation. The Fig. 1.5 shows the pulse sequence diagram for GRE sequence.

Due to the absence of 180° pulse, a shorter TE is possible in GRE sequence. However, the inhomogeneity in the B_0 affect the signal decays in GRE acquisition. These inhomogeneities cause additional dephasing of the spins in a voxel. This constitutes one type of susceptibility induced off resonance effect. The combined effect of T_2 decay and the decay due to off resonance is defined as T_2^* decay. Due to additional dephasing, the T_2^* decay is faster than the T_2 decay. Therefore the TE of the GRE sequence is generally set to a low value to avoid signal loss. With the development of superconducting systems to produce homogeneous magnetic field and the understanding of using shorter TE to reduce artifacts in the magnitude image makes the GRE acquisition a possible tool to obtain the T_2^* weighted images.

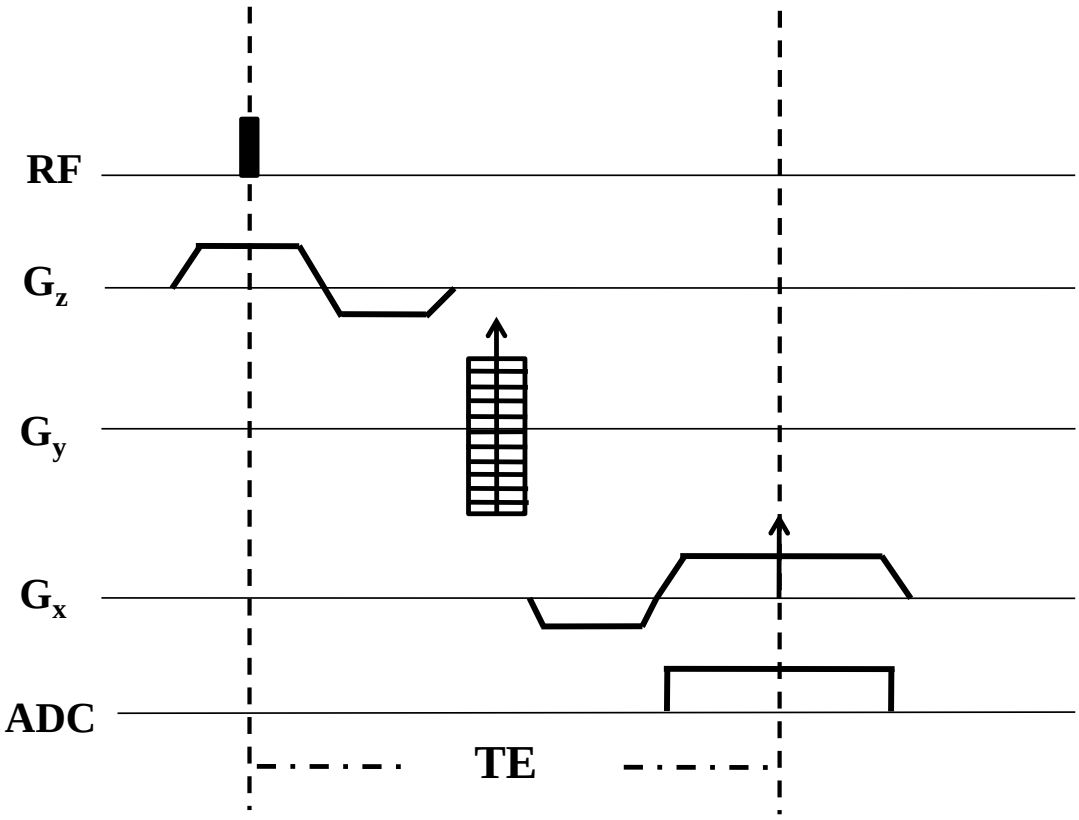

Fig. 1.5: Pulse sequence diagram for a GRE sequence

1.5 GRE acquisition and MR phase image

The sensitivity of the GRE phase image to susceptibility sources has triggered the study related to application of MR phase image in stroke, tumor and neurodegenerative diseases. It is reported that compared to the T_2^* magnitude image the phase image shows an average of seven times contrast improvement between the white and gray matter region, (Hammond et al., 2008, Duyn et al., 2007). This shows the potential of the phase image to reveal more clinical information from the MR magnitude images. Hence it is important to highlight the origin of phase components and explore its relation to susceptibility.

1.5.1 Basics of Electromagnetism

The spatial variation of magnetic field introduces the phase in GRE data. In order to study the effect of susceptibility in the phase image, a basic knowledge of the electromagnetism is required. One of the primary terms that is often encountered in electromagnetism is the magnetic field intensity (H). It is the field produced by the external source. On applying an external field, the subject will induce its own field due to magnetization. The resultant magnetic flux density (B) whose unit is Tesla (T) is proportional to both the sum of both magnetic flux density and induced magnetization M.

$$B = \mu(H + M) \tag{1.29}$$

where, μ is the permeability (H/m) and $M = \chi H$, χ is the susceptibility. The permeability of free space $\mu_0 = 4\pi \times 10^{-7}$that relates to B and H can be represented as

$$B = \mu_0 H \tag{1.30}$$

The ratio between the permeability of the object μ in the magnetic field and permeability of the free spaceμ_0 is called relative permeability μ_r, defined as

$$\mu_r = \frac{\mu}{\mu_0} \tag{1.31}$$

Based on the relative permeability, the materials are categorised basically into three types: diamagnetic, paramagnetic and ferromagnetic.

Materials with relative permeability $\mu_r < 1$ are called diamagnetic materials. In these materials, the induced bulk magnetization aligns in the opposite direction to the external field. Paramagnetic materials are those with relative permeability $\mu_r > 1$. The unpaired electrons in the atoms of these materials exhibit a permanent magnetic moment. When an external magnetic field is applied, a bulk magnetization will produce and the magnetic moments will align according to external field. Paramagnetism is considered to have high strength when compared with the diamagnetism. However, the effect of paramagnetism is negligible in the case with paired electrons.

The ferromagnetic materials are those materials with relative permeability much greater than 1. Irrespective of external field, materials like iron, exhibit a high magnetic moment. On application of magnetic field the magnetic moment will align with external field and result in strong magnetic field.

1.6 Generation of MR phase image

Since a major component of the tissues in brain consists of water that is diamagnetic with susceptibility of -9.05×10^{-6} at body temperature, brain tissues are also diamagnetic with susceptibility values ranging between -11.0×10^{-6} to -7.0×10^{-6} (Schenck, 1996). Increase in concentration of paramagnetic substances in the tissues can alter diamagnetic property in brain tissues and can introduce strong paramagnetic

effect, resulting in additional contrast in the phase image. An example is the contrast between brain tissues and venous structures. Due to deoxyhaemoglobin which is paramagnetic with a susceptibility of 0.15×10^{-6}, deoxygenated blood can be attributed to a paramagnetic source. This causes an increase in the B_0 field in the venous location, resulting in a phase with higher positive value than the surrounding tissues in left handed type scanners. This leads to higher contrast between other tissues and venous structures. Even though the change in susceptibility between venous structures and its parenchyma are relatively small, it is enough to bring sufficient contrast so as to distinguish the venous structures in the phase image (Duyn et al., 2007).

The complex signal ρ received in a right handed system using a short TR GRE sequence is given by

$$\rho = \rho_m exp(-i\gamma\Delta BTE) \tag{1.32}$$

where, ρ_m is the magnitude of the signal and ΔB is the change in field due to susceptibility of the tissues. Then the above Eq.32 can be modified as

$$\rho = \rho_m exp(-i\gamma g\Delta\chi B_0 TE), \tag{1.33}$$

where, g is the geometric factor and $\Delta\chi$ is the local susceptibility difference in the tissue. From the relation of Larmor frequency $\omega = \gamma B_0$, the phase can be represented as

$$\varphi = \omega t \tag{1.34}$$

For a period of time TE, the change in phase for different tissues is given by

$$\Delta\varphi = \Delta\omega TE \tag{1.35}$$

On substituting the relation between $\Delta\chi$ and $\Delta\omega$ in the above equation, the change in phase can be expressed as

$$\Delta\varphi = -\gamma g \Delta\chi B_0 TE \tag{1.36}$$

This indicates that phase change have a direct relation to the change in susceptibility which in effect changes the magnetic field at that location.

The phase term is introduced in the measured complex signal by the spatially varying B_0. Three major causes of B_0 variation is the inhomogeneity in the B_0 itself, susceptibility effect of the tissues and other components, and the chemical shift. Imaging the phase angle of measured complex signal from MRI of brain does not show any structural resemblance with the brain since the phase image contains components due to the main field inhomogeneity, chemical shift, global geometry of the object and local field deviation caused by susceptibility changes between tissues. Without any form of post processing, the phase image shows only the B_0 field inhomogeneities and wrapping artifacts that exhibit sharp intensity changes in the range of $[-\pi, \pi]$. After phase unwrapping, background suppression is performed to obtain phase components due to tissues alone. Since the slow varying frequency changes in the phase is mainly contributed from field inhomogeneities, coil sensitivity and global geometry of the object, phase obtained after background suppression reveals the high frequency variations due to the intrinsic susceptibility changes between tissues. Owing to the induced magnetization, the change in susceptibility values causes changes in B_0 field at the sub-voxel level. This results in spatial phase variation across the brain.

Several studies demonstrated that magnetic susceptibility of biological tissues at each voxel is not the only factor which controls the phase intensities of the MR images at that voxel (Duyn et al., 2007, Zhong et al., 2008). As per the law of magnetism, induced magnetic field shows a dipole field pattern which extends beyond the

susceptibility source. Therefore, phase intensity at each location is determined not only from the susceptibility of tissues within the voxel but also from the near-by sources. This results in a non-zero phase at locations with no significant susceptibility sources. The orientation and shape of the imaging object also affect the contrast of the phase image. In a high resolution acquisition, those venous structures which are at an angle of 90° with respect to the field has an opposite sign to the value of vein that are aligned in the same direction to the applied field (Liu et al., 2014). Moreover, those veins which, makes an orientation equal to the magic angle, exhibit no effect on the phase image. This causes reduced contrast of structural information in the phase image. This shows the limitation of phase to enhance the structures at different orientation.

1.7 Reconstruction of local phase

Visualization of structural information in the phase image generated from the MRI data requires removal of background field information in the phase data. The range of phase values of these components often go beyond 2π, which will wrap around in the $[-\pi, \pi]$causing phase wrapping artifacts. This necessitates the need for phase unwrapping procedure followed by background suppression for removal of low frequency components to create a phase image which exhibits structural details as shown in Fig. 1.6 (Jenkinson, 2003, Song et al., 1995, Li et al., 2014b, Zhou et al., 2009).

A common method to reconstruct the high frequency local phase image is the homodyne high-pass filtering method (Noll et al., 1991, Wang et al., 2000).

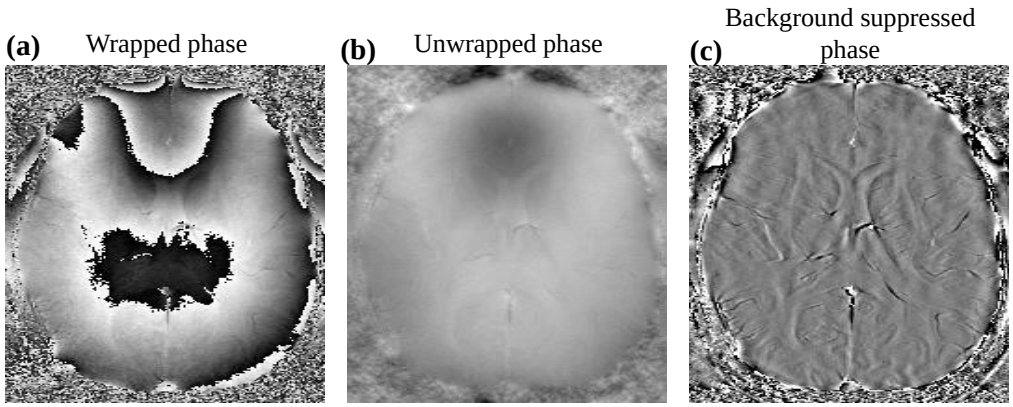

Fig. 1.6: Left to right panel show the wrapped phase, unwrapped phase and the phase obtained after background suppression.

Homodyne filtering method recovers the high-frequency components in the phase without the need for a separate phase unwrapping step. In homodyne filtering, the measured image is divided by a low pass filtered form of the original complex image to obtain an image with high-pass filtered effect. To create the low-pass filtered image of the same size as the original image, a small window is chosen at the central k-space, with the outer k-space locations filled with zeros. Dividing the original image with this low pass filtered image will result in an image with high-pass filtered effect (Haacke et al., 2009, Liu et al., 2017). Here, the window size for truncating the central k-space acts as a filter parameter. A main drawback of homodyne filtering is that while using a low filtering strength the phase wraps retains and when the filtering strength is too high, information about faint venous structures will be lost.

To circumvent this problem, more sophisticated algorithms were developed for phase unwrapping and minimizing information loss using refinements in background suppression methods. Unlike the homodyne filtering method, the phase unwrapping algorithms remove phase wraps in the spatial domain to estimate the true phase. Incorrect estimation of the true phase may lead to streaking artifacts in the phase

image. Algorithms like Laplacian based fast unwrapping (Li et al., 2014b), Goldstein (Goldstein et al., 1988) and PRELUDE (Jenkinson, 2003)are increasingly gaining attention. Followed by phase unwrapping, background suppression is performed. Of late, algorithms such as the sophisticated harmonic artifact reduction for phase data (SHARP) (Schweser et al., 2010), projection onto dipole field (PDF) (Liu et al., 2011a)and Laplacian boundary value (LBV) (Zhou et al., 2014) methods have been applied for background fields removal.

1.8 Susceptibility Weighted Imaging (SWI)

SWI is a method to increase the SuR contrast in the magnitude image by utilizing the phase information obtained from GRE acquisition. Originally developed by Haacke et al. (Haacke et al., 2004), SWI gives information about the tissue susceptibility by enhancing the image contrast for the tissues with a different susceptibility as compared to its surrounding. Data for SWI processing was conventionally acquired using flow compensated 3D GRE sequence. Since a SE sequence uses an 180˚ RF pulse to rephase the T_2^* effect, it cannot be used for generating SWI. In the case of GRE acquisition, field gradients are used to refocus the spins.

1.8.1 SWI pulse sequence

The GRE sequence forms the basic framework for SWI data acquisition. This is because in GRE, the local susceptibility effect causes T_2^* relaxation that modulates the contrast of both magnitude and phase image. SWI sequence generally uses a 3D GRE sequence since it provides high resolution than the 2D GRE sequence. Due to 3D acquisition, an additional slice selection gradient is required. A flip angle is set such that the signal intensity of cerebro-spinal fluid (CSF) is more than the surrounding white matter and gray matter. This will result in a flat contrast between

the tissues and CSF in the magnitude image. The pulse sequence diagram is shown in Fig.1.7.

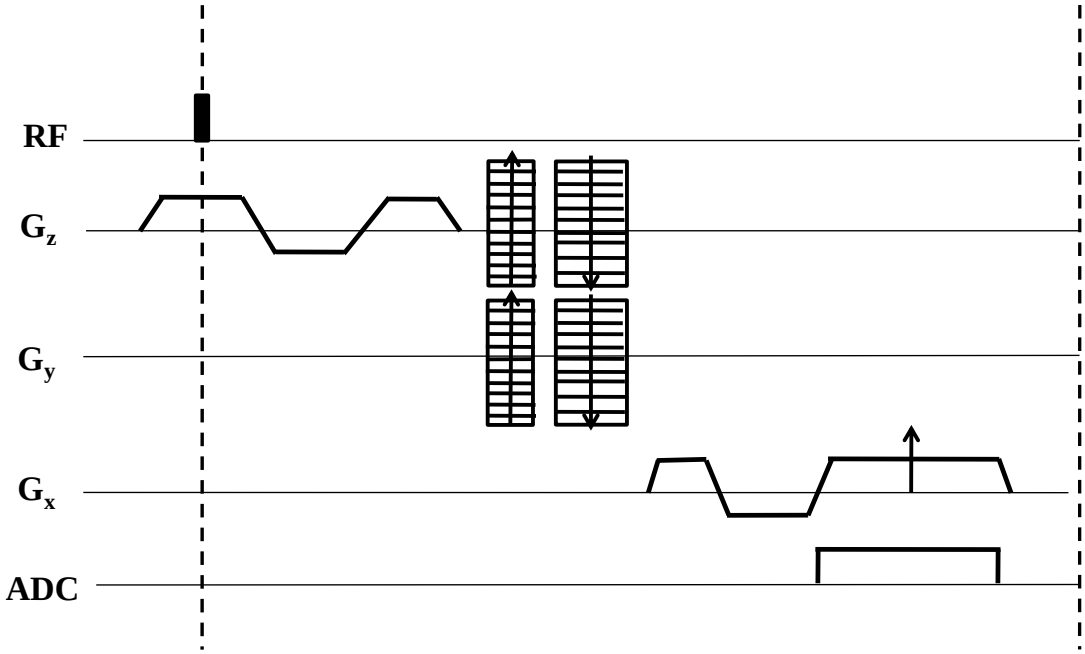

Fig. 1.7 pulse sequence diagram for 3D GRE

Since SWI is used to visualize the susceptibility changes between tissues, the phase accumulated due to rapid flow of blood must be compensated. This is accomplished using flow compensation gradients applied in all the spatial encoding directions of the 3D GRE sequence. Due to the flow compensation gradients, protons in the fast flowing blood will induce additional phase which the encoding gradients cannot refocus.

The conventional SWI uses the homodyne filtering to obtain the filtered phase image. As the filtered phase represents the local field variation due to intrinsic susceptibility changes, it is used to increase the SuR contrast in magnitude image for differentiating tissues with different susceptibility. This is accomplished using a susceptibility mask or phase mask, generated from the pre-processed phase using a mapping function. The phase masks are designed in such a way that its value range from 0 to 1. The

phase mask value is set to unity at those locations where the there are no significant changes in susceptibility such as the gray matter or ventricles. In regions with significant susceptibility differences from the background, the phase mask is set to a value between 0 and 1 to attenuate the signal intensity. The amount of attenuation signifies the relative change in susceptibility with respect to the background regions. If the phase of interest is positive in a left handed system, the phase mask is generated such that it linearly scale the phase values in the range$[0, \pi]$.

$$\mathcal{W}(r) = \begin{cases} \frac{(\pi - \varphi(r))}{\pi} & for \quad \varphi(r) \geq 0 \\ 1 & \varphi(r) < 0 \end{cases} \tag{1.37}$$

where$w(r)$ is the value of phase mask at location $r$and φ is the filtered phase. Similarlyfor right handed system, the phase mask is obtained as

$$\mathcal{W}(r) = \begin{cases} \frac{(\pi + \varphi(r))}{\pi} & for \quad \varphi(r) \leq 0 \\ 1 & \varphi(r) > 0 \end{cases} \tag{1.38}$$

The generated phase mask is multiplied with the original magnitude image $\rho_m(r)$at each position to generate an image with higher contrast than the actual one. This is given by (Haacke et al., 2004)

$$\bar{\bar{\rho}}_m(r) = \mathcal{W}^{\Gamma}(r)\rho_m(r), \tag{1.39}$$

where$\Gamma$is the contrast paremeter, and $\bar{\bar{\rho}}_m$is called the magnitude SWI. For better visualization of venous structures, minimum Intensity Projection (mIP) of the resultant magnitude SWI images are computed using a minimum of 4 slices. Images obtained at various stages of the SWI processing pipeline is shown in Fig.1.8.

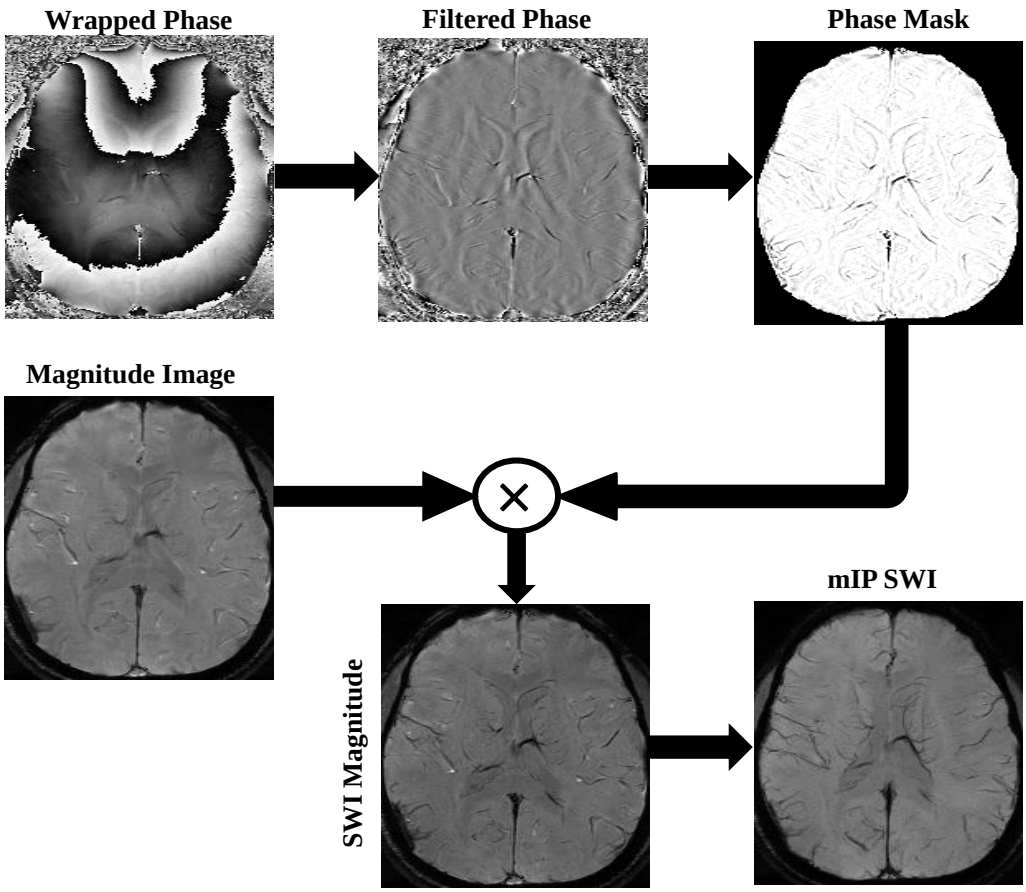

Fig.1.8: SWI processing pipeline

As the effect of T_2^* relaxation on the magnitude image can be reduced by using small voxel size a high resolution acquisition is usually preferred in SWI. Moreover, a high resolution acquisition reduces the partial volume effect and preserves the local phase offset contrast. Higher acquisition time is the major disadvantage of high resolution imaging. To shorten the scanning time, parallel imaging techniques such as SENSE (Pruessmann et al., 1999) and generalized autocalibrating partially parallel acquisition (GRAPPA) (Griswold et al., 2002) are usually employed. These techniques enable acquisition of k-space with reduced number of samples by reducing the number the phase encoding lines that essentially determines the

acquisition time. Using the samples acquired along phase encoded lines the neighboring unacquired samples are estimated using regression techniques to generate an artifact free image. However, undersampling and high-resolution acquisition causes reduction of signal-to-noise ratio (SNR) in the final image. As the SNR increases with increase in field strength, high field strengths are preferred in SWI. This is also a blessing in disguise as the susceptibility effects will get enhanced at higher field strengths.

Since the phase in MR signal is directly related to the change in susceptibility and TE as in Eq. 1.36, GRE sequence with longer TE are generally used for SWI. This helps to accumulate sufficient phase offset between tissues. For example, the susceptibility difference between the veins and its surrounding parenchyma is usually of the order of 10 ppm. By using a long TE, phase intensity of venous structure and the surrounding tissue will vary considerably to obtain sufficient contrast in the phase image. Even though long TE has the advantage of enhancing the susceptibility effects of the tissues in the phase image, reduction in SNR is a major problem of concern. Secondly, structures with high susceptibility values may mask the neighboring tissues with relatively low susceptibility. More importantly, at long TE, the phase images exhibit wrapping artifacts. Post processing steps are usually required to remove these wraps and recover the useful phase information.

1.9 Challenges in SWI

Even though SWI processing is technically straight forward, techniques to revamp the quality of the images are required. One among the key steps in post processing is the background suppression of the phase images. Traditionally, background fields are

removed using homodyne filtering. Besides the advantage of simplicity in implementation without the need of phase unwrapping algorithms, homodyne filter have certain disadvantages. In homodyne, the window size for truncating the central k-space acts as the filter parameter. Since the intrinsic susceptibility component in the phase image is spatially varying, the selection of global filter strength can result in loss of phase information and low contrast-to-noise ratio (CNR) in magnitude SWI. Moreover, the selection of filter strength is empirical. A selection of small filter strength will cause the retention of background field inhomogenities in the filtered phase image while a too large filter will remove useful local field deviations due to susceptibility from the phase images. Therefore, a filtering method which can automatically control the artifacts and simultaneously increase the CNR of SWI image is important.

The SWI processing aims to increase the contrast of structures like veins and other regions with mineral deposition in the absolute image without any phase artiftact. But the measurement noise in GRE phase causes CNR reduction, especially when the phase mask multiplication increases. Therefore, in conventional SWI, the number of phase mask multiplication is usually limited to 4, which otherwise will reduce CNR. Alternatively, loss of structures will occur when denoising is performed using methods which are not specific for SWI.

Apart from these, imperfections in background suppression in regions with low SNR may cause under estimation of local susceptibility distribution and information loss in the magnitude SWI. Therefore, a major challenge in SWI is to recover the lost information in regions with high phase wraps and bulk field inhomogeneities. So a

robust method to restore the SuR information in the background suppressed phase is important.

CHAPTER 2

LITERATURE REVIEW

2.1 Origin of SWI processing

The signal intensity changes in MR images with respect to the blood oxygen level was first observed by Ogawa et al. (Ogawa et al., 1990b). Later several studies were conducted to understand the mechanism behind BOLD phenomena (Ogawa et al., 1993, Yablonskiy and Haacke, 1994, Boxerman et al., 1995, Haacke et al., 1995, Menon et al., 1998). In blood oxygen level depended (BOLD) imaging, the susceptibility difference between deoxygenated and oxygenated hemoglobin in the microvasulature and vasculature affects the signal intensities (Ogawa et al., 1990a). Susceptibility of blood in arteries and veins was quantified by Weiskoff and Kiihne (Weisskoff and Kiihne, 1992). This difference arises from the fact that the unpaired electrons in the deoxygenated hemoglobin cause a paramagnetic behaviour while oxygenated hemoglobin results in diamagnetism. Thus the oxygenation status of venous and arterial blood determines the change in bulk magnetic susceptibility. Pioneering work by Reichenbach et al (Reichenbach et al., 1997) uses the field information in the phase image for clinical investigation of iron deposition. In their article, it is shown that the bulk susceptibility of deoxygenated blood causes a shift in phase value between the spins of venous and brain parenchyma. The difference in phase behaviour of the brain parenchyma and the veins, in the presence of high field strength and long TE, enables the visualization of vascular structures. This initial work was termed as BOLD venography due to the oxygen level dependency for visualization of veins. As a clinical application, it was first used to detect venous

malformation (Lee et al., 1999). The correlations between susceptibility of the brain tissues due to iron depositions and phase shift in the GRE images was studied by (Ogg et al., 1999) and concluded that MR phase reflect the change in tissue susceptibility .

However, there are certain limitations with this approach. One of the major problems is the signal loss that stems from the long TE approach. Signal loss geometries like air-tissue interface limits the application of BOLD venography in different anatomical regions. This necessitated the need for a more robust method to use the details in phase to visualize structures with different susceptibility values. Although phase image contains information related to tissue susceptibility, phase images were unable to be directly useful for clinical purposes due to the presence of background fields induced by main field inhomogeneity and global geometry of the object. Later, Haacke and his group developed a mechanism to retain the local field information after suppressing the background fields. In 2004, (Haacke et al., 2004) demonstrated a fully functional working model to combine the magnitude image and phase information to generate susceptibility weighted images. In this method, the unwanted components of the phase were removed while preserving the local field information by using a homodyne high pass filtering.

2.2 Clinical Utility of SWI

Studies on the application of SWI to image the BOLD changes starts with the assessment of vascular architecture at modulated oxygen level by Rauscher et al. in 2005 (Rauscher et al., 2005a). The field variation around the venous structures was studied by changing the oxygen level in the blood. For this, healthy volunteers were

subjected to oxygen and carbogen breathing while acquiring signals. It is observed that with increase in the blood oxygen level due to oxygen and carbogen breathing, field inhomogeneity around the venous structures reduces along with the reduction in phase shift between the veins and brain parenchyma. As a result, T_2^* effect reduces together with the reduction in contrast between venous structures and neighboring tissue. The contrast reduction is severe while breathing carbogen. This study greatly helps to investigate the venous vasculature using high resolution SWI and its dependence on the blood oxygenation level.

It is reported that the filtered phase image obtained from SWI processing is useful in visualizing a wide range of structures like small veins and deep brain nuclei which are not visible in the magnitude image (Rauscher et al., 2005b). These filtered phase images play a key role in visualization of mineral deposition as discussed in (Thomas et al., 2008). Since calcium is diamagnetic and blood products are paramagnetic, differentiation of calcification and hemorrhage is made possible in the phase images. Analysis of phase shift is also finding useful in quantifying mineral deposits that are indicative of various neuro-degenerative conditions.

Susceptibility based contrast enhancement finds wide range of applications in various clinical applications. A few examples of the clinical applications of SWI was demonstrated by (Thomas et al., 2008) that includes vascular malformations, venous thrombosis, brain tumor, trauma, stroke, neurodegenerative diseases and multiple sclerosis. In the case of venous malformation, conventional MR sequences like Magnetic Resonance Angiography (MRA) and Time –of-Flight (TOF) exhibited poor delineation of low flow venous structures. Moreover, due to partial volume effect

there was considerable loss of information in the small vessels. By using a T_2^* weighted high resolution GRE image, SWI increases the sensitivity toward low flow multi-directional small venous structures and reveals the vascular malformations (Lee et al., 1999, Reichenbach et al., 2001). Using the magnitude and phase image in SWI, (Lin et al., 1999) it is shown that cortical venous thrombosis can be detected better in SWI as compared to the conventional T_2 spin echo images.

For pre-operative grading of gliomas, Bagley et al found that T_2^* weighted GRE images can add more information on the hemorrhagic components based on its susceptibility (Bagley et al., 1997). Later it was reported that SWI depicts better visualization of lesions compared to contrast enhanced T_1 weighted images (Sehgal et al., 2006). An interesting observation related to SWI contrast is that relative to normal tissues, CSF appears dark while edema shows enhanced signal intensity. This unique intensity feature makes SWI suitable for detection of lesions. Moreover, SWI is able to detect the hemoglobin products within the tumors; where as in conventional MR sequences, it is not visualized.

Application of SWI in detecting Diffuse axonal injury (DAI) was studied by Tony et al and Babikian et al (Tong et al., 2004, Babikian et al., 2005). It is found that the SWI is more suitable to detect DAI more than the GRE images due to the presence of hemorrhages. SWI is shown to be useful for evaluation of DAI in deep subcortical white matter which are not visualized in spin echo images or CT. Moreover, Tony et al. has shown that the only means to visualize small hemorrhagic lesions is by using SWI. Sensitivity of SWI towards the hemorrhage make it an important sequence to indentify infract in stroke cases (Wycliffe et al., 2004). Additional signal cancellation

introduced by the phase image causes a hypointense appearance in the regions of subacute and acute hemorrhage. Reports show that thrombo-embolism which is a reason of infracts, also causes susceptibility change by decreasing the flow in arterial blood and increase in the level of deoxyhemo globin (Mammen, 1992). Although diffusion weighted imaging is conventionally used to detect acute stroke, SWI may give more details for identifying the blood products within the infract, identifying the occult arteries by detecting thrombo-embolism and predicting hemorrhagic transformation by identifying microbleeds (Mittal et al., 2009). The Cerebral microbleed which is observed in various pathological conditions like cerebral amyloid angiopathy, hypertension and leuko encephalopathy are visualized better in SWI than the T_2^* weighted images and conventional spin echo images (Thomas et al., 2008).

Radwan et al., performed a clinical study that demonstrated the application of SWI in the evaluation of brain lesions (Radwan et al., 2011). In this study, it was reported that while both CT and conventional MRI showed no abnormalities, SWI revealed positive findings. The unique capability of SWI to reveal hemorrhagic lesions is useful for identification of lesions along the brain stem, basal ganglia and gray-white matter junctions.

Haacke et al. initiated the study of using filtered phase image for measurement of iron deposition in the brain (Haacke et al., 2005, Haacke et al., 2007, Haacke et al., 2010b). The finding of Haacke matched with the earlier findings in literature that relates to iron content in the brain with progression in age (Chua and Morgan, 1996). Age related changes in iron depositions were further studied by (Wang et al., 2012)

using the unique feature of SWI phase that changes with the susceptibility of tissues. Barbosa et al. did a detailed study on the effect of phase mask to differentiate hemosiderin and calcium (Barbosa et al., 2015). In their analysis, it was found that in all cases where CT images identified calcium deposition, SWI also revealed calcium with a hyperintense signal. It is reported that compared to GE- T_2^* image, SWI revealed more micro hemorrhages in the brain (Larsen et al., 2007). Qualitative and quantitative assessment of iron deposition using SWI in amyotrophic lateral sclerosis patients was studied by (Sheelakumari et al., 2016), and observed the pivotal role of iron deposition. Their study concluded that measurement of motor cortex iron deposition could be set as a biomarker for these diseases. Another study on Amyotrophic Lateral sclerosis showed the capability of SWI to identify the alternation in myelin (Prell et al., 2015). For Parkinson's, clinicians and radiologist have confirmed the potential of SWI for characterization of iron deposition to diffentiate Parkinson diseases from a typical Parkinsonion disorder (Wang et al., 2016). A recent investigation using SWI also relates iron deposition in fronto-temporal dementia subtype with associated behavioral profile (Sheelakumari et al., 2017).

2.3 Processing techniques for phase images

The differences in tissue susceptibility arises mainly due paramagnetic substances (e.g. ferritin, hemosiderin etc) or diamagnetic (e.g. calcium) substances (Schenck, 1996, Schenck and Zimmerman, 2004, Shmueli et al., 2009, Langkammer et al., 2012). Due to local susceptibility variation the magnetic field changes spatially, results in spatial variation of signal phase. Therefore the phase image provides

information about magnetic field perturbations in the object imaged. The field variation caused by the susceptibility of local tissues are called microscopic field changes, whereas the macroscopic field changes are due to bulk susceptibility differences at regions such as air-tissue interface. The macroscopic field variations typically have low spatial frequency components (Wang et al., 2000). Since the phase arises from the microscopic field changes have high spatial frequency, the macroscopic field effects are removed by high-pass filtering (Wang et al., 2000, Sehgal et al., 2005).

However, since this filtering is in Fourier domain, information from spatially large tissue structures may get filtered out depending on the strength of the applied filter. Hence, the filter parameter which determines the filter strength plays an important role in SWI processing. When the filter strength is too low, macroscopic background phase effect may not be fully removed, while high filter strength will remove the useful local phase information from tissues of interest. High pass filtering approach assumes that the background field effects are slowly varying across the image, and are thus constrained to lower spatial frequencies, while the intrinsic field effects are local and thus confined to the higher spatial frequencies. In practice, this assumption does not always hold, especially in large iron containing structures such as the basal ganglia regions (Haacke et al., 2010a). Homodyne high pass filtering is a trade-off between tissue contrast and removal of macroscopic field inhomogeneities. If the filter strength is increased, the contrast between tissues is removed and only the edges of the tissue structures are retained. The strength of the filter required for

removing background phase variations also depends on the TE of the imaging experiment.

In general, the distribution of voxel weights derived from phase information is manipulated by an exponent applied to the phase mask. In a recent approach, the exponentiation is implicitly eliminated using a model of Human Contrast Sensitivity Function (HCSF) applied to selectively amplify the phase information at a series of high frequency points, constituting the center frequencies of a set of band-pass filters (Wang et al., 2014). The weight applied to each band-pass filtered phase is obtained as the spectral magnitude of HCSF at the corresponding center frequency. In their study, the parameters of HCSF are chosen by inspection of image quality, so as to fit a large cohort of SWI data. Similar to other existing approaches using homodyne filtering, the HCSF SWI processing is able to suppress background components generated by the instrumentation. However, since the field inhomogeneities increase with the strength of main magnetic field and TE, all of the above mentioned SWI processing methods fail to completely eliminate such effects without prior tuning of filtering parameters, or adjustments using visual inspection.

In GRE MR imaging, phase of the signal acquired is linearly proportional to the local field shift

$$\theta = \gamma \Delta B TE, \tag{2.1}$$

where θ is the phase of the MR signal, ΔB is a local field shift due to tissue magnetic susceptibility effects as well as background field effects. The measured phase (Θ) wraps around every 2π according to

$$\boldsymbol{\psi} = mod(\theta, 2\pi) \tag{2.2}$$

In conventional SWI processing, under the assumption that phase from local tissue is of high spatial frequency, homodyne filtering can be expressed as

$$\theta_{\text{filt}} = angle\left(\frac{I}{FFT^{-1}(h.FFT(I))}\right), \tag{2.3}$$

where θ_{filt} is the filtered phase, I is the measured image, and h the low-pass filter function. Since the homodyne filter works on complex data, phase unwrapping is not necessary for homodyne filtered phase images. However, to perform spatial operations on the phase image, the measured phase needs to be unwrapped.

Using the MR image (I), a weighting scheme is developed to enhance the venous contrast. The enhancement is achieved using a data driven phase mask, derived from unwrapped phase image, instead of the conventional linear mask mapped from the filtered image. Unwrapped phase can be obtained by applying Laplacian operators in the Fourier space of the phase maps (Bagher-Ebadian et al., 2008). The forward and inverse Laplacian operators applied to any spatial function $f(x,y)$ can be calculated using (Schofield and Zhu, 2003, Volkov and Zhu, 2003)

$$\nabla^2 f(x,y) = -\frac{4\pi^2}{N^2} FFT^{-1}\{(p^2+q^2)FFT[f(x,y)]\} \tag{2.4}$$

$$\nabla^{-2} f(x,y) = -\frac{N^2}{4\pi^2} FFT^{-1}\left\{\frac{FFT[f(x,y)]}{(p^2+q^2)}\right\}, \tag{2.5}$$

where (*x*,*y*) and (*p*,*q*) are the spatial and spectral coordinates respectively. For an input image of size *N*×*N*, the spectral coordinates take values $p, q = -\frac{N}{2}, \cdots, 0, \cdots \frac{N}{2} - 1$. The unwrapped phase($\widehat{\boldsymbol{\psi}}$) is then computed using

$$\widehat{\boldsymbol{\psi}} = \nabla^{-2}\left(cos\boldsymbol{\psi}\nabla^2(sin\boldsymbol{\psi}) - sin\boldsymbol{\psi}\nabla^2(cos\boldsymbol{\psi})\right) \quad (2.6)$$

In further discussion, wrapped and unwrapped phase components will be designated using $\boldsymbol{\psi}$ and $\widehat{\boldsymbol{\psi}}$ symbols. Conventionally, this unwrapped phase is then used as input to methods involving spatial processing of phase such as polynomial fitting methods (Abduljalil et al., 2003).

2.4 Modifications in SWI data acquisition

Conventional SWI uses a flow-compensated 3D GRE sequence with a relatively long echo time (TE = ~ 25 ms at 3 T). Due to the long echo times, artifacts may occur in brain regions with inhomogeneity. Identification of local susceptibility sources such as vessels becomes challenging, and therefore, limits the applicability of SWI in areas with high field inhomogeneities. Such artifacts are more prominent in phase than in magnitude.

Approaches intended to compensate for these artifacts removes artifacts only in phase images (Rauscher et al., 2003, Jin et al., 2008, Neelavalli et al., 2009).Consequently, the processed SWI images will have remnant artifacts due to signal dropout in magnitude data. The magnitude signal dropout is remedied by fitting a signal decay model (Fernandez-Seara and Wehrli, 2000, Truong et al., 2006, Baudrexel et al., 2009) or by using *z*-shim that compensates the field gradients

(Frahm et al., 1988, Yang et al., 1998, Glover, 1999, Meng and Lei, 2008, Nam et al., 2012).

A multi-echo approach for SWI shows a variety of advantages in comparison to the single echo acquisition. SNR is improved in standard SWI using a low readout bandwidth. This requirement is necessitated by the small voxel sizes and long echo times. Nevertheless high bandwidth is necessary for the minimizing the geometric distortions, chemical shifts and blur along readout direction, with a relatively short echo spacing of 7ms (Denk and Rauscher, 2010). In this situation, the resulting SNR that is penalized per echo is compensated due to acquisition of more number of echoes. In this modified sequence, flow compensation is performed fully in the first echo. While the flow compensation is not performed in second and the fourth echoes, third and fifth echoes flow compensation is done along the readout direction only (Deistung et al., 2009). A caveat here is the appearance of false veins in the higher echoes due to signal losses experienced by arterial vessels with fast blood flow. In parallel MRI, SWI reconstruction is performed using the SENSE algorithm (Pruessmann et al., 1999), resulting in unfiltered and wrapped phase images. The phase images are then unwrapped and homodyne filtered. To reduce the number of phase wraps at higher echoes, it is necessary to adjust the strength of the homodyne filter for each echo. The study conducted by (Deistung et al., 2005) investigates the role of filter strength on echo time. In accordance with what is reported in their study, it is possible to effectively suppress the phase wraps together with achieving a reasonable good phase contrast if the filtering is performed using a 2D Fourier domain window with a size of 20 to25% of the k-space dimension at the lower

echoes. At later echoes, the window size needs to be adjusted to account for the linear scaling of the phase with field inhomogeneities. The increase in SNR reported in (Deistung et al., 2005)is also in agreement with a study using dual echo SWI conducted by (Brainovich et al., 2009). The effect of multi-echo averaging on SNR is reported in the study by (Helms and Dechent, 2009).

2.5 Post processing methods in multi-echo SWI

In the dual echo scheme proposed by (Brainovich et al., 2009), the mean phase and mean magnitude volumes are first generated, and then used to produce a single SWI. In an alternative scheme by (Denk and Rauscher, 2010), a multi-echo acquisition with five echoes is used to produce five different SWI and latter combined to form the final SWI image. Both schemes were shown to result in improved CNR than the standard SWI. While a conventional phase mask function suffices for multi-echo data, the use of alternative mask functions are shown to result in higher CNR of the cerebral veins (Casciaro et al., 2010).

In the post-average multi-echo SWI processing, standard SWI processing is first performed and later averaged to obtain the processed images. To avoid phase wrapps and background field contributions from each echo Denk and Rauscher used a homodyne filter whose strength linearly increases with TE. Quinn et al. proposed the use of a constant filter size to compromise between elimination of wraps and preservation of contrast in the images obtained from all echoes (Quinn et al., 2014).

The third approach for multi-echo SWI processing is a frequency-based method in which successive TE-dependent phase images are temporally unwrapped at each

voxel and divided by TE to generate the frequency maps. A weighted average of the frequency is then computed followed by the generation of the mask. Distinct from the method developed by (Brainovich et al., 2009) that considers mean of the phase images for generating the phase mask, the frequency weighted method involves temporal unwrapping of phase together with masking the weighted average of the frequency maps. Intuitively, the mean of the frequency maps is more physically interpretable quantity than the mean of the phase images as used by (Brainovich et al., 2009).

2.6 SNR enhancement in SWI

For identification of small venous structures, it is required to increase the image resolution. However, higher resolution is accompanied by reduction in the SNR. In this context, several post-processing methods have been developed to either increase the resolution without compromising the SNR or restore the reduced SNR in high-resolution SWI. Although standard procedures using spatial filters such as a Gaussian low-pass filter (Wink and Roerdink, 2004), a median filter (MF) (Ying et al., 1996), or an anisotropic diffusion filter (Samsonov and Johnson, 2004) are very effective for noise suppression, they tend to remove information about edges between tissues, or introduce artificial features such as stair casing artifacts (Ying et al., 1996, Samsonov and Johnson, 2004, Wink and Roerdink, 2004). This led to a cohort of SWI post-processing technique to increase spatial resolution without reduction of SNR and introduction of artifacts.

A second major concern for SNR enhancement is the value of an appropriate echo time that generates a high-contrast magnitude SWI. Experimental observations have

revealed maximal contrast at TE=28 ms for veins parallel to the B_0field and later echoes for veins oriented at other angles (Reichenbach et al., 2000, Haacke et al., 2004, Hernando et al., 2012). This brings out the difficulties in performing SWI venography at a fixed echo time. Furthermore, there are no clear cut guidelines for the choice of optimal echo times to image venous structures that are not oriented along the main field. This further motivates the development of denoising techniques that do not introduce spatial artifacts in the processed magnitude SWI.

In this context, a potential SNR improvement in multi-echo SWI venography was achieved by application of a predictable signal model fitted to the multi-echo magnitude data (Jang and Hwang, 2011, Jang and Hwang, 2012).Based on the idea that the T2* relaxation curves of brain tissues follow a multi-exponential decay pattern (Wachowicz and Snyder, 2002, Lancaster et al., 2003, Andrews et al., 2005, Valentine et al., 2007, Hwang and Du, 2009, Jang and Hwang, 2012), the voxel-wise decay signals extracted from multi-echo images acquired using the MGRE sequence were fitted to a multi-exponential model. This was later followed up with the development of a method that combined the signal model for the magnitude data and the linear phase model for noise suppression(Jang et al., 2013).

A major handicap of the multi-exponential model was that SNR in regions with severe field inhomogeneity and susceptibility differences, such as veins, could not be enhanced. This is primarily due to the non-exponential rapid decay signals in these regions. An alternative proposed by Fan and Gijbels employed a piecewise polynomial model(FanJQ, 1996). The temporal fitting process enabled noise suppression in the magnitude data. For noise suppression in the phase data, the phase

data is first temporally unwrapped, followed by fitting a polynomial model. A limitation of this approach at long TE is the need for exclusion of phase data from the fitting process, at low SNR locations. With the field perturbation assumed to be temporally invariant, and the phase evolving at a fixed rate ϕ with reference to a phase offset ϕ_0, the linear phase model

$$\Phi(TE) = \phi TE + \phi_0 \tag{2.7}$$

is typically used to suppress the noise in the multi-echo phase data. The unknown parameters ϕ and ϕ_0 are determined by least squares error method (Abdi et al., 2003).

2.7 Data Reconstruction

Since noise or artifact in the phase images can propagate into the final output in the SWI processing pipeline, reconstruction of the phase images from a GRE sequence becomes very crucial (Schweser et al., 2013, Liu et al., 2013a, Haacke and Reichenbach, 2014). A major problem encountered with improper coil combination for generation of phase image is the appearance of cusp artifacts which could also be misinterpreted as microbleeds (Haacke et al., 2015, Li et al., 2015).

Coil combination becomes an integral step if the GRAPPA (Griswold et al., 2002) is used for image reconstruction. In this case, the magnitude and phase images for each channel of the phased array coil need to be procrssed separately, which are then combined to generate the final images (Griswold et al., 2002, Hammond et al., 2008, Robinson et al., 2011). To preserve phase information during coil combination, it is required to have a prior knowledge of the coil sensitivities (Roemer et al., 1990,

Pruessmann et al., 1999, Walsh et al., 2000, Bydder et al., 2002). For sufficiently high SNRs, the coil combination is performed by sum-of-squares operation, if the coil sensitivity is approximated as the complex conjugate data (Roemer et al., 1990). Due to the influence of the coil sensitivity-induced phase components between different coils, coil combination using a magnitude information only will result in cusp artifacts (Hammond et al., 2008, Ros et al., 2009, Robinson et al., 2011, Parker et al., 2014, Ma et al., 2015). Using Eq. (2.7), the j'th channel phase in a left-handed system can be expressed as

$$\Phi_j(r, TE) = \gamma \Delta B(r) TE + \phi_{0,j}(r), \tag{2.8}$$

where $\phi_{0,j}(r)$ is the phase component due to coil sensitivity. In most applications, the offset $\phi_{0,j}$ is assumed to be a constant. Although the constant phase offset eliminates cusp artifacts in the central part of the FOV, the combined phase image quality will depend on the region selected for estimating the baseline. $\phi_{0,j}(r)$ can be more accurately estimated using either a body coil or multi-echo data (Ros et al., 2009, Robinson et al., 2011). For a double echo acquisition,

$$\phi_{0,j}(r) = \frac{TE2.\phi_{TE1,j}(r) - TE1.\phi_{TE2,j}(r)}{TE2 - TE1} \tag{2.9}$$

A more accurate method for estimation of the phase offset involves modelling the coil sensitivity induced phase component as a 3D linear function in k-space (Haacke et al., 1999, Liu et al., 2015). With this approximation, the phase offset can be expressed as

$$\phi_{0,j}(r) = \boldsymbol{\beta}_j r + \phi_{c,j}\,, \tag{2.10}$$

where $\phi_{c,j} = arg(K_{max,j})$ and $K_{max,j}$ denotes the maximum k-space magnitude. Using the Fourier shift theorem, $\boldsymbol{\beta}_j = [\beta_{x,j}, \beta_{y,j,}, \beta_{z,j}]$ is estimated as the gradient at the peak location with magnitude $K_{max,j}$. The use of only the low resolution part of k-space results in saving time and memory. The combined phase is obtained from the complex data by averaging the individual channel phases after subtraction of their respective offsets, weighted by the squared channel magnitudes.

CHAPTER 3

MATERIALS AND METHODS

3.1 Granularity controlled edge-preserved denoising of multi-channel GRE images

SWI derives information about susceptibility differences between tissues from high resolution phase images in GRE acquisitions. As GRE provides significant contrast boost between and within gray and white matter, the required susceptibility contrast is invariably obtained by weighting the magnitude GRE image with a phase mask derived from the high-pass filtered GRE phase image. Processing to obtain the phase mask, however, goes through several intermediate steps wherein the raw phase is either subjected to a high-pass homodyne filter, or spatially varying high-pass filters following an initial phase unwrapping step. The main aim of these processing is to improve the susceptibility related contrast in the magnitude SWI image with reduced effect of artifacts. However the acquisition noise in the GRE phase image causes granular appearance in the processed phase image. Consequently in parallel MRI (pMRI) based GRE acquisition, inadequate processing of the channel phase images prior to obtaining the combined phase can result in mis-representation of structures and significantly influence the resolution and accuracy of the resulting susceptibility map.

This can be addressed by channel-wise phase processing, with granularity controlled edge-preserved denoising, or by introduction of regularization in the high-pass filtering process. The former is applied either to the combined phase, or to real and

imaginary parts of the complex image. One such denoising method by Jang et al.,(Jang et al., 2013) uses a linear fitting phase model to suppress the phase noise of echoes in multi-echo acquisition. Alternately, Borrelli et al., (Borrelli et al., 2015) applied a multi-component Non-Local Means (NLM) filter on the real and imaginary part of complex data obtained after high-pass filtering stage of the SWI pipeline.

Most of the edge preserved denoising methods involve minimizing a cost function consisting of two main components. The data fidelity term which controls the deviation of the denoised data from the original data and second one is the regularization term which introduces a smoothness controlled by the regularization term λ. The regularization term uses a predefined potential function which works on the cliques of the neighbourhood system. The robustness of the potential function is controlled by a scale parameter ts. It often happens in a noisy image that if λ is too small, even the small intensity change is treated as edge and the image appears granular, on the other hand, if λ is increased, some desired edges are lost. These granular effects in filtered phase will decrease the quality of SWI, since the mask generated from the filtered phase is multiplied several times with the absolute image in SWI processing. To reduce the effect of granularity an extra term is included in the cost function that assigns additional weighting to large change in intensities that are given a constant cost by the potential (Rudin et al., 1992, Charbonnier et al., 1997, Rivera and Marroquin, 2003).In the proposed method, maximum extent of edge-preserved denoising and granularity control is achieved without the extra term and additional parameter. Furthermore, the inbuilt automatic tuning features of ts makes our algorithm a convenient and attractive tool for SWI processing pipeline.

Since gradient descent methods can only optimize one variable at a time, the desired phase image is to be estimated separately for each value of ts, which becomes time consuming especially if the processing is performed for each channel separately. In our approach to control the granularity with edge preservation, the phase images are iteratively updated using an intermediate filtering operation dependent on ts, as deduced from the derivative of the main cost function. The edge preservation and granularity control are achieved by fixing the value of ts used for the intermediate filtering step. In each iteration there would be one ts value corresponds to which the cost function is minimum (ts_{01}). This automatically sets the limit to the extent of edge-preserved denoising with granularity control.

3.1.1 Channel phase pre-processing for GRADER

In the measured phase images of each channel, phase wrapping artifacts are present due to the phase shifts larger than 2π. Since the measured phase have a direct relation to the local field variations and TE used for acquisition, the contrast of venous structures and hemorrhages increases along with the effect of phase wraps at higher TE. Therefore phase pre-processing is usually performed to extract the SuR field information, (Rauscher et al., 2005b, Li et al., 2014a). For this thesis work, the Laplacian based fast unwrapping method (Schofield and Zhu, 2003, Li et al., 2014b) was used.

Quality of SWI depends on the estimated local field after phase pre-processing to remove phase wrapps and background field. The global geometry of the object and other components such as the phase contribution due to channel sensitivity causes background field which needs to be removed to observe the susceptibility change in

the tissues. High-pass filtering of the measured data is one common way to remove the background field (Haacke et al., 2009). However, proper selection of high-pass filter strength to reduce the loss of local field information is a difficult task. (Schweser et al., 2010, Liu, 2014). To avoid signal loss, phase unwrapping and background suppression methods are used. Here PDF based background is used after phase unwrapping (Liu et al., 2011a). These background suppressed phase are denoised prior to SWI processing.

The measured channel phase image (ψ_j) contains components due to background filed and intrinsic susceptibility variations which are corrupted by measurement noise. To observe the local field variations due to intrinsic susceptibility sources, the phase images are subjected to phase unwrapping and background suppression. The unwrapped channel phase ($\hat{\psi}_j$) is subjected to background field removal and the resultant phase image (φ) contains components only due to local susceptibility sources and measurement noise (η_j). The phase change due susceptibility sources such as venous structures and micro bleeds constitute edges (borders) in the noisy phase image.

3.1.2 Application of potential function for high-pass filtering

Using the background field removal methods like PDF, the large amplitude field components of the unwrapped phase is removed. The background suppressed phase φ contains components due local field variations and noise. With the application of a filter the remnant phase components can be high-pass filtered and mapped to generate the phase mask for SWI processing. However conventional high-pass filter amplifies the remnant noise and destroys the structural similarity. Therefore a high-

pass filtering operation which can suppress the noise and enhance the relevant structural information is needed. To address this, a high-pass filter which operates on the weighted neighbourhood phase difference is used. The weights for the neighbourhood operation is estimated using a positive valued potential function $\boldsymbol{\phi}$**.** The above mentioned high-pass filtered phase ($\widehat{\boldsymbol{\omega}}_{HPF}$) at location r is given by

$$\widehat{\boldsymbol{\omega}}_{HPF}(r) = \frac{1}{n_i}\sum_i \left[\boldsymbol{\phi}\left(\frac{\nabla\widehat{\boldsymbol{\omega}}_{r,i}}{ts}\right)\right], \tag{3.1}$$

where n_i is the number of cliques and $\nabla\widehat{\boldsymbol{\omega}}_{r,i}$ is the phase difference computed between the r'th location and its clique along direction i. $\boldsymbol{\phi}(\cdot)$ is the positive valued symmetric function with a known derivative. Sample potential functions with their derivatives are shown in Table 3.1 (Charbonnier et al., 1997).

Table3.1: Edge preserving potential functions and their associated weighting function

$\phi(x)$	$\phi'(x)$
$\phi_{GM} = \frac{x^2}{1+x^2}$	$\frac{2x}{(1+x^2)^2}$
$\phi_{HL} = \log(1+x^2)$	$\frac{2x}{1+x^2}$
$\phi_{HS} = 2\sqrt{1+x^2} - 2$	$\frac{2x}{\sqrt{1+x^2}}$
$\phi_{HS} = 2\log(\cosh x)$	$\begin{cases} 0 & x = 0 \\ 2\tanh(x) & x \neq 0 \end{cases}$

3.1.3 Granularity controlled denoising using alternating minimization

A conventional high-pass filter applied to the background suppressed GRE phase destroys the structural similarity and amplifies noise. Therefore before the

application of high-pass filter, a denoising operation is necessary. However, to obtain a denoised phase $\widehat{\boldsymbol{\omega}}$ using regularization and to tune the filter characteristics that can minimize granularities require prior information. One possible way to control the granularity is by minimizing the cost that use filter function that operates on local gradients (Teboul et al., 1998, Vogel and Oman, 1996),

$$\mathcal{J} = \frac{1}{2}\|\varphi - \widehat{\omega}\|_2^2 + \lambda \sum_i \left\| \phi\left(\frac{\mathrm{R_i}\widehat{\boldsymbol{\omega}}}{ts}\right)\right\|_1, \tag{3.2}$$

with respect to ts and $\widehat{\boldsymbol{\omega}} \in \Re^N$. Since $\phi(\cdot)$ is symmetric and does not have any negative values, instead of l_1-norm all elements from r=1,2,⋯,N are added together. Consider the dimension of the input image be P rows and Q columns and $N = PQ$, the local gradient operation is performed by using a vectorized $\widehat{\boldsymbol{\omega}}$ and multiply it with a finite differencing matrix R_i of size $N \times N$. The R_i matrix for finite difference operation for each direction is shown in Fig 3.1 The value of the above mentioned cost $\mathcal{J}$ is then determined by ts and $\widehat{\boldsymbol{\omega}}$. If the cost function is minimized with respect to $\widehat{\boldsymbol{\omega}}$ by fixing ts there would not be any control over granularity, but this will only help to preserve the structural information. Even though $\widehat{\boldsymbol{\omega}}$ and ts appears to be independent, selection of ts controls both granularity and structures in the desired image.

One way to minimize the cost with respect to the two variables $\widehat{\boldsymbol{\omega}}$ and ts is through alternating minimization (AM) where first fix the one and minimize $\mathcal{J}$ with respect to the other variable and then fix the second and optimize the first. Derivative of $\mathcal{J}$ in Eq. (3.2) with respect to $\widehat{\boldsymbol{\omega}}$ after fixing ts is

$$\begin{aligned}\frac{\partial \mathcal{J}}{\partial \hat{\boldsymbol{\omega}}} &= (\hat{\boldsymbol{\omega}}-\boldsymbol{\varphi})+\frac{\lambda}{ts}\sum_i\left[\mathrm{R_i^T}\,\mathrm{diag}\left(\phi'\left(\frac{\mathrm{R_i}\hat{\boldsymbol{\omega}}}{ts}\right)\right)\mathbf{1}_N\right] \\ &= (\hat{\boldsymbol{\omega}}-\boldsymbol{\varphi})+\frac{\lambda}{ts}\sum_i \mathrm{R_i^T}\,\phi'\left(\frac{\mathrm{R_i}\hat{\boldsymbol{\omega}}}{ts}\right),\end{aligned} \tag{3.3}$$

where $\mathbf{1}_N$ is $N \times 1$ vector of ones. $diag\left(\phi'\left(\frac{\mathrm{R_i}\hat{\boldsymbol{\omega}}}{ts}\right)\right)$ depict the Jacobian diagonal matrix whose diagonal elements are estimated from $\phi'\left(\frac{\mathrm{R_i}\hat{\boldsymbol{\omega}}}{ts}\right)$.

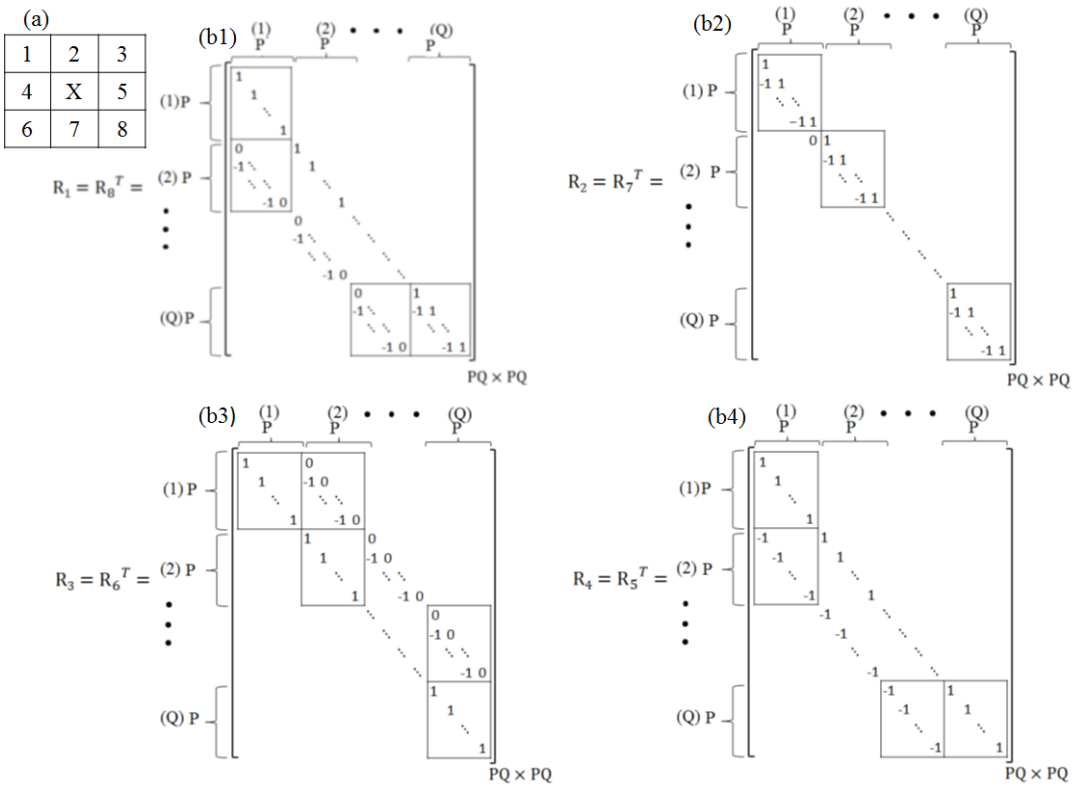

Fig. 3.1: Difference operator implementation. (a) 3×3 neighboring system with X labelled as centre (b1)-(b4) difference operator along ith direction (R_i). The input image size is considered to be P × Q.

Here after, $\mathcal{L}(\hat{\boldsymbol{\omega}}, ts)$ is used to represent the second term of Eq. (3.3). On equating the Eq. (3.3) to zero

$$\hat{\omega} = \varphi - \frac{\lambda}{ts}\,\mathcal{L}(\hat{\omega}, ts)\,. \tag{3.4}$$

As the derivative of the ϕ and $\mathcal{J}$ are known Eq. (3.4) can be written as

$$f'(ts, \hat{\omega}) = \varphi - \left(\hat{\omega} + \frac{\lambda}{ts}\mathcal{L}(\hat{\omega}, ts)\right). \quad (3.5)$$

Quasi-Newton type iterations can be used to solve Eq. (3.4) for $\hat{\omega}$. To start the quasi-Newton iterations using BFGS, an initial estimate of $\hat{\omega}$ is needed which is obtained using

$$\hat{\omega} = \varphi - \frac{\lambda}{ts}\,\mathcal{L}(\varphi, ts)\,. \quad (3.6)$$

At first, for a pre-determined range of ts value, Eq. (3.6) is computed and for each pair of $(ts, \hat{\omega})$ the cost $\mathcal{J}$ is estimated. The initial value is the one that satisfies the condition

$$\left(ts_{01}^{(0)}, \hat{\omega}_{01}^{(0)}\right) \leftarrow \min_{(ts,\hat{\omega})} \mathcal{J} \quad (3.7)$$

The AM algorithm uses this as the input. The SWI processing pipeline which uses the GRADER algorithm is shown in Fig. 3.2.

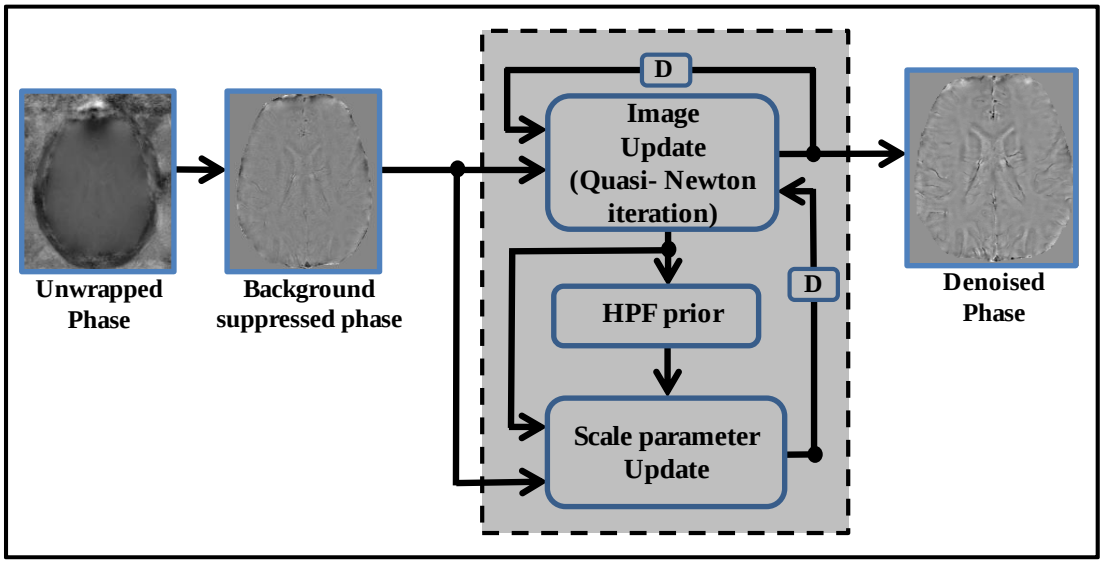

Fig.3.2: Process flow for the GRADER algorithm

GRADER algorithm

Setk $= 1$.

Step 1: Compute $\mathcal{L}\left(\hat{\boldsymbol{\omega}}_{01}^{(k-1)}, ts_{01}^{(k-1)}\right)$

step 2: $\widehat{\omega}_{01}^{(k)} \leftarrow Solve\ Eq.(4)\ with\ starting\ point\ \widehat{\boldsymbol{\omega}}_{01}^{(k-1)}\ and\ ts_{01}^{(k-1)}$
step 3: $ts_{01}^{(k)} \leftarrow \min_{t} \mathcal{J}\left(\varphi, \widehat{\omega}_{01}^{(k)}, ts\right)$
$Repeat\ steps\ 1\ to\ 3\ until\ ts_{01}^{(k)} - ts_{01}^{(k-1)} < tol$

3.1. 4 Extension to parallel MRI (pMRI)

In pMRI, for each channel the initial conditions have to fix as in the GRADER algorithm. Using Eq. (3.4), the channel phase image is estimated followed by optimizing the scale parameter $ts_{01j}^{(k)}$. This is done by using the combined phase image ($\theta^{(k)}$) and φ_j. On fixing the $ts_{01j}^{(k)}$, $\widehat{\omega}_{01j}^{(k)}$ for each channel is estimated through BFGS iterations.

pMRI-GRADER algorithm

Set $k = 1$ and $\theta^{(0)} = \frac{1}{n_c}\sum_j \widehat{\omega}_{01\,j}^{(0)}$
$for\ j = 1, \cdots, n_c$
Step 1: Compute $\mathcal{L}\left(\theta^{(k-1)}, ts_{01\,j}^{(k-1)}\right)$
Step 2: $\widehat{\omega}_{01\,j}^{(k)} \leftarrow Solve\ Eq.(3.4)\ with\ starting\ point\ \theta^{(k-1)}\ and\ ts_{01\,j}^{(k-1)}$
end
Step 3: $\theta^{(k)} = \frac{1}{n_c}\sum_j \widehat{\omega}_{01\,j}^{(k)}$
$for\ j = 1, \cdots, n_c$
Step 4: $ts_{01\,j}^{(k)} \leftarrow \min_{t} \mathcal{J}\left(\varphi_j, \theta^{(k)}, ts\right)$
end
$Repeat\ steps\ 1\ to\ 4\ until\ ts_{01\,j}^{(k)} - ts_{01\,j}^{(k-1)} < tol$

3.1.5 Enhancing the magnitude SWI

The contrast of the magnitude SWI is dependent on the SNR of magnitude as well as the phase. Therefore any process that indent to improve the magnitude SWI should apply on the complex data. Since the above mentioned algorithm and process are

valid only for real numbers, the real part and imaginary part has to be processed individually to enhancement of structural information. This is implemented by individually processing the real part and imaginary using the pMRI- GRADER. This is now mentioned as Imaginary-Real GRADER (IR-GRADER). With the assumption that the measured noise is complex Gaussian, the noise variance in the real and imaginary components is considered to be same. Consequently, it is also possible to treat both the real and imaginary part as the elements of the same vector. On holding this assumption, φ and $\hat{\omega}$ in Eq. (3.2) can be replaced with $\begin{bmatrix} Real(\boldsymbol{I}_j) \\ ----- \\ Im(\boldsymbol{I}_j) \end{bmatrix}$ and $\begin{bmatrix} Real(\boldsymbol{Z}_j^{(k-1)}) \\ ----- \\ Im(\boldsymbol{Z}_j^{(k-1)}) \end{bmatrix}$, where $\boldsymbol{I}_j$ and $\boldsymbol{Z}_j$ represents the complex input and denoised channel data. For quasi-Newton iterations an initial estimate $\check{\boldsymbol{I}}_j$ of the desired solution need to be calculated and is first obtained using

$$\begin{bmatrix} Real(\check{\boldsymbol{I}}_j) \\ ----- \\ Im(\check{\boldsymbol{I}}_j) \end{bmatrix} = \begin{bmatrix} Real(\boldsymbol{I}_j) \\ ----- \\ Im(\boldsymbol{I}_j) \end{bmatrix} - \frac{\lambda}{ts}\, \mathcal{L}\left(\begin{bmatrix} Real(\boldsymbol{I}_j) \\ ----- \\ Im(\boldsymbol{I}_j) \end{bmatrix}, ts \right), \tag{3.8}$$

Similar to GRADER for a range ts values, Eq. (3.8) is computed and the cost is estimated for each pair $\left(ts, \begin{bmatrix} Real(\check{\boldsymbol{I}}_j) \\ ----- \\ Im(\check{\boldsymbol{I}}_j) \end{bmatrix} \right)$. The initial $ts_{01j}^{(0)}$ and $\check{\boldsymbol{I}}_j^{(0)}$ is fixed to the pair that satisfies

$$\left(ts_{01j}^{(0)}, \begin{bmatrix} Real(\check{\boldsymbol{I}}_j^{(0)}) \\ ----- \\ Im(\check{\boldsymbol{I}}_j^{(0)}) \end{bmatrix} \right) \leftarrow \min_{\left(ts, \begin{bmatrix} Real(\check{\boldsymbol{I}}_j) \\ ----- \\ Im(\check{\boldsymbol{I}}_j) \end{bmatrix} \right)} \mathcal{J}, \tag{3.9}$$

which is later given to AM algorithm.

$\boldsymbol{\varphi}_j = \angle \boldsymbol{I}_j, \boldsymbol{\theta}^{(0)} = \frac{1}{n_c}\sum_j \angle \check{\boldsymbol{I}}_j^{(0)}$, $\mathbf{Z}_j^{(0)} = \left|\check{\boldsymbol{I}}_j^{(0)}\right| \exp(i\boldsymbol{\theta}^{(0)})$,$k = 1$.

$for\ j = 1, \cdots, n_c$

Step 1: Compute $\mathcal{L}\left(\begin{bmatrix} Real(\boldsymbol{Z}_j^{(k-1)}) \\ ----- \\ Im(\boldsymbol{Z}_j^{(k-1)}) \end{bmatrix}, ts_{01\,j}^{(k-1)}\right)$

Step2:

$\begin{bmatrix} Real(\check{\boldsymbol{I}}_j^{(k)}) \\ ----- \\ Im(\check{\boldsymbol{I}}_j^{(k)}) \end{bmatrix} \leftarrow Solve\ Eq.\ (3.4)\ with\ starting\ point \begin{bmatrix} Real(\boldsymbol{Z}_j^{(k-1)}) \\ ----- \\ Im(\boldsymbol{Z}_j^{(k-1)}) \end{bmatrix}\ and\ ts_{01\,j}^{(k-1)}.$

end

Step 3: $\boldsymbol{\theta}^{(k)} = \frac{1}{n_c}\sum_j \angle \check{\boldsymbol{I}}_j^{(k)}$.

$for\ j = 1, \cdots, n_c$

Step 4: $\boldsymbol{Z}_j^{(k)} = \left|\check{\boldsymbol{I}}_j^{(k)}\right| exp\left(i\boldsymbol{\theta}^{(k)}\right)$.

Step 5: $ts_{01\,j}^{(k)} \leftarrow \min_t \mathcal{J}\left(\begin{bmatrix} Real(\boldsymbol{I}_j) \\ ----- \\ Im(\boldsymbol{I}_j) \end{bmatrix}, \begin{bmatrix} Real(\boldsymbol{Z}_j^{(k)}) \\ ----- \\ Im(\boldsymbol{Z}_j^{(k)}) \end{bmatrix}, ts\right)$

end

$Repeat\ steps\ 1\ to\ 5\ until\ ts_{01\,j}^{(k)} - ts_{01\,j}^{(k-1)} < tol.$

3.2 Noise compensation in SWI processing with spatial high-pass filter

SWI in clinical settings is used for investigation of neurodegenerative conditions and mild cognitive impairments. One of the challenges in SWI is the separation of low amplitude susceptibility related local field from the large amplitude background field induced by global geometry of the object and other components such as the phase contribution from coil sensitivity. This is because the large amplitude low spatial frequency components is conventionally removed through high-pass filtering. (Haacke et al., 2009, Liu et al., 2017). A very strong high-pass filter required to avoid the rapid phase variations at certain regions will also result in loss of information related to tissue susceptibility (Liu, 2014). Information loss is dependent on size of

the filter and the object. To avoid this, phase unwrapping and background suppression using Projection onto Dipole Fileds (PDF), or Sophisticated Harmonic Artefact Reduction for Phase data (SHARP) can be used. An additional high-pass filtering is usually performed on the pre-processed phase images to further reduce the low spatial frequency phase artifacts (Liu, 2014). The SuR contrast in the magnitude is improved by weighted with a phase mask (Haacke et al., 2009, Barbosa et al., 2015). This in turn is constructed by mapping the HP filtered phase to values in the range [0,1] using a mapping function (Quinn et al., 2014). While voxels mapped to lower values highlight regions with susceptibility changes, those falling around unity appear as a bright region in the phase mask.

Other than background suppression, a second most challenging step that influences the diagnostic quality of SWI involves choice of filter parameter This is because filtering in the presence of noise can introduce spurious information in the form of edges that can very well be interpreted as susceptibility related. To select the desirable filter characteristics and mapping function, we consider classifying the intensities of the phase mask into two regions, viz. the one with intensities lower than the phase mask mean representative of voxels containing susceptibility related information (C_1), and the other representing the bright region (C_2).

Other than our current approach of tuning the filter and phase mask, attempts have been made earlier to synthetically boost the high-frequency characteristics of SWI phase without consideration of the phase mask, or its statistical parameters (Borrelli et al., 2015, Wang et al., 2014). While the first address the problem of noise related artifacts by denoising the real and imaginary components using a multi-component

NLM filter (Borrelli et al., 2015), the second attempts to enhance the high-frequency characteristics using frequency weights derived from the human contrast sensitivity to the spatial frequencies (HCSF) of the phase image. The weights for discrete frequency bands of the phase image are synthesized using a modified form of HCSF that dictates emphasis of higher spatial frequencies for improving the contrast. Besides the fact that in practice, choice of HCSF parameters are made subjectively, the synthetically derived weights do not address the problem of noisy appearance in phase mask.

The high-frequency components of measured phase are estimated as the result of a homodyne filtered image. The filtering operation is performed by division of the measured image with a low-pass image (Haacke et al., 2004, Rauscher et al., 2008). The low-pass image is generated by Fourier filtering, which involves a pre-determined Hamming window function applied in k-space, that defines the filter strength. The filtered phase is then mapped onto a linear phase mask exponentiated to a power Γ, which is typically chosen in the range of $3-5$ to increase the contrast (Haacke et al., 2009). In this case, shape of the mapping function may be considered to consist of an initial rapidly decaying segment (S_1) followed by a plateau region (S_2) extending towards higher phase values. Since the distribution of weights in the phase mask is peaked around unity, the mean weight μ_w is typically closer to unity. This means that a major section of S_1 and S_2 predominantly represent region C_1 with mean weight μ_{C1}, consisting of the noisy pixels and locations representative of susceptibility related information. Although their proportions depend on the filter strength, weights of noisy pixels along with those of faint venous structures assume

values in the interval $[\mu_{C_1}, \mu_w]$. Thus any function having the aforementioned shape features with values in the range [0,1]may be used to construct the mask for contrast improvement.

Although the phase mask can influence the visibility of faint structures as described above, the noisy appearance can only be controlled by the filtering method. One approach to control this is by resorting to spatial high-pass filtering in which the filtered phase is obtained by first unwrapping the phase (Goldstein et al., 1988, Ghiglia and Romero, 1994, Jenkinson, 2003, Li et al., 2014b), and adding the weighted phase differences at each clique with the weights estimated using a function with the phase difference as the input. This form of spatial high-pass filtering is referred to as Weighted High-Pass (WHP) filter. The weighting function is designed based on the idea that larger phase differences are more likely to represent local susceptibility changes in comparison to phase differences closer to zero which represent noise related changes. Here, the dependence of the means μ_w, μ_{C1} and μ_{C2} on the slope of the filter weighting function is used to improve localization of venous structures and reduce the noisy appearance of phase mask.

3.2.1 SWI processing using linear spatial high-pass filter

The phase of a gradient echo acquisition is proportional to both field variation and echo time. The field variation in general occurs due to local susceptibility sources and also due to global geometry of the object. Due to the slowly varying spatial characteristic of background phase, a filter is used to remove it. In general, filtering is achieved either using homodyne method, or by subtracting the averaged phase value of neighboring voxels from the centre voxel. However, neighbourhood operations

require the phase to be unwrapped. For suppressing the background phase using spatial neighborhood based filter, the neighborhood size N_r is dependent on the distance d_r from the brain centre, especially near to the air-tissue interface. At any given location $r \triangleq (m, n)$, the neighbourhood averaged filtered phase is given by

$$\varphi_H(r) = \varphi_H(m,n) = \varphi(m,n) - \sum_{\substack{p,q= \\ -(N_r-1)/2}}^{(N_r-1)/2} \varphi(m+l, n+q)/N_r, \qquad (3.10)$$

where l and q denote indices for a $N_r \times N_r$ neighborhood and φ denotes the unwrapped phase.

Since the estimated background field by variable size filter may violate the harmonic conditions, the background field is estimated from the field data outside the ROI of brain in PDF method. Following background suppression, neighbourhood pixel difference operations are performed for a fixed $N_r = 3$ due to the expected phase variation representative of susceptibility changes in the immediate periphery of venous structures can be safely assumed to be limited to a radius of one voxel thickness. This suggests the possibility of going for a weighted neighbourhood operation to additionally leverage the flexibility of adjusting the weights and fine tune the desired phase mask features.

3.2.2 Weighted high-pass filtering

Depending on the angle between venous structures and the main field, dipolar modulation of the main field causes changes in phase within and outside the venous structure. So a weight applied to the phase difference along the cliques help to correct

the change in phase in vessel boundaries. For this, a non-linear function is designed (eg: an error function), with value approaches to unity for large phase differences. Although in principle, this helps to enhance faint structures, likelihood of noisy edges being enhanced is also high. However, this can be controlled by adjusting the slope of the weighting function.

Let $\varphi = \{\varphi_i | i \epsilon \mathrm{Z}_N\}$where $\mathrm{Z}_N = \{1,2,\cdots,N\}$ represent the unwrapped phase at each voxel. For a 3 × 3 neighborhood system $i \in \{1,2,\cdots,8\}$ represents the 8 neighboring locations of the centre voxel. Then the phase difference from the i'th neighboring location is denoted by $\Delta\varphi_i$. The weights needed for the spatial filtering is estimated from these phase differences. Separate weight functions are designed for left and right handed system (Mehemed and Yamamoto, 2013) as denoted in Eq.(3.11) and Eq.(3.12)

$$\mathrm{W}_i = 0.5\left(1 + erf\left(\frac{(\Delta\varphi_i - 2t)}{t}\right)\right) \tag{3.11}$$

and

$$\mathrm{W}_i = 0.5\left(1 - erf\left(\frac{(\Delta\varphi_i + 2t)}{t}\right)\right) \tag{3.12}$$

where t is the scale parameter. The weight function characteristic curves for increasing t values are shown in Fig.3.3. The slope of the curve is determined by the value of t. With decrease in t value the slope of the weight function increases. The phase differences values which are relatively small are assigned with a weight close to zero or low weights and higher phase differences are assigned higher weights close

to unity. The WHP filtered phase can be computed by summing the weighted phase difference across all the eight neighbourhood directions. Thus a WHP filtered phase is obtained as

$$\varphi_{WHP} = \sum_i \mathrm{W}_i \, \Delta\varphi_i \tag{3.13}$$

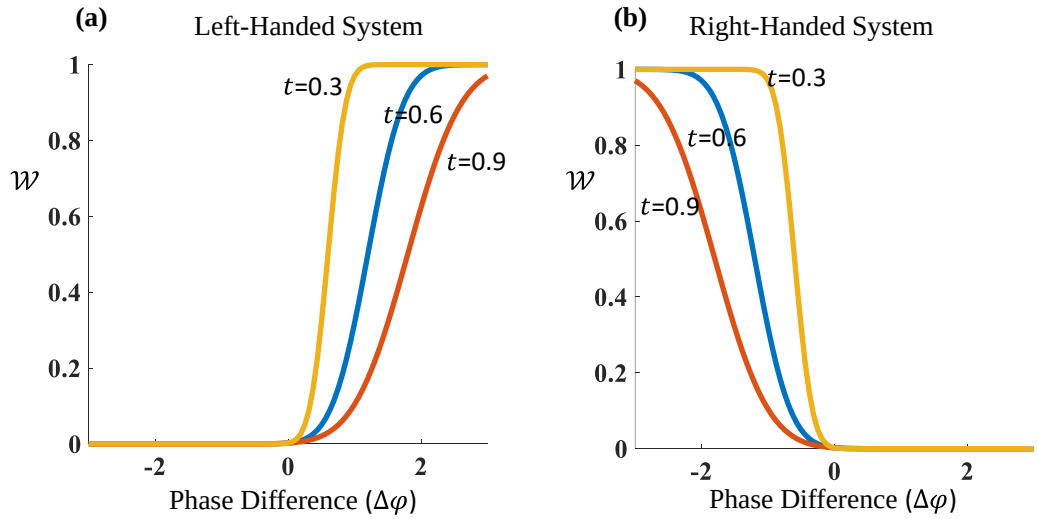

Fig. 3.3: Characteristic curve of filter weight function in WHP filter

3.2.3 Role of filter scale parameter in weighted high-pass filtering

The influence of t in the filtering process can be studied by considering the mean $\mu_w$of the phase mask. The increase in the scale parameter value will lead to increase in the area near to unity, accompanied by decrease in area of the tail region. This in variably relates to regions with two separate intensity based classes $C_1$and C_2, having the respective means$\mu_{C_1} < \mu_w$and $\mu_{C_2} > \mu_w$. Thus the phase mask is considered to have two regions. These include a region C_1 with the mean weight μ_{C1}, representing the veins and other susceptibility related voxels and a region C_2 with the mean μ_{C2}, representing the background locations. The background shift $(\mu_{C_2} - \mu_w)$is indicative

of the variance in the peripheral regions of the veins, whereas the venous shift ($\mu_w - \mu_{C_1}$) is indicative of the retention of venous information. When t is tuned from low to high values, the region C_1 will initially contain a large collection of locations emulating the vein centers. Here, only a subset of these locations will actually represent the true vein centers, while others are simply artifacts of the filter due to the wrong choice of t. As t is increased, the class separation $\left(\mu_{C_2} - \mu_{C_1}\right)$ first increases and then starts decreasing. During this process, number of locations corresponding to the false vein centers will decrease and become minimal once t crosses the peak. This point is reached when the difference between μ_w and μ_{C_1} is maximal. If t is increased beyond this point, then one starts loosing the true vein centers.

3.2.4 Noise Compensation weights

Consider a region comprising of a vein and its edges. It is clear that the vein centre ('c') have a larger phase than the edges ('e'). In these regions where the phase signal shows a negative phase exhibit a low SNR and signal intensity in the magnitude. However for the phase image, the effect of SNR will be different on the edges and centre. This is dependent on the phase distribution conditioned on the intensity of the magnitude at each location and the noise variance (Chung et al., 2002). The phase distribution of the measurement signal with Additive White Gaussian Noise (AWGN), in the real part and imaginary part of the complex data (Aja-Fernández and Tristán-Vega, 2013) is given by,

$$P(\varphi\,|M,\sigma) = \frac{\exp(-\alpha^2)}{2\pi} \times 1 + \left(\sqrt{\pi}\alpha\cos(\varphi-\bar{\varphi})\exp(\alpha^2\cos^2(\varphi-\bar{\varphi}))\right. \\ \left.[1+\mathrm{erf}(\alpha cos(\varphi-\bar{\varphi}))]\right) \quad (3.14)$$

where $\varphi \in [-\pi, \pi)$, $\alpha = M/\sqrt{2}\sigma$, $\bar{\varphi}$ is the average phase value, ρ_m is the magnitude. On measuring the phase, φ_e appears to be closer to zero within the given region, which reveals that as $P(\varphi_e|\rho_m, \sigma) > P(\varphi_c|\rho_m, \sigma)$ .This shows that, the effect of phase values on SNR will be higher at the edges. This points that the neighboring phase difference used in the WHP can be associated with the edges of venous structure by estimating $P(\varphi_e|\rho_m, \sigma)$ and $P(\varphi_c|\rho_m, \sigma)$ for a pair of observations (φ_c, φ_e). Furthermore the joint observation of the two neighboring phase values will be $w_c w_e$ if the measurements are considered to be statistically independent. These pair wise observations of the neighboring phase are then used to deduce the reliability measure that associate central pixel difference to the edge of a susceptibility induced structure.

In pMRI, the AWGN noise model is valid only to the channels images and hence both probabilistic measures are estimated for each channel image. The distribution of noise in the channel image can be assumed to be stationary and not varied spatially across the image location. However, the noise variance changes across the channel, then the combined information from all channels is obtained as

$$w = \left([w_1, w_2, \cdots w_{n_c}] \begin{bmatrix} \sigma_1^2 & \cdots & 0 \\ \vdots & \ddots & \vdots \\ 0 & \cdots & \sigma_{n_c}^2 \end{bmatrix} [w_1, w_2, \cdots w_{n_c}]^T \right)^{\frac{1}{2}}. \qquad (3.15)$$

In the context of weighted high-pass filtering operation all channel observations need to be combined. For this the information obtained from all channels are considered as statistically independent for each pair of observations $(\varphi(m+p, n+q), \varphi(m, n))$ in

a neighbourhood centered at (m,n). Based on the above arguments, a reliability index scaled to the (0,1] range will be

$$W_i(m,n) = 1 - \frac{w(m+p,n+q)w(m,n)}{w_{max}}, \tag{3.16}$$

where the subscript i refers to the i'th neighborhood direction at location pair $((m+p,n+q),(m,n))$ and $w_{max} = Max\{w(m+p,n+q)w(m,n): 1 \le m \le M, 1 \le n \le N, -(N_r-1)/2 \le (p,q) \le (N_r-1)/2\}$. Noise compensation can be introduced to the WHP filtering operation by incorporating the reliability weights as shown in Eq.3.17

$$\varphi_{WHP} = \sum_i W_i W_{Fi}\, \Delta\varphi_i, \tag{3.17}$$

where$W_{Fi}$is the filter weight obtained by using the error functions as sown in Eq. (3.11)-(3.12). Application of the noise compensation weights (W_i)in the WHP filter will help to derive the phase mask that exhibits phase mask with minimum effect of noisy, while retain the structural information for of the venous structures as compared to the phase mask generated without the application of compensation weights.

3.2.5 SWI processing pipeline using WHP filtering and noise compensation

At first, the Laplacian based fast unwrapping method is used to unwrap the measured phase obtained from a GRE acquisition at each channel. The standard deviation of signal intensities outside the brain is computed separately for the real and imaginary

part of the complex data to estimate the noise standard deviation σ_j. In a more general sense, a separate scan is to be performed to measure the noise present at each location and to account for the spatial noise variations due to pMRI reconstruction. Setting these noise estimates as the prior information $P(\varphi_j\,|\rho_{m_j}, \sigma_j)$ is computed using Eq. (3.13) for all voxels. The weights w_j for each channel is computed by multiplying $P(\varphi_j\,|\rho_{m_j}, \sigma_j)$ by $P(\rho_{m_j})$ which is computed from the magnitude ρ_{m_j} image using the normalized histogram. The channel images are then combined using

$$I(m,n) = \sum_{j=1}^{n_C} \frac{C_j^*(m,n)}{\sigma_j^2} I_j(m,n), \tag{3.18}$$

where C_j denotes the channel sensitivity map. After combining the channel images, background suppression is performed followed by WHP filtering. The SWI processing pipeline with WHP and noise compensation is shown in Fig. 3.4.

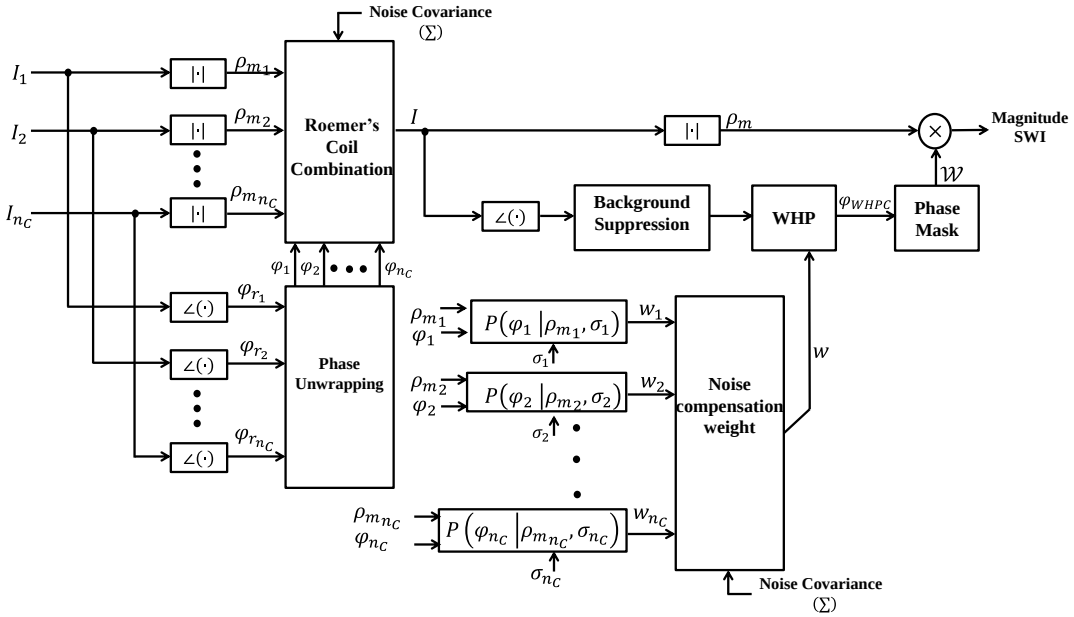

Fig. 3.4: Block diagram for noise compensated WHP filter for SWI processing.

3.3 Multi-echo GRE Phase processing using unity rank enforced complex exponential model

Of late, SWI has increasingly gained importance as a clinical tool for visualization of fine venous structures, bleeds and mineral depositions. Contrast enhancement in SWI has been lately achieved using both non-linear phase filters (Madhusoodhanan et al., 2019), and weighting using the susceptibility map (Gho et al., 2014). Moreover, as the phase wraps and SNR vary widely with echo time, a multi-echo acquisition has always been beneficial for GRE to reduce the spatial distortion and increase the SNR (Helms and Dechent, 2009, Denk and Rauscher, 2010). More significantly, this also allows estimation of a signal model at each voxel after the pre-processing steps applied to remove the phase wrapps and background field (Zhou et al., 2009, Reichenbach et al., 2015). Imperfections in the standard phase pre-processing are known to result in loss of spatial resolution and SuR information (Funai et al., 2008, Dagher et al., 2014). Therefore, an important challenge in SWI is to recover the lost details in regions with high phase wraps and bulk field inhomogeneities.

Although refinements in phase pre-processing have resulted in minimizing the signal errors, it is impossible to recover the lost information without introducing corrections in the signal model. For example, when imaging a brain slice with dural sinus, phase wraps and bulk field inhomogeneities are usually high. Tweaking the signal model after phase pre-processing as proposed in this work, enables the visualization of venous structures in the cerebral peduncle and choroid plexus. Due to the bulk field variations introduced by the interpeduncular cistern, these venous structures are usually not enhanced in standard SWI. Additional venous structures between the

superior and middle temporal gyrus near to the sinus regions are also seen enhanced in the magnitude SWI using the corrected signal model.

The signal models are based on the linear predictability of the multi-echo signals such as that employed in MORASA (Peng et al., 2016). In this, a parametric signal model with a decaying exponential fit along temporal direction is used to enhance the features. This relies on the use of linear predictability of the exponentially decaying magnitudes in the temporal signals at each voxel, which are modelled to enforce low rankness of a structured matrix constructed from the vector of samples at each location (Cadzow, 1988). This technique is well suited for spin echo sequence and turbo spin echo sequence, whose temporal signal evolution is modelled as a combination of decaying exponentials and image phase support is shared at all TEs.

In the case of GRE acquisition with sufficiently long TE, out of phase spins in the voxels result in phase dispersion that causes loss of signal intensity (Port and Pomper, 2000). The resultant signal model for the magnitude intensities along temporal direction loses the linear predictability due to the sinc function modulation of the magnitudes (Brown et al., 2014). Thus in situations where the echoes are few in number, the required number of samples to deduce the signal model for the magnitude component (such as the sinc function) may not be adequate. This makes it difficult to apply an intermediate correction procedure. Therefore, introduction of the magnitude intensity into the model fitting can significantly influence the phase estimate. This effect is more pronounced particularly in regions with signal dropout and also those having low intensities that sometimes can overlap with areas containing the venous structures to be restored.

In the case of SWI, one needs to correct the local phase after supressing the bulk field inhomogeneity in the combined channel images. The voxel-wise signal can be conceived to be one consisting of a single complex exponential representing the frequency relating to the susceptibility induced field. Thus by fitting a complex exponential with only a single frequency, it is possible to apply a unity rank approximation (URA) of the structured matrix along the temporal dimension. This is formulated as an optimization problem, and implemented using alternating direction method of multiplier (ADMM) with variable splitting (Boyd et al., 2011, Gabay and Mercier, 1975).

3.3.1 Phase pre-processing for URA-SWI

The phase of a multi-echo GRE sequence is given by

$$\psi_r^l = 2\pi\gamma\Delta B_r(\mathrm{TE}^0 + l\Delta\mathrm{TE}) + \Omega_r^l + 2\pi\epsilon_r^l, \tag{3.18}$$

where ΔB_r represents field value at location r, TE^0 is the initial TE, $\Delta\mathrm{TE}$ is the difference in TE, l corresponds to TE index, $l = 0,1,2 \ldots, L-1$, L is the total number of TE used, Ω^l is the phase contribution from additive noise term, and ϵ_r^l is the phase wrapping term. To observe the local SuR information in the phase image, phase unwrapping (Schofield and Zhu, 2003, Li et al., 2014b, Jenkinson, 2003)and background field removal is performed (Schweser et al., 2010, Zhou et al., 2014, Liu et al., 2011a, Madhusoodhanan et al., 2019).

3.3.2 Low Rankness in Multi-echo data

The signal generated using a GRE sequence at a given TE is given by (Liang and Lauterbur, 2000, Nguyen et al., 2009)

$$g_r^l = \rho_r^l \exp\{i\psi_r^l\}, \tag{3.19}$$

where ρ_r^l is the signal intensity measured at location r for echo index l. In acquisition with more than one echo, the reconstructed images are denoted as g^0, g^1, $\cdots$, g^{L-1}. Prior to application of URA to the phase component of g, one needs to apply phase unwrapping and background suppression as its effect becomes more severe at higher echo times. Let φ^l be the phase image obtained after unwrapping and background suppression of ψ^l. Since the Kronecker's theorem (Beylkin and Monzón, 2005) is valid only for complex symmetric matrix, a unit magnitude complex exponential signal is constructed from the background suppressed phase. For a given location r, the collection of unit magnitude complex exponential signals at each TE is modelled as a uniformly sampled signal with a single frequency component. This is given by

$$x_r = \begin{bmatrix} e^{i\varphi_r^0} \\ e^{i\varphi_r^1} \\ \vdots \\ e^{i\varphi_r^{L-1}} \end{bmatrix} = \begin{bmatrix} e^{i2\pi\gamma\Delta B_r(\mathrm{TE}^0)+\widehat{\Omega}_r^1} \\ e^{i2\pi\gamma\Delta B_r(\mathrm{TE}^0+\Delta\mathrm{TE})+\widehat{\Omega}_r^2} \\ \vdots \\ e^{i2\pi\gamma\Delta B_r(\mathrm{TE}^0+(L-1)\Delta\mathrm{TE})+\widehat{\Omega}_r^L} \end{bmatrix} \tag{3.20}$$

To permit further analysis on x_r, a common approach is to map the one dimensional signal x_r to a multi-dimensional structured Hankel matrix. Using the window length (w) as the parameter for mapping such that $2 \leq w \leq L$ (Gillard, 2010), the structured Hankel matrix H_r is constructed as

$$\mathrm{H}_r = \begin{bmatrix} e^{i\varphi_r^0} & e^{i\varphi_r^1} & \cdots & e^{i\varphi_r^{w-1}} \\ e^{i\varphi_r^1} & e^{i\varphi_r^2} & \cdots & e^{i\varphi_r^w} \\ \vdots & \vdots & \ddots & \vdots \\ e^{i\varphi_r^{L-w}} & e^{i\varphi_r^{L-w+1}} & \cdots & e^{i\varphi_r^{L-1}} \end{bmatrix}, \tag{3.21}$$

In this case, w is choosen such that the Hankel matrix would be complex symmetric square Hankel, so that singular value decomposition (SVD) for rank minimization can be performed in minimum number of flops (Peng et al., 2016, Xu and Qiao, 2008). Since the elements of the Hankel matrix H are uniformly sampled points with single frequency component, it can be considered as a matrix with rank R=1.

In practical conditions, due to noise in the measured signal, the lower singular components of the Hankel matrix H may not be zero. Therefore singular values of H can be truncated to obtain a minimum variance estimate. Then the reconstructed signal is estimated from rank minimized H by averaging across its anti-diagonal elements. This step helps in iterative filtering of the signal model (Gillard, 2010). To maintain consistency with the measured phase after background suppression, a fidelity term is added along with the rank prior. The estimate of the underlying true phase representative of the SuR information can hence be obtained from an optimization problem formulated as:

$$\min_{\varphi} \frac{1}{2} \left\| e^{i\varphi} - e^{i\hat{\varphi}} \right\|_2^2 \; subject\ to\ rank\ \left(\mathcal{H}\left(e^{i\hat{\varphi}} \right) \right) = N, \tag{3.22}$$

where φ and $\hat{\varphi}$ are the measured and true phase image, $\mathcal{H}$ denotes an operator which operates on a data matrix of size $N \times L$, N is the number of elements in the 2D image and L is the number of echoes. The operator is defined such that for each row of the data matrix, a square Hankel matrix of dimension $\frac{L+1}{2} \times \frac{L+1}{2}$ can be created and placed in diagonal order to generate a 2D matrix of size $N * \left(\frac{L+1}{2}\right) \times N * \left(\frac{L+1}{2}\right)$ with rank N. Alternatively, the minimization problem in Eq. (3.24), applied to each location r, is given by

$$\min_{y_r} \|x_r - y_r\|_2^2 \qquad subject\ to\ rank\ (\mathrm{H}_r) = 1 \tag{3.23}$$

where x_r and y_r denote the measured and the original complex exponential signal at location r, with unit magnitude. Since constructing a 2D matrix of size $N * \left(\frac{L+1}{2}\right) \times N * \left(\frac{L+1}{2}\right)$ and performing rank minimization by SVD is computationally intense, rank minimization is performed on the Hankel matrix constructed at each location. Hereafter, the pixel subscript r is dropped for simplicity in representation. Using ADMM formulation, the above rank minimization problem takes the form

$$\begin{aligned} &\min_{\mathrm{H,u}} \mathbb{R}(\mathrm{H}) + \frac{\lambda}{2}\|u\|_2^2, \ \ subject\ to \\ &\qquad \mathrm{H}(j,k) + u(j+k) = x(j+k);\ 0 \le j,k \le M, \end{aligned} \tag{3.24}$$

where $u = x - y$, $\mathrm{M} = \frac{L-1}{2}$, λ is a regularization parameter and $\mathbb{R}(\cdot)$ is the indicator function defined as

$$\mathbb{R}(\mathrm{H}) = \begin{cases} 0 & if \quad rank\ (\mathrm{H}) = 1 \\ \infty & otherwise \end{cases}. \tag{3.25}$$

Since the cost function consist of two terms, each depending only on one of the variable H and u, the problem formulated in Eq. (3.24) is well suited to be addressed using ADMM. Although the phase expressed as complex exponential in the fidelity term facilitates the ADMM implementation, it makes the cost function non-convex due to the periodicity of the complex exponential (Zhao et al., 2012). However, since the background suppressed GRE phase always exhibit values in the range $(-\pi, \pi]$, the cost function can be treated to be convex in the current context (Liu et al., 2017). This additionally favours the convergence to a global minimum. For obtaining the

ADMM solution, it is required to consider the augmented Lagrangian function of Eq.(3.24):

$$\mathcal{L}(\mathrm{H}, u, z) = \mathbb{R}(\mathrm{H}) + \frac{\lambda}{2}\|u\|_2^2 + \sum_{j,k=0}^{M} z(j,k)[\mathrm{H}(j,k) + u(j+k) - x(j+k)] + \sum_{j,k=0}^{M} \frac{\delta}{2}|\mathrm{H}(j,k) + u(j+k) - x(j+k)|^2 , \tag{3.26}$$

where z is the Lagrange multiplier, and δ is the step parameter or penalty parameter. The iterative steps from iteration q to $q+1$ for ADMM implementation, involve solving the following subproblems:

$$\mathrm{H}^{q+1} = \min_{\mathrm{H}} \mathbb{R}(\mathrm{H}) + \sum_{j,k=0}^{M} \frac{\delta}{2}\left|\mathrm{H}(j,k) + u^q(j+k) - x(j+k) + \frac{1}{\delta} z^q(j,k)\right|^2 \tag{3.27}$$

$$u^{q+1} = \min_{u} \frac{\lambda}{2}\|u\|_2^2 + \sum_{j,k=0}^{M} \frac{\delta}{2}\left|\mathrm{H}^{q+1}(j,k) + u(j+k) - x(j+k) + \frac{1}{\delta} z^q(j,k)\right|^2 \tag{3.28}$$

$$z^{q+1} = z^q(j,k) + \delta[\mathrm{H}^{q+1}(j,k) + u^{q+1}(j,k) - x(j+k)] \quad for\ 0 \le j,k \le M \tag{3.29}$$

The solution to subproblem-1 can be obtained from the proximal version of Eq. (3.27), given by

$$\mathrm{H}^{q+1} = \underset{\frac{\mathbb{R}(\mathrm{H})}{\delta}}{\mathrm{prox}} \textstyle\sum_{j,k=0}^{M} [x(j+k) - u^q(j+k) - \frac{1}{\delta} z^q(j,k)] \tag{3.30}$$

The updated H^{q+1} is then obtained using nuclear norm minimization of H, which can be computed by singular value thresholding (SVT) of a matrix B_m defined as

$$B_m(j,k) = x(j+k) - u^q(j+k) - \frac{1}{\delta} z^q(j,k) \; for \; 0 \le j,k \le M \; . \qquad (3.31)$$

With the SVT of $B_m = U\Sigma V^*$, the updated H becomes

$$H^{q+1} = U\Sigma_1 V^*, \qquad (3.32)$$

where Σ_1 is obtained from the diagonal matrix Σ by truncating to the highest singular value. This is because the matrix H constructed from the complex exponential of multi-echo signal at each location ideally contains a single frequency component. For second minimization step, the solution $u^{q+1}$is obtained by equating the derivative of the cost function to zero. i.e.,

$$\frac{\partial \Psi(u)}{\partial u} = 0, \qquad (3.33)$$

where $\Psi(u) = \frac{\lambda}{2}\|u\|_2^2 + \sum_{j,k=0}^{M} \frac{\delta}{2} \left| H^{q+1}(j,k) + u(j+k) - x(j+k) + \frac{1}{\delta} z^q(j,k) \right|^2$.

The solution for Eq. (3.33) is given by

$$u^{q+1}(l) = \frac{Q(l)\delta x(l) - \sum_{j+k=m} [\delta H^{q+1}(j,k) + z^q(j,k)]}{Q(l)(\lambda + \delta)}, \qquad (3.34)$$

where$0 \le l \le L-1$ and

$$Q(l) = \begin{cases} l+1 & if \quad l \le M \\ 2M+1-l & otherwise \end{cases}$$

After updating of H and u, the Lagrange multiplier can be updated using

$$z^{q+1}(j,k) = z^{q}(j,k) + \delta[\mathrm{H}^{q+1}(j,k) + u^{q+1}(j+k) - x(j+k)] \quad (3.35)$$

$$for\ 0 \le j,k \le M$$

Algorithm is stopped when the tolerance $\tau = \frac{(u^{q+1}-u^{q})}{u^{q}} \le 10^{-3}$.

To generate a symmetric square Hankel matrix for the case where L is even, the vector x_r can be split into two vectors ${}^{1}x_r$ and ${}^{2}x_r$ using first and last $(L-1)$ elements of x_r. The two Hankel matrices ${}^{1}\mathrm{H}$ and ${}^{2}\mathrm{H}$, each of size $\frac{L}{2} \times \frac{L}{2}$, can be constructed by choosing the window length $w = \frac{L}{2}$ (Golyandina et al., 2001). To compute ${}^{1}u$ and ${}^{2}u$, the minimization procedure can then be performed separately on ${}^{1}x_r$ and ${}^{2}x_r$. The first and last element of the solution u can be directly obtained from the first element of ${}^{1}u$, and the last element of ${}^{2}u$. The rest of the elements of u can be estimated by averaging the last $(L-2)$ elements in ${}^{1}u$ and the first $(L-2)$ elements in ${}^{2}u$.

3.3.3 URA processing pipeline

The phase of channel combined complex signal was first pre-processed by phase unwrapping and background suppression to remove the bulk field variations. For reconstruction with URA prior at each location, the unit magnitude complex exponential signals along the temporal direction were used to construct a square Hankel matrix. Singular value thresholding was then performed on the Hankel matrix by retaining the highest singular value and principal singular vectors. To restore the Hankel structure, each matrix element was replaced by the mean of its cross-diagonal elements. By iteratively continuing the rank minimization together with imposition of

data fidelity constraint, empirical convergence was observed in terms of the relative l_2-norm error between phase images of successive iterations. The phase image generated after attaining convergence was used for either SWI processing. The proposed processing pipeline is shown in Fig.3.5.

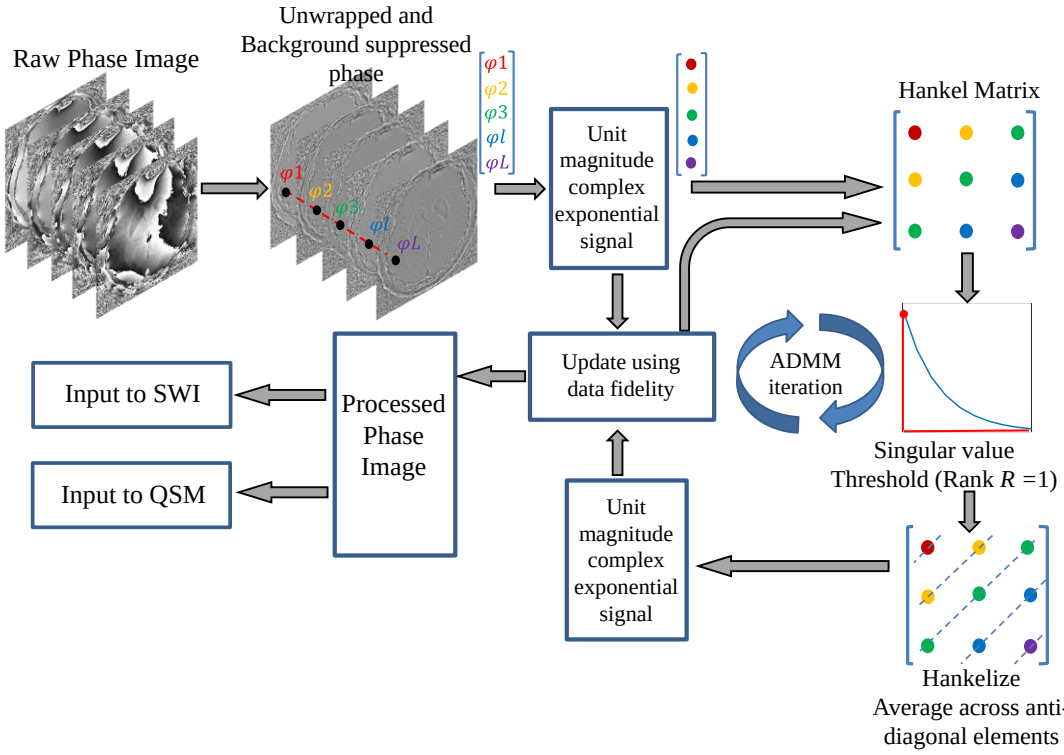

Fig. 3.5: Schematic block diagram of URA processing pipeline.

3.3.4 Choice of regularization parameter

One of the main parameter to control the performance of ADMM iteration is the regularization parameter (λ) used to update the unit magnitude complex exponential. Here λ controls the extent of update in a single iteration. The value of λ was determined by an adhoc search procedure that involved solving Eq. (3.26) using different values of λ, and choosing the one that minimizes the deviation cost. Another parameter that controls the performance of ADMM is the penalty

parameter(δ) for the violation of linear constraints. Since an analytical approach for automatic selection of this parameter is currently not known, heuristic methods are usually proposed to choose the value of δ (Liu et al., 2013b, Iordache et al., 2013, Trémoulhéac, 2015). In all experiments, the specific value of the penalty parameter was fixed to $\delta = \frac{N}{4\|x\|_1}$ as proposed by Benjamin et al. (Trémoulhéac, 2015).

CHAPTER 4

RESULTS

4.1 Data Acquisition

Data acquisition for this study uses GE 3.0 T Discovery MR750W and Siemens Magnetom Avanto1.5 T scanners. The acquisition parameters for the two scanners are listed in Table 1 below. Fifty subjects with age ranges from 24 to 76, with an average age of 62 years, were used in this study. Among this four are volunteer scans. Number of patients recruited for each neurological condition are-: 1) tumor 4(6), 2) stroke 4(8), 3) microbleed 4(6), and 4) dementia 4(10) (Number of patients scanned in 3.0 T scanners is shown in brackets). Institute ethics committee approved this study and written informed consent was obtained from all subjects.

Table.4.1: Scan parameters.

Scan parameters	1.5 T Siemens	3.0 T GE
TR	49 ms	35 ms
TE	40 ms	24.5 ms
FA	20°	15°
Slice Thickness	2.2 mm	2.4 mm
Matrix	186 × 230	288 ×384
FOV	203 × 250 mm^2	168×240 mm^2
Bandwidth	80 Hz/pixel	325.52 Hz/pixel
Average	1	1
No. of rx channels	12	12

4.2Application of GRADER algorithm in SWI data

GRADER algorithm was applied to multi-channel multi-echo data and observed that the convergence rate of the algorithm differs in each channel images and across the echoes. Table.4.2 depict the initial scale parameter ts_{01} and the iterations needed for each channel to reach the convergence. The value of the cost function for the pre-

determined range of ts values is shown in the first row in Fig. 4.1. Left-right panel (a1)-(a4) shows the plots of $\mathcal{J}$ at four different iteration ($k = 1,3,5\ and\ 7$). The ts_{01}value for channels-2, 4, 6 and 8 are shown in the second row.

Table 4.2: Optimum scale parameter value$ts_{01}^{(1)}$and total number of AM iterations required for each channel

Channel	SIEMENS 1.5T Data		GE 3T Multi Echo Data					
	Echo-1 (TE = 40 ms)		Echo-1 (TE = 20 ms)		Echo-2 (TE = 24.68 ms)		Echo-3 (TE=29.36 ms)	
	$ts_{01}^{(1)}$	Iterations	$ts_{01}^{(1)}$	Iterations	$ts_{01}^{(1)}$	Iterations	$ts_{01}^{(1)}$	Iterations
1	0.0992	10	0.0446	4	0.0482	10	0.0555	10
2	0.0848	7	0.0518	4	0.0591	7	0.0664	10
3	0.0365	4	0.0373	4	0.0446	6	0.0518	9
4	0.0992	10	0.0409	6	0.0482	5	0.0518	9
5	0.0543	5	0.0373	6	0.0409	7	0.0482	9
6	0.0581	6	0.0337	6	0.0373	7	0.0446	7
7	0.0594	6	0.0373	5	0.0409	6	0.0482	7
8	0.0848	10	0.0373	4	0.0446	6	0.0482	7
9	0.0848	7	0.0482	4	0.0518	7	0.0591	8
10	0.0992	10	0.0409	6	0.0518	6	0.0555	9
11	0.0992	10	0.0482	5	0.0518	7	0.0627	7
12	0.0746	6	0.0446	5	0.0518	6	0.0591	8

It is observed that value of ts_{01}decreases as the AM iteration progress and requires 6-10 iterations to reach a steady state. The processed channel phase images at four AM iterations are shown in panel (c1)-(c4). Images obtained after processing the Siemens 1.5 T data using MIR-SWI and GRADER is shown in Fig. 4.2. Column wise panel shows the processed phase images, phase masks, and SWI image. From panel (a3) and (b3) it is observed that the venous structures are better preserved in

GRADER while controlling granularity when compared to the images obtained after MIR-SWI. Arrow heads are used to point-out the structures preserved while using the GRADER algorithm. Quantitative evaluation of the filter performance was performed using vein based CNR (*VB-CNR*) measure defined as (Borrelli et al., 2015)

$$VB - CNR = \frac{S_{OUT} - S_{IN}}{\sigma}, \quad (4.1)$$

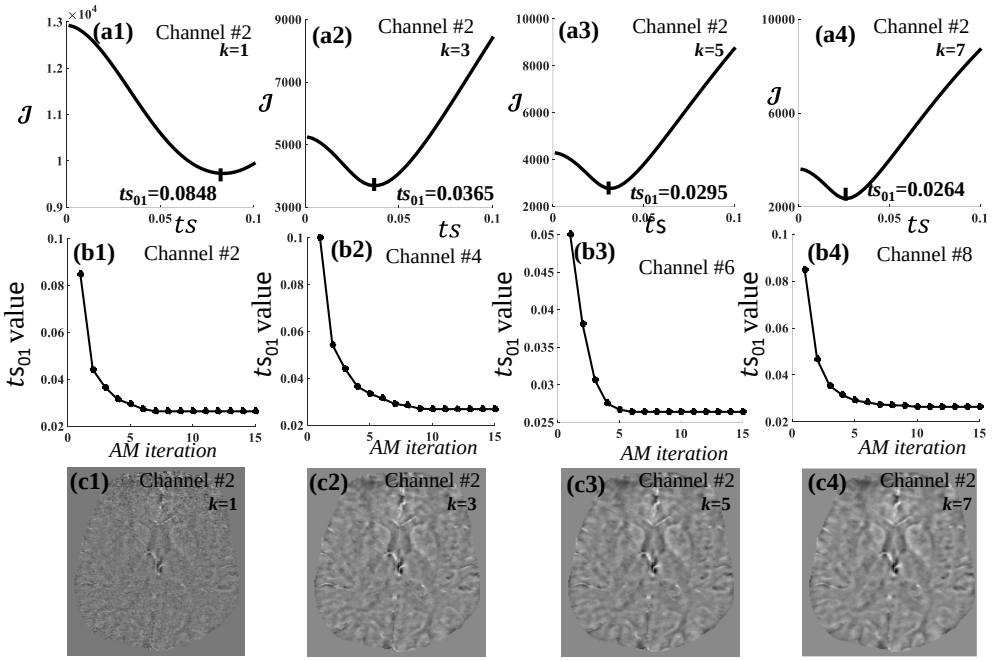

Fig. 4.1: Application of GRADER to channel phase images at 1.5T scanner with TE= 40 ms and TR= 49 ms. Top row shows the plot of $\mathcal{J}$ for a single channel and the second row shows the convergence plot of AM iterations for different channels (2,4,6& 8 of a 12 channel dataset). Bottom row (c) shows the denoised phase images for a single channel at different iterations (1, 3, 5 and 7).

where S_{IN} is the mean intensity of the venous location (red) and S_{OUT} represents the mean intensity at the regions near to the vein (blue line), as highlighted in Fig. 4.2(a3)-(b3). σ is the standard deviation, computed from the region where there are no venous information. Panels (c) and (d) in Fig. 4.2 shows the *VB-CNR* profile at

location marked with blue line in panel (a3) and (b3) obtained after MIR-SWI and GRADER.

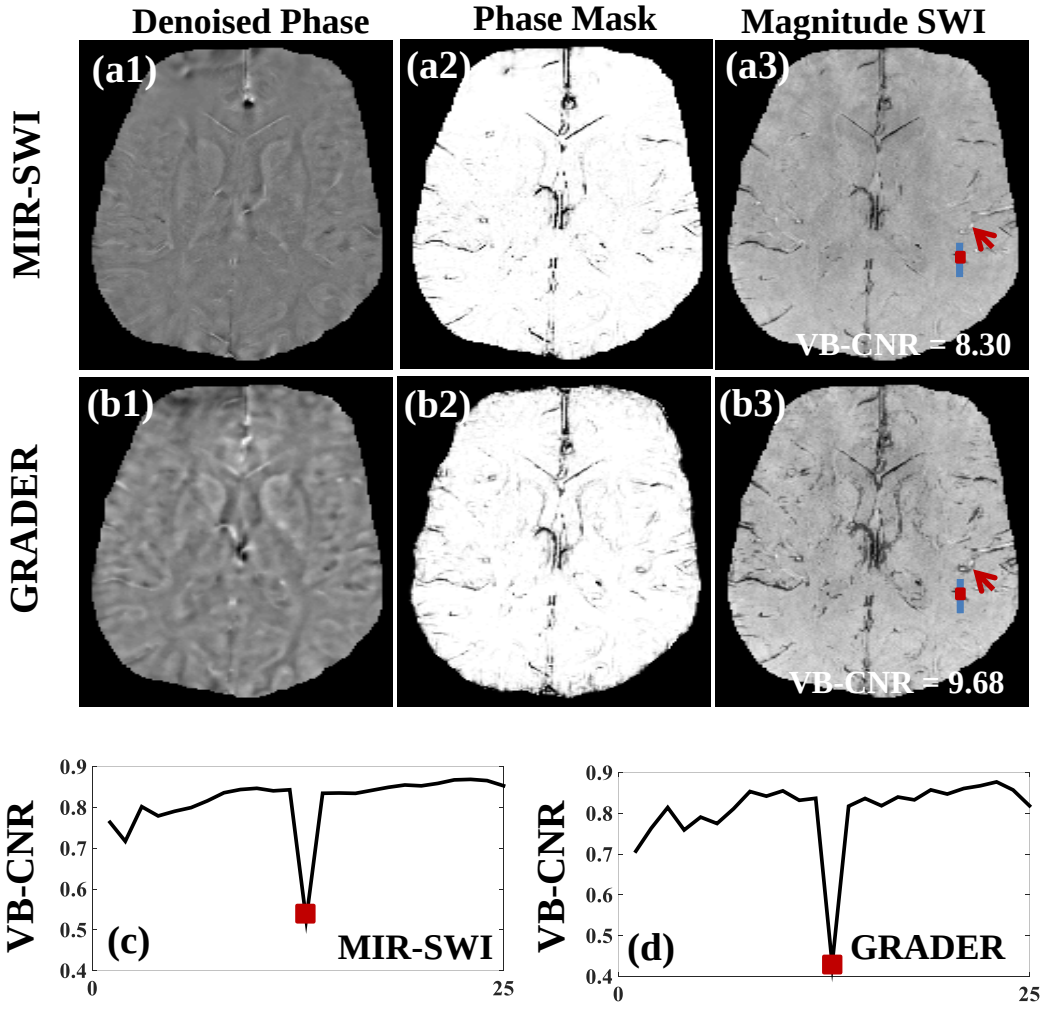

Fig. 4.2: Application of MIR-SWI (first row) and GRADER (second row) to 1.5 T data. Voxel intensity at the chosen ROI (blue line in SWI image) is shown in panels (c) MIR-SWI and (d) GRADER.

For datasets acquired with multi-echo susceptibility weighted angiography (SWAN) sequence, it is observed that as the TE increases ts_{01} also increases for each channel. This is in conformity with the actuals that signal acquired at higher echoes have lower SNR. Two channel phase images are obtained after processing is shown in Fig.4.3. The ts_{01} value (shown in insets) decreases with AM iterations. Fig. 4.4 shows the combined phase, phase mask, magnitude SWI and minimum intensity

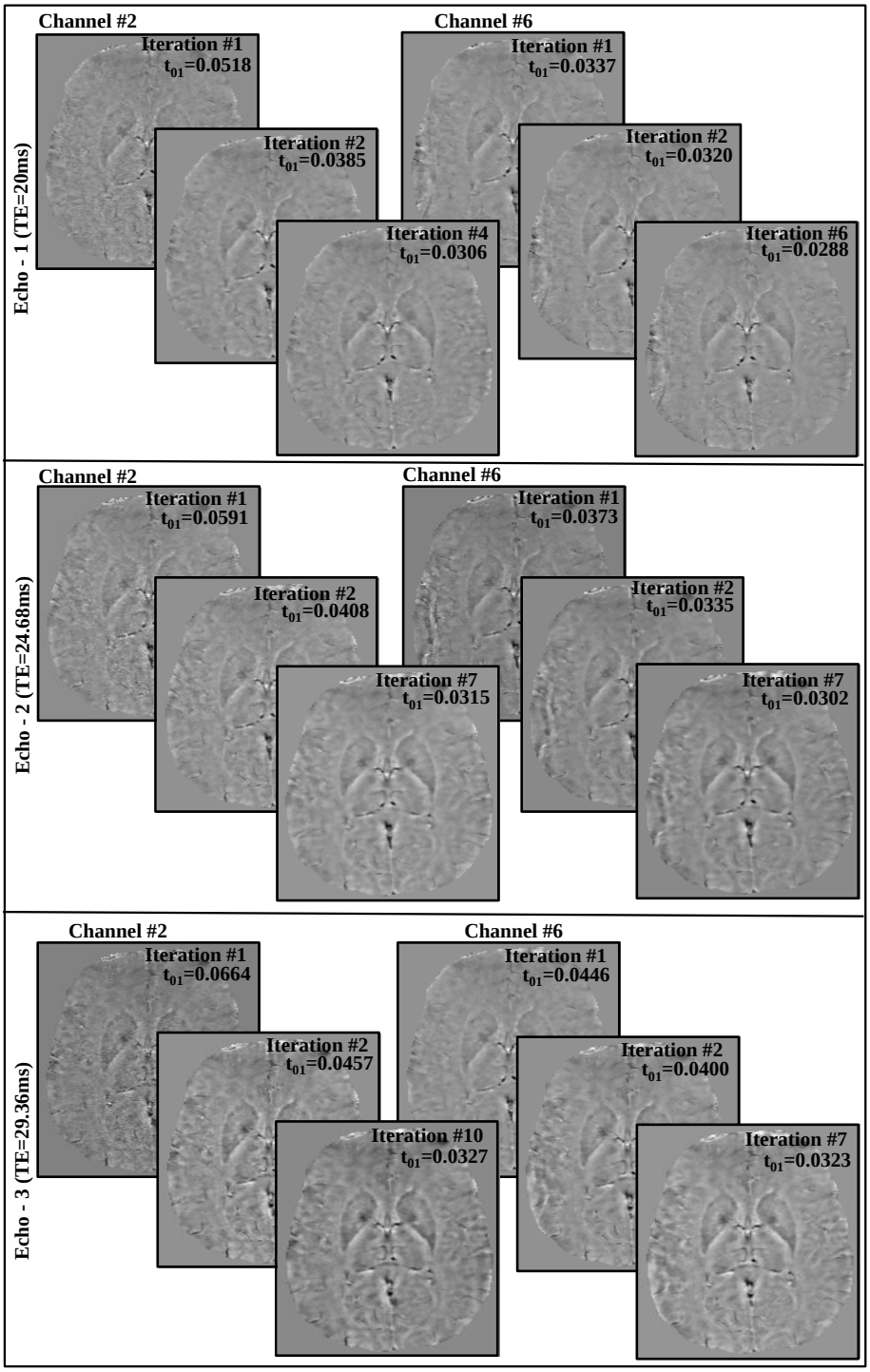

Fig. 4.3: Application of GRADER to multi-echo SWAN images with 12 channel, TE=24.7 ms and TR =34.0ms. The multi-echo data includes three echoes with interval 4.68 ms. The initial TE is set to 20 ms. Two channel phase images are shown in left and right column. Denoised phase images of three echoes are shown in row wise panels.

projection (mIP) over eight slices obtained using MIR-SWI (top row) and IR-GRADER (second row). Similar to the earlier observation using 1.5 T data, multi-echo SWAN 3.0 T images obtained after GRADER exhibit faint structures with increased contrast after removing granularity. The *VB-CNR* profile is shown in the bottom row of Fig. 4.4(c)-(d).

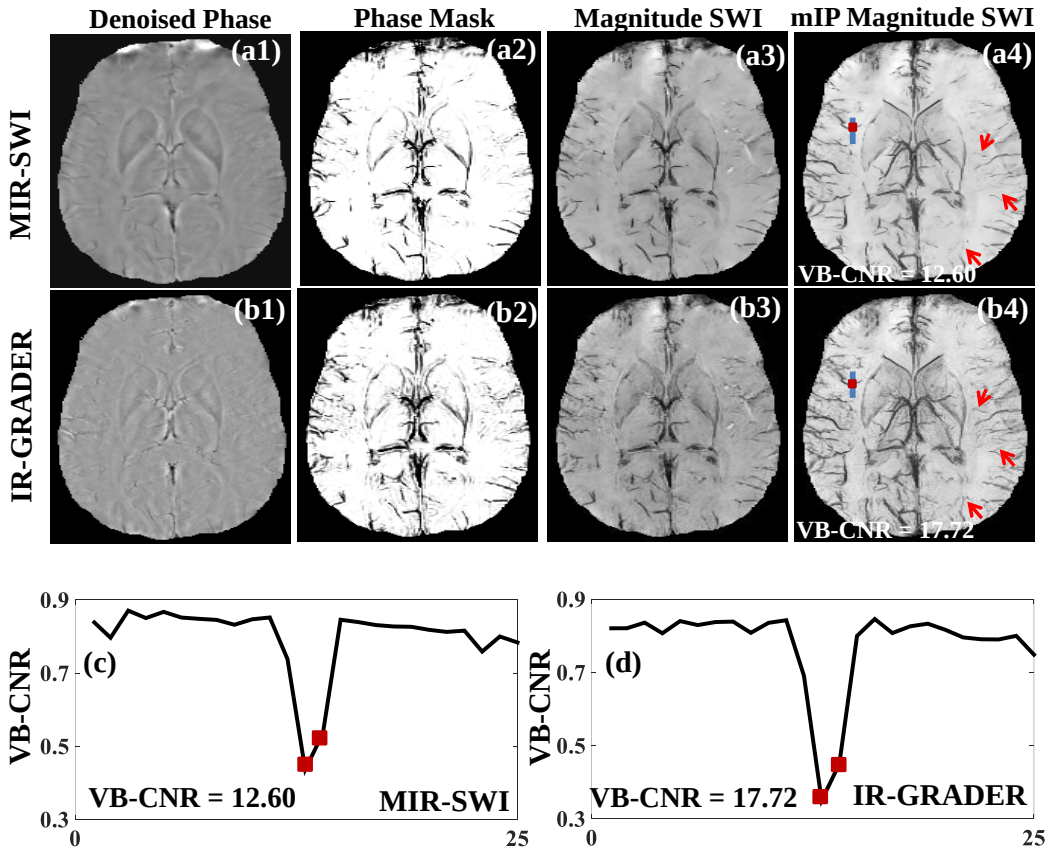

Fig. 4.4: Application of MIR-SWI (first row) and GRADER (second row) to 3.0T SWAN data. Arrow heads indicate the venous structures preserved after the application of GRADER. Pixel intensities at the ROI marked with blue line in the mIP image is shown in last row. (c) MIR-SWI and (d) GRADER.

To evaluate the performance of the filter, a 5-point scoring of image quality by considering the features including gray-white matter distinction, prominence of vein, noise reduction and identification of mineralization of globus pallidus (GP). On qualitative evaluation both the methods score equally for visualizing deep veins.

However for identifying superficial veins and nucleus with iron depositions, pMRI-GRADER scored better than the MIR-SWI.

4.2.1 SNR and Contrast using GRADER

Development of contrast in the processed magnitude image with AM iteration is demonstrated using a multi-echo data as shown in Fig.4.5. Column wise panel show the contrast evolution for different channel images. With the application of the IR-GRADER algorithm as discussed in section 3.1.5, SNR and CNR improvements were calculated in frontal white matter and basal ganglia region respectively. The contrast of the images is computed as the ratio of the difference in signal intensity between two regions to the noise variance. In this case the signal intensity difference between frontal white matter and basal ganglia region is used to measure the contrast. To measure the noise variance of each channel image, variance calculated at different white matter region is averaged. Similarly the ratio of mean signal intensity to the noise standard deviation is computed to calculate the SNR. An interesting observation while computing the CNR is that as the effect of noise increases, the number of iterations required to reach the convergence increases, this is evident in slow convergence of late echoes. Since the IR-GRADER controls the noise in real part and imaginary part, both the magnitude SWI and the mask created from the phase images shows an improvement in the contrast. Bottom row in Fig.4.5 shows the magnitude SWI generated without and with IR-GRADER at two echo levels. Panels (e) and (g) show SWI images obtained without IR-GRADER at two different TE. Similarly panels (f) and (h) show SWI images obtained with IR-

GRADER. Improved contrast is observed in the SWI generated after processing with IR-GRADER.

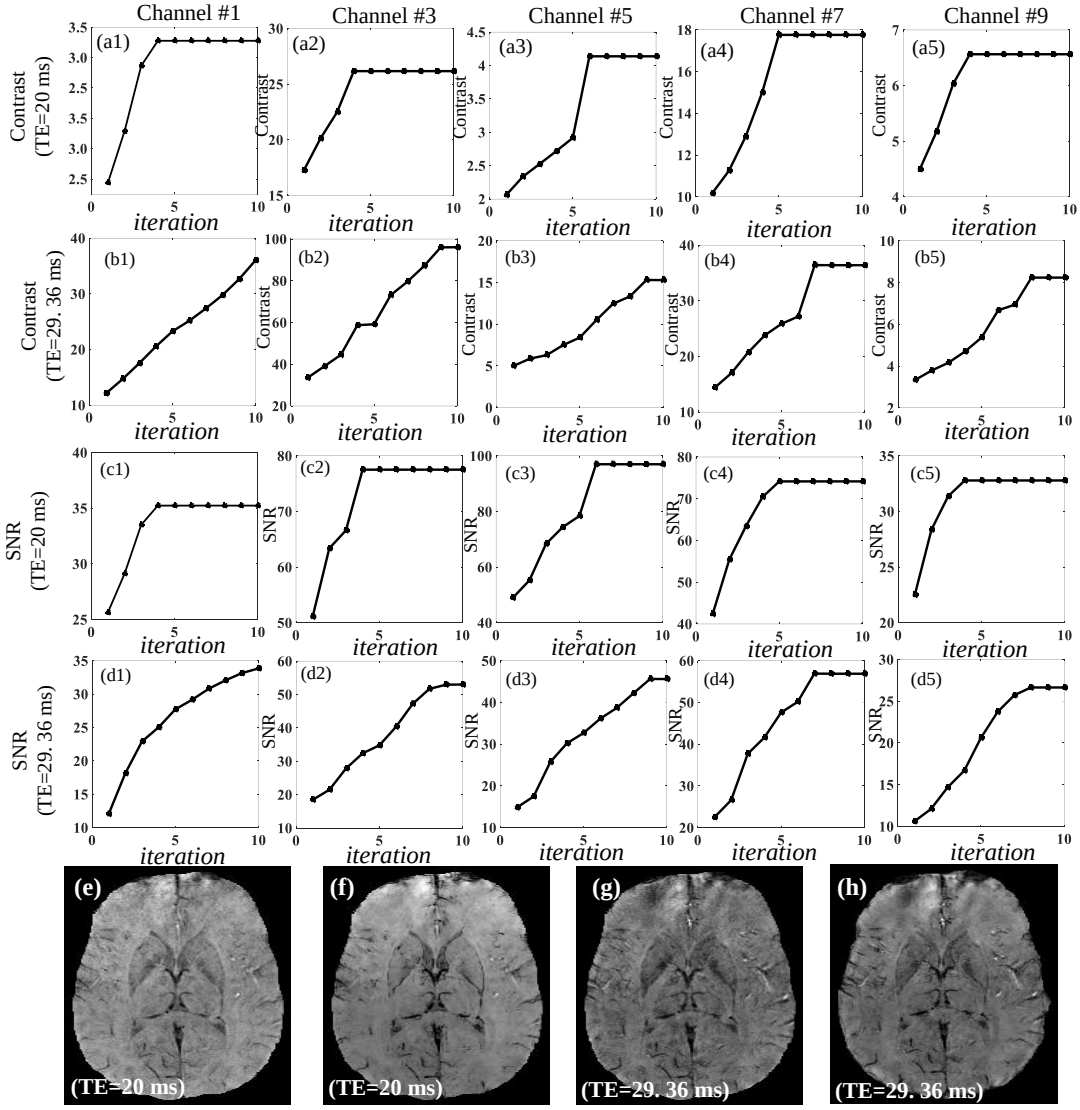

Fig. 4.5:SNR and Contrast evolution with iterations in IR-GRADER. Top two rows show the contrast evolution with iteration in (a) early echo and (b) late echo, Third and fourth row show the SNR evolution with iteration in (c) early echo, (d) late echo for channels-1,3,5,7& 9. (e) and (f) corresponds to magnitude SWI obtained without and with IR-GRADER for early echo, similarly (g) and (h) corresponds to late echo.

At later TE SWI generated without IR-GRDER shows high level of granularities. Reduction in granularities and improved contrast is observed in panel-(h) computed using IR-GRDER.

4.3 Spatial high-pass filtering in SWI

4.3.1 Determination of filter scale parameter for spatial high-pass filtering

The filter parameter is equivalent to the filter strength in HHP filter and filter scale parameter in WHP filter. In HHP filter the filter strength is defined by the window size normalized by the image size. The influence of filter parameter on the statistics of the phase mask $\mathcal{W}$ is shown in Fig 4.6. On changing the filter parameter on a pre-determined limit $[0.01,0.4]$ the statistics of $\mathcal{W}$ is computed which includes the mean vaule of phase mask (μ_w), and mean of the two regions C_1 and C_2. Here the region C_1 corresponds to locations with intensities less than μ_w and C_2 corresponds to locations with intensities greater than μ_w. The mean value at these two regions are represented as μ_{C1} and μ_{C2}. As the filter parameter increases all these statistical means are seen to increase as shown in panels (a). Panel-b shows the mean separation between $\mu_w$and μ_{C_1}. It is observed that when compared to HHP filter, the WHP filter exhibit an improved mean separation of 56%. Moreover at the desired t value WHP filter shows a maximum difference in mean separation. Top and bottom panel shows the results observed for HHP and WHP filters. Sample phase mask at five different filter parameters are shown in panel (c). When the filter parameter is small, filter induced artifacts are seen in the phase mask. With the increase in the filter parameter artifact are reduced with reduction in SuR information. It is observed that the reduction in SuR information is more in HHP filter when compared to WHP.

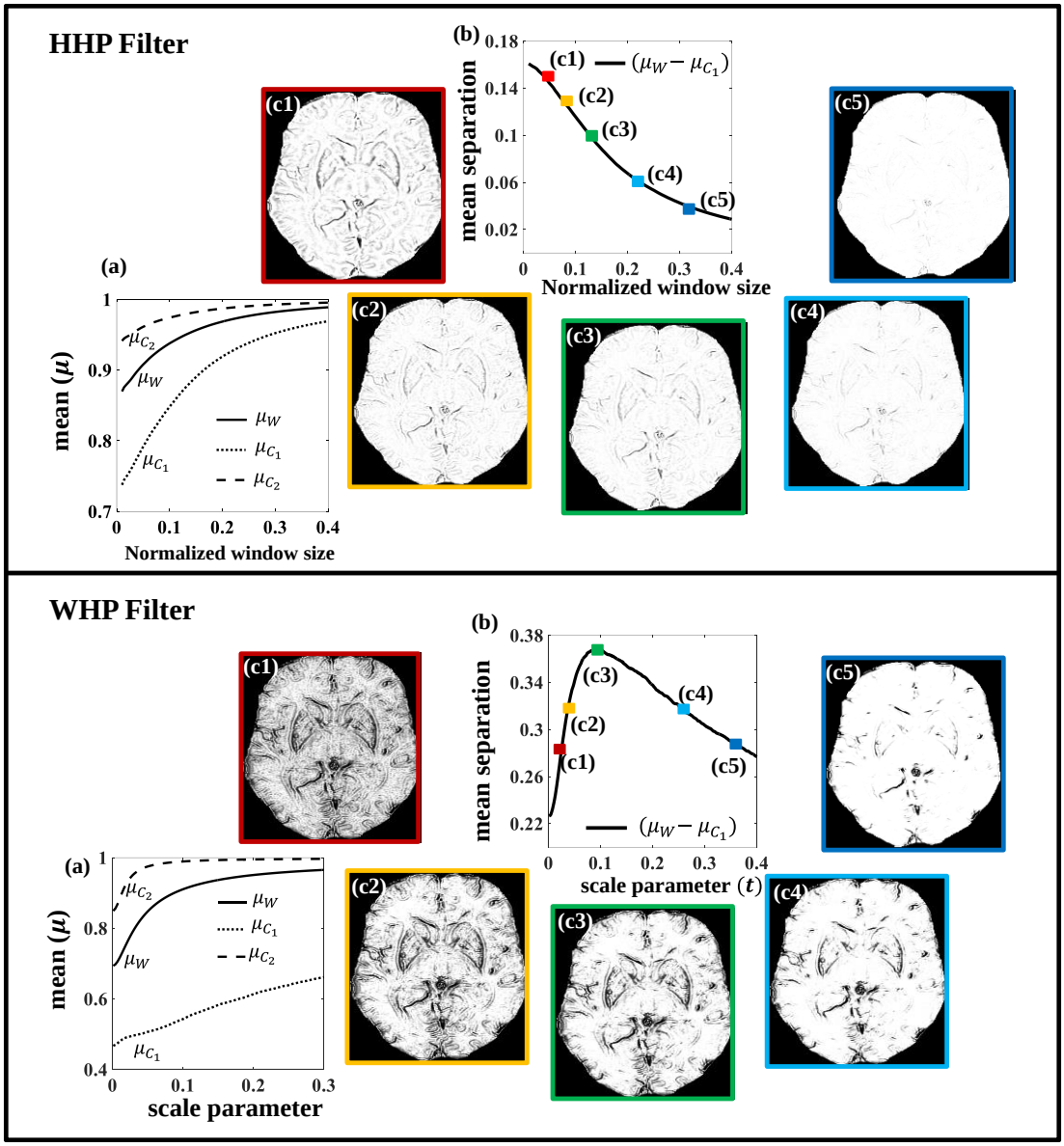

Fig.4.6: Change in Mean separation with respect to the filter parameter. The filter parameter for HHP filter is the normalized window size and for WHP filter it is the scale parameter t. Panel (a) shows the plots of μ_w, μ_{C_1} and μ_{C_2} as function of filter parameter, Mean separation with respect to filter parameter is shown in panel (b), (c1-c5) corresponds to the phase mask obtained at five sample filter parameter values.

4.3.2 Effect of WHP and WHPC filter on CNR

Quantitative evaluation of the three filtering scheme (HHP, WHP and WHPC) was performed using *VB-CNR* at three ROIs labelled R1, R2 and R3. Row wise panel in Fig 4.7 shows the pixel intensities at each ROI. Left- right panels show the type of

filtering scheme used (HHP (Blue), WHP (Green) and WHPC (Orange)). Advantage of WHP and WHPC processing over HHP is clearly shown by the increase in *VB-CNR*.

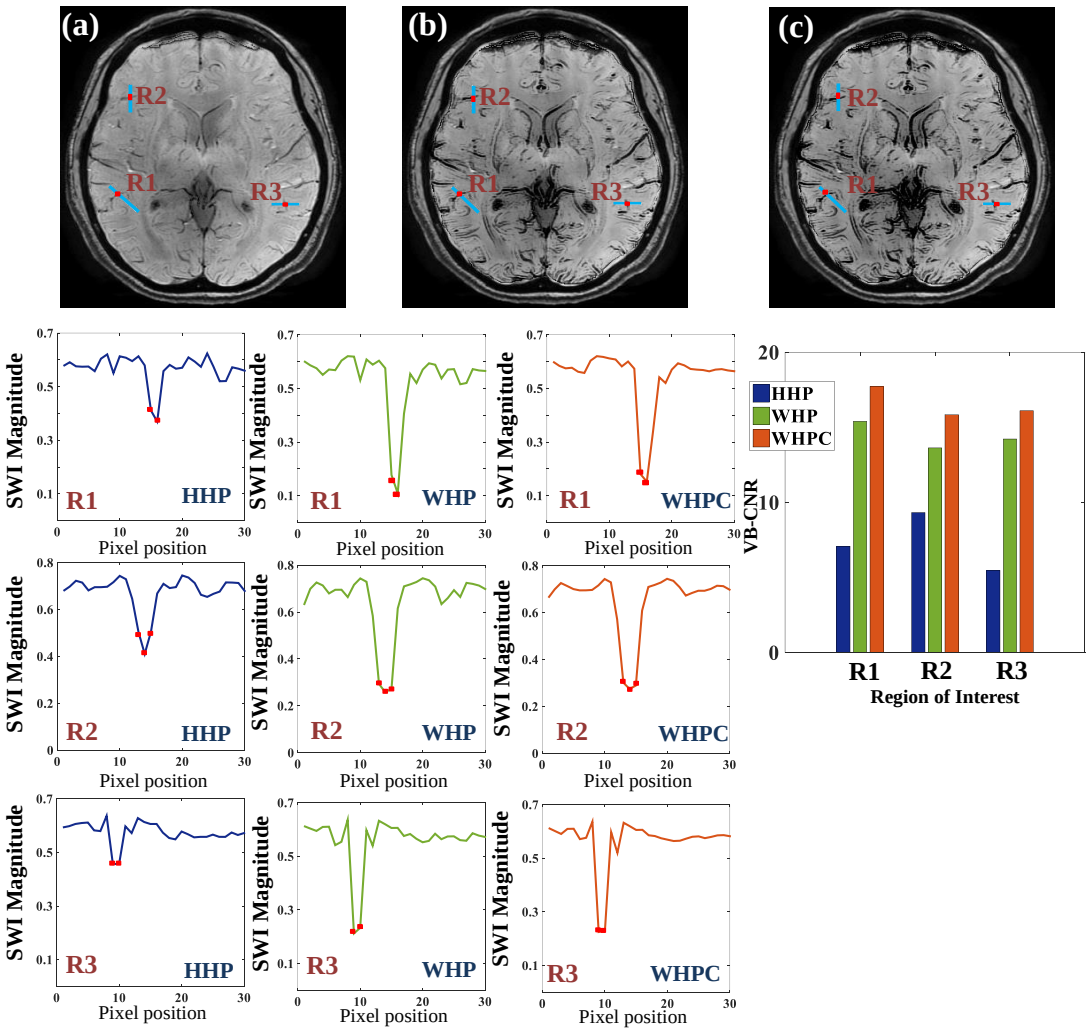

Fig.4.7: Vein-based CNR (*VB-CNR*) analysis of SWI image. *VB-CNR* was measured for three ROIs (R1, R2 and R3). Column wise panel corresponds to the three filtering scheme HHP, WHP and WHPC. SWI images obtained using the filtering schemes are shown in the first row (a) HHP, (b) WHP and (c) WHPC filters. Row-wise panels correspond to intensities across the ROIs R1, R2 and R3.Red dot in each plot indicate the venous center.

4.3.3 Application of spatial high-pass filtering to in vivo clinical studies

Quality improvement in SWI using the proposed WHP and WHPC filter provides a mean to visualize the multiple hemorrhagic foci and micro bleeds. The relative increase in phase shift between the ROI and the reference regions gives an indication of the amount of mineral deposition in that region. For example the relative change in filtered phase, between the basal ganglia structure and cerebro-spinal fluid (CSF) indicates the amount of iron deposition at that region.

Sample mIP magnitude SWI images with clinical findings like tumor, stroke, microbleed and dementia are shown in Figs.(4.8 - 4.11). Left to right panel in each figure shows the resultant mIP images generated after processing the phase using HHP, WHP, and WHPC filters. Top and bottom row corresponds to data acquired at 3.0 T and 1.5 T. In in all these cases the prominence of veins is observed to be high when processed with WHP and WHPC filters. It is also observed that the venous contrast in WHP and WHPC are relatively same, but the WHP appears noisier than WHPC filter. CNR computed at the ROI marked with blue lines in the mIP images show the superiority of the WHPC filter for reducing the noise without reduction in venous contrast. The percentage improvement of CNR for WHPC over HHP is 68.40% and between WHPC and WHP filter is observed to be 18.63 %.

In Fig. 4.8 shows the mIP images of subject with tumor. Blooming of peripheral structural wall due to hyper acute bleeding is more pronounced in mIP obtained with WHP. Peripheral blooming along with improved visualization of cortical veins shows the superiority of WHPC. When compared to images obtained after HHP, visualization of thin and faint venous structures are clearer in WHP and WHPC as

indicated by the red arrow heads. Even though venous information are prominent in WHP, it exhibit a noisy appearance which is addressed in WHPC though the application of noise compensation weights. Panels (b) depict glioma with microbleeds identified near the sylvian fissure and insular region. The microbleeds are better identified together with venous structures inside the glioma (see the red arrow head) using WHPC compared to HHP and WHP.

In Fig. 4.9(a), multiple bleed spots are identified in the basal ganglia region. Only two out of three micro hemorrhagic bleed near right putamen, are seen in the mIP derived using both HHP and WHP. While the other bleed appears faint, mIP derived using WHPC enables improved visualization of all the three microbleed foci with sufficiently high blooming (indicated by thick red arrow). Also bleeding near the right globus pallidus region appears clearly with higher blooming in WHP and WHPC than in HHP as indicated by the red arrow heads. For bleeding in intra ventricular space as shown in panels (b), blooming in hemorrhagic transformation appears high in WHP and WHPC. Same as the earlier observation, WHP and WHPC filter shows better visibility of venous structures as indicated by red arrows.

Micro hemorrhage is seen in bilateral basal ganglia and subcortical white matter in Fig. 4.10(a). It is observed that microbeelds are more hypointense and easily noticeable in mIP image derived using WHPC. Along with microbleed points venous structures are more prominent in WHP and WHPC as indicated by red arrow. Yellow arrow heads highlight these bleed points. Panels (b) show mIP images with SWI blooming in the frontal white matter and right parietal region. Contrast of trans-medullary veins and SWI blooming is more in mIP SWI derived using WHP and

WHPC filter. Although the cortical venous information is clearly depicted in mIP SWI derived using WHP, it exhibit a noisy appearance which is compensated in WHPC and helps in easy identification of micro haemorrhagic bleeds. Yellow arrow heads indicate higher blooming of the bleeding points and red ones highlight improved visualization of the venous structures with WHPC.

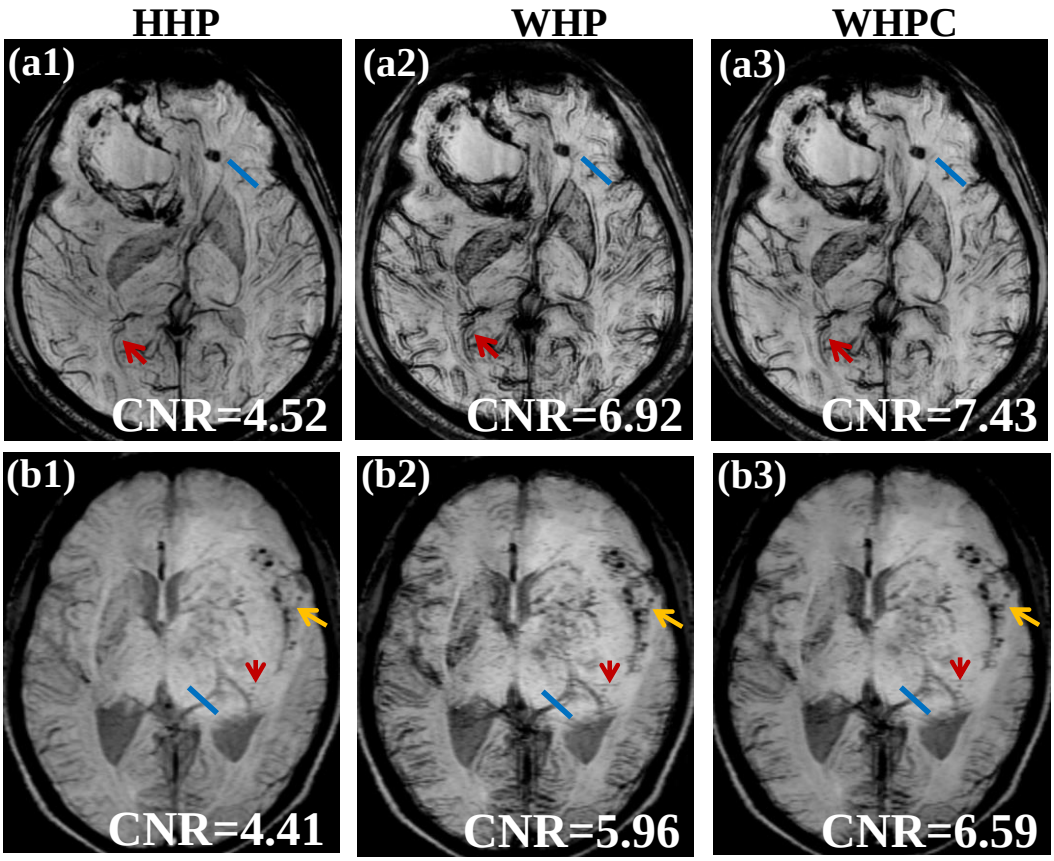

Fig. 4.8: Row wise panels show the mIP images over 8 slices of 3.0 T data (slice thickness 2.0 mm) and 1.5 T data (slice thickness 2.4 mm) for subjects with brain tumor. Column wise panel depict the mIP SWI images obtained using (1) HHP, (2) WHP, and (3) WHPC filters. Red arrows and yellow arrow is used to indicate the improved visualization of vein and bleed spot.

It is well known that the iron depositions in basal ganglia structures are more. Therefore the hypo-intense appearance of globus pallidus and putamen structure in Fig. 4.11 indicates that the spatial high-pass filtering enhances the SuR features and improves the visibility of SWI images.

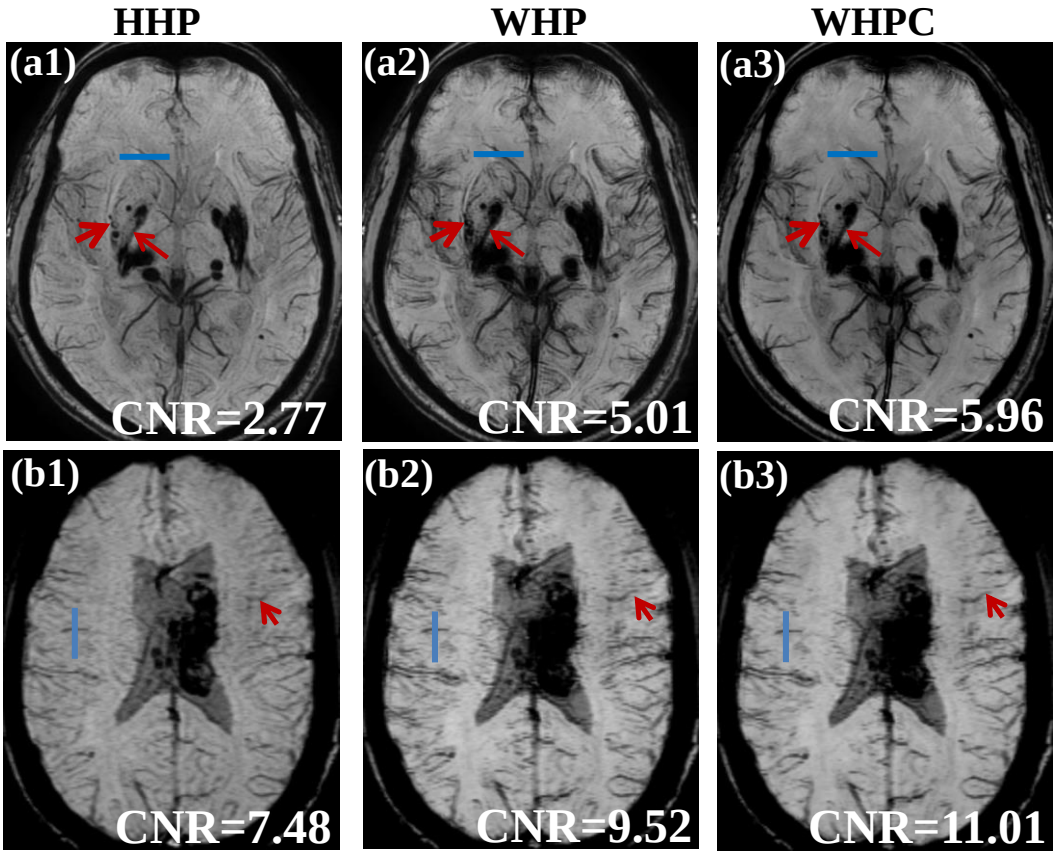

Fig. 4.9: Row wise panels show the mIP images over 8 slices of 3.0 T data (slice thickness 2.0 mm) and 1.5 T data (slice thickness 2.4 mm) for subjects with hemorrhagic bleed. Column wise panel depict the mIP SWI images obtained using (1) HHP, (2) WHP, and (3) WHPC filters. Bleed foci of interest (top row) is highlighted using red arrow. Increase in prominence of vein is seen in mIP images generated using WHP and WHPC.

To illustrate the filter performance at two field strength, same volunteer is scanned at both 1.5 T and 3.0 T with same in-plane resolution (448×364) and slice thickness 2 mm. The SWI images generated from these dataset is shown in Fig.4.12. Top two panel (a) and (b) corresponds to data acquired at 1.5 T and 3.0 T. The column-wise panels show SWI images generated using the HHP, WHP, and WHPC filters. Furthermore, the VB-CNR computed across a venous object in the region highlighted using the blue line is shown in the insets. The VB-CNR value indicates the superiority of WHPC filter to increase the contrast of the venous structures. Bottom

two rows (c) and (d) show the VB-CNR profile for the SWI images at two field strength.

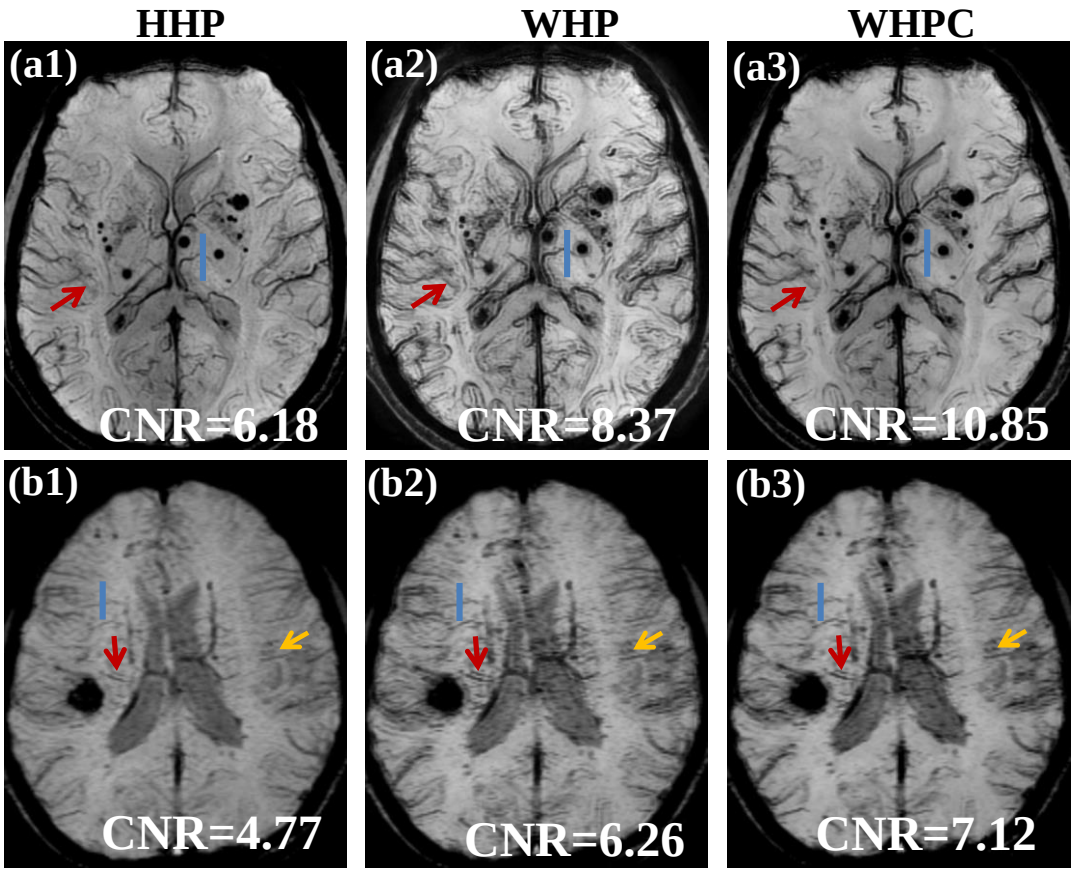

Fig. 4.10: Row wise panels show the mIP images over 8 slices of 3.0 T data (slice thickness 2.0 mm) and 1.5 T data (slice thickness 2.4 mm) for subjects with microbleed. Column wise panel depict the mIP SWI images obtained using (1) HHP, (2) WHP, and (3) WHPC filters. The red arrow indicates improved visualization of venous structures and yellow arrows are used to indicate microbleeds whose prominence increase with the application of WHP and WHPC filters.

4.3.4 Statistical Analysis

Paired t-tests are performed to evaluate differences in mean separation for all the filtering methods discussed above. Fig. 9(a1)-(a4) shows the mean separation observed in tumor, stroke, microbleed and dementia, respectively, with the p-values for each combination indicated by (*) for $p < 0.001$and (#) for $p < 0.05$.

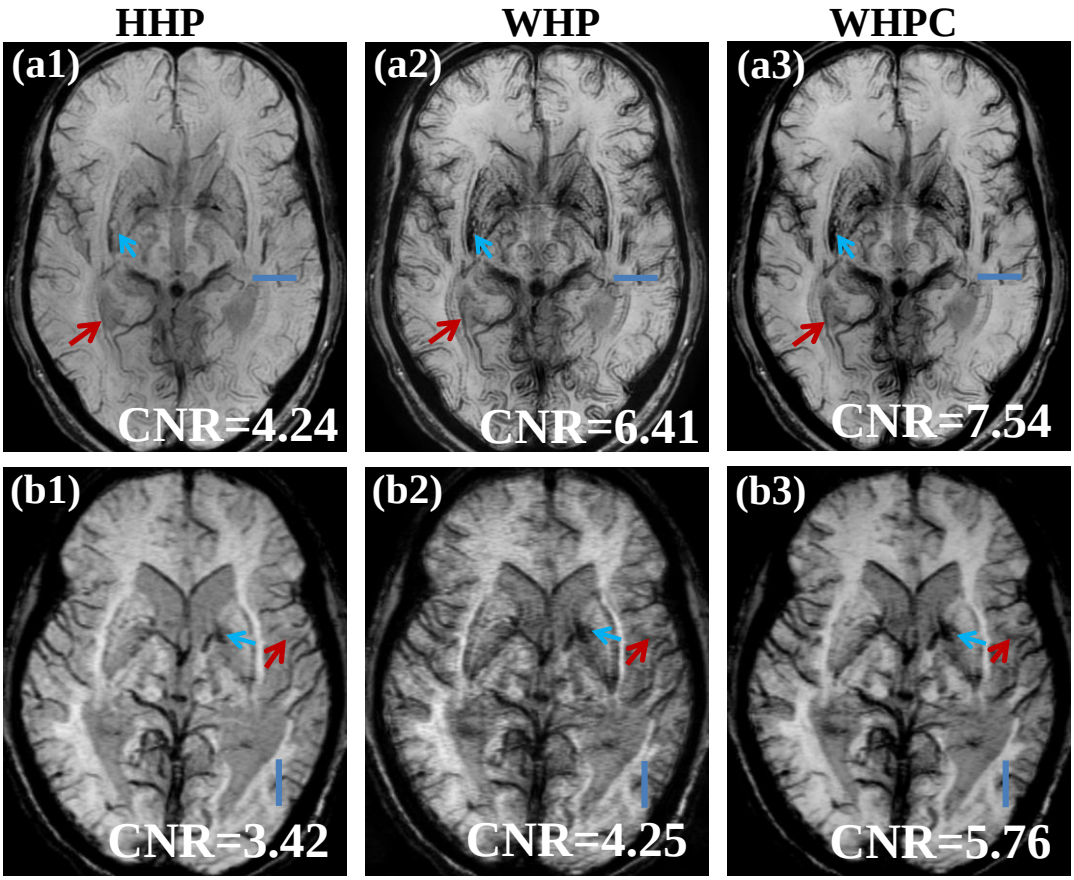

Fig. 4.11: Row wise panels show the mIP images over 8 slices of 3.0 T data (slice thickness 2.0 mm) and 1.5 T data (slice thickness 2.4 mm) for subjects with mild cognitive impairment. Column wise panel depict the mIP SWI images obtained using (1) HHP, (2) WHP, and (3) WHPC filters. Blue arrow head indicates the improved visualizations of iron deposition and red arrow indicate improved visualization of venous structures.

As reported in the previous studies where relative phase difference between the fronto-temporal white matter and basal ganglia structure are used to measure the quantity of iron depositions (Sheelakumari et al., 2017), phase values at the chosen ROIs are compared with the reference CSF. Two ROIs include the globus pallidus (GP) and putamen (PT). Significance level of the relative phase difference is measured using paired t-tests. Bottom panel in Fig. 4.13 shows the bar graph of mean phase values of ten dementia patients at the chosen ROI (CSF, GP and PT). Panels

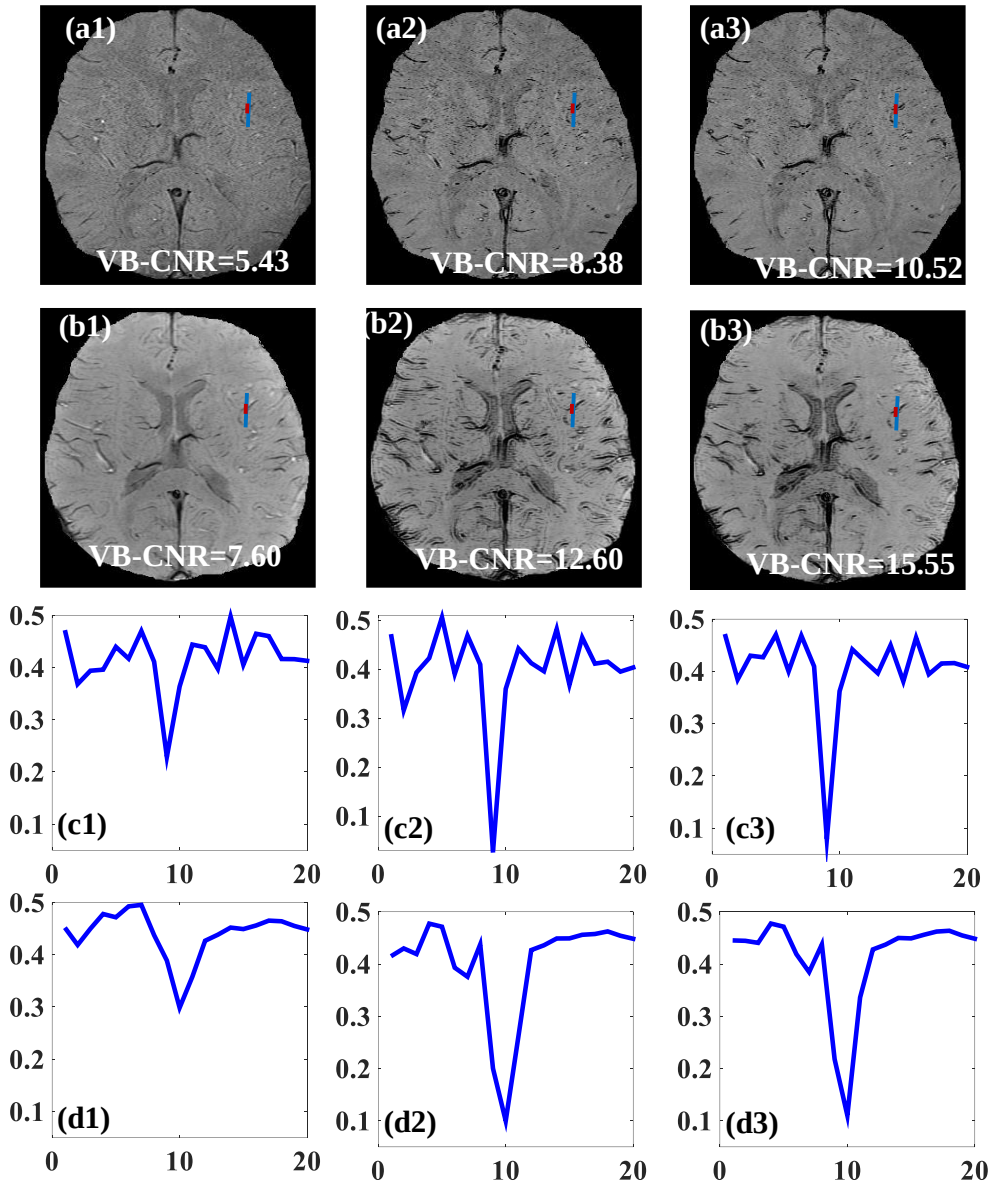

Fig.4. 12: Left-to-right panels show SWI images obtained using (1) HHP, (2) WHP, and (3) WHPC filters for same subjects. Top two rows show the SWI images generated from GRE data acquired at field strength 1.5 T and 3.0 T, with slice thickness 2.0 mm and resolution(448×364), respectively. Bottom two rows show the *VB-CNR* profile of SWI images.

(c1) correspond to the phase values in CSF and GP. and (c2) corresponds to CSF and PT. For each filtering scheme the p-values are also marked alongside. It is observed that among the three filter scheme, the WHPC filter shows the highest significance level with a p-value $p < 0.001$.

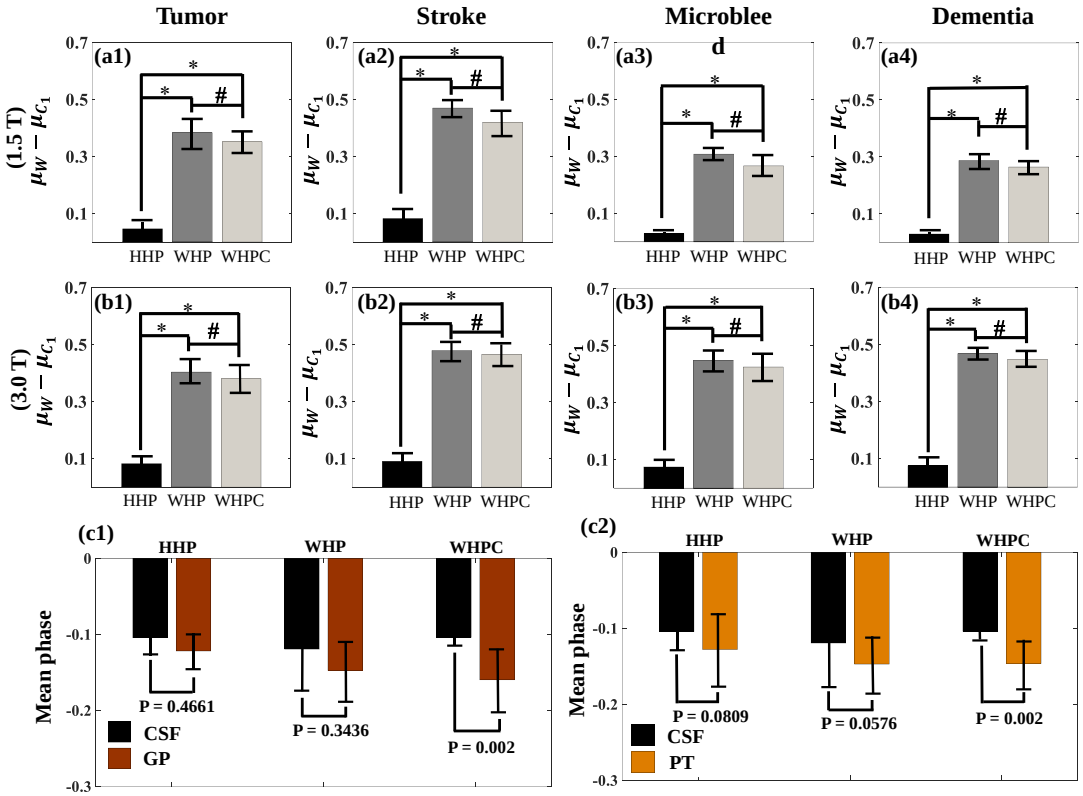

Fig. 4.13: Top two rows show the mean-separation for 1.5 T and 3.0 T data. Column wise panel shows the bar graphs for tumor, stroke, microbleed and dementia data. The symbols (*) and (#) in each panel correspond to significance levels of 0.001 and 0.05, respectively. Panels (c1) correspond to the phase values in CSF and GP and (c2) corresponds to CSF and PT. The observed p-values after paired t-test were shown for each filtering scheme.

4.4 Application of URA prior to SWI processing

Fig. 4.13 shows sample phase images of a multi-echo SWAN sequence, before and after reconstructing the phase with URA prior (first and second row). Column-wise panels show the phase images at TE= 20 ms, 24.6 ms, 29.3 ms, and the echo-combined phase. In the combined phase images, yellow arrows indicate the newly observed transverse veins that are not seen in the unprocessed combined phase image. Furthermore, the improved gray-white matter contrast in the processed phase image enables better visualization of the white matter tracks. The blue arrow in the combined phase points to the white matter track between lentiform nucleus and

insular region that is hardly seen in the unprocessed phase image. The empirical convergence of the phase reconstruction scheme is shown using the relative l_2-norm error between the phase images estimated in successive iterations.

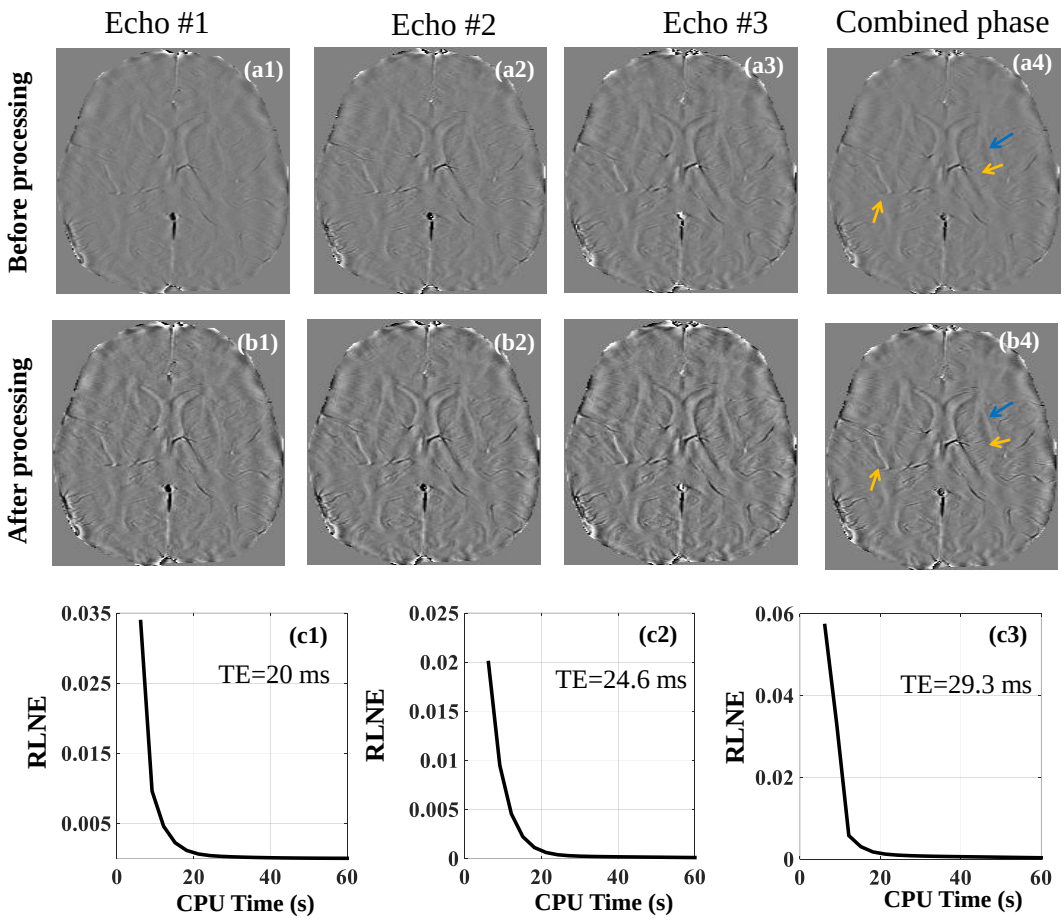

Fig. 4.14: Top two panels show the unprocessed phase image and phase image reconstructed with URA prior. Column-wise panels show phase images at $TE = 20$ ms, 24.6 ms, 29.3 ms and the echo-combined phase. Yellow and blue arrows are used to indicate the newly observed transverse veins and white matter tracks in the combined reconstructed phase image. Bottom row shows the empirical convergence of the phase reconstruction algorithm for three echo times.

Fig. 4.14 illustrates the application of URA prior in SWI processing. The combined phase, phase mask, and magnitude SWI obtained without and with URA prior are shown in the left and right panels, respectively. Red arrows indicate the faint

transverse and medullary venous structures that are highlighted only in the magnitude SWI generated using the phase image reconstructed with URA priors.

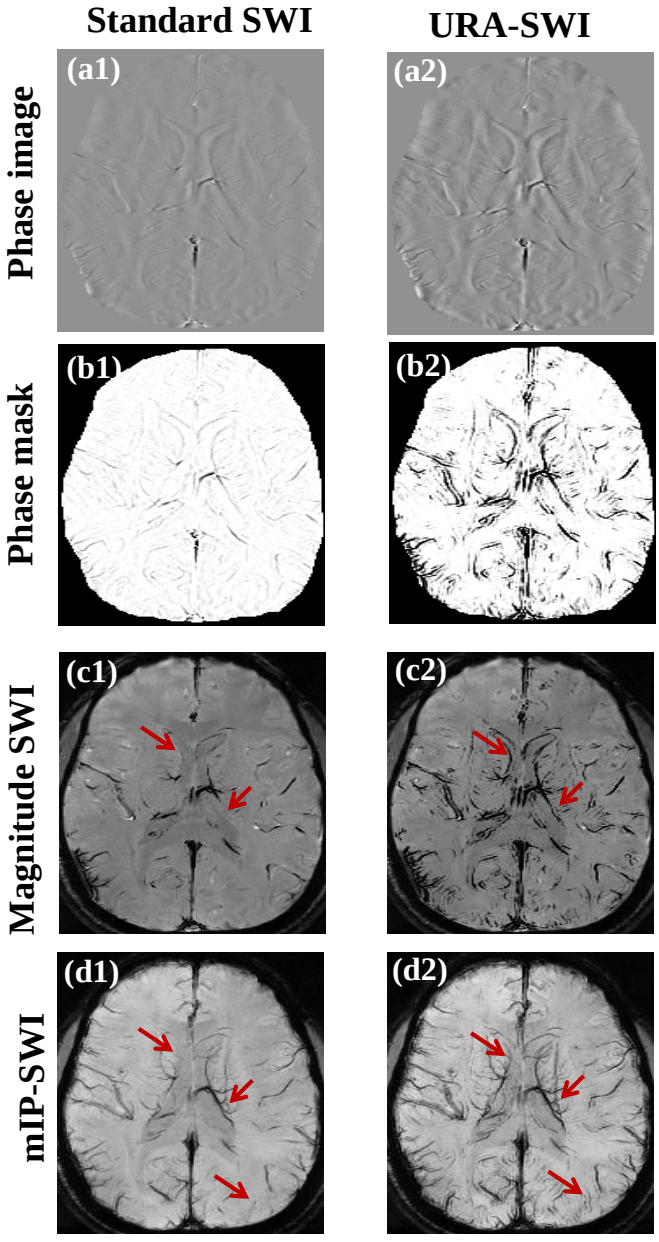

Fig. 4.15 Row-wise panels show the combined phase, phase mask, magnitude SWI and mIP images. Red arrows are used to indicate the newly observed venous structures in the reconstructed magnitude SWI.

A major advantage of phase reconstruction with URA prior in SWI processing is the restoration of obscured information in regions with residual components of bulk field

inhomogeneity and phase wraps. For example, in a brain slice with dural sinus where phase wraps and bulk field inhomogeneities are usually high, phase reconstruction with URA prior enhances the SuR information, and enables restoration of venous structures in the cerebral peduncle and choroid plexus as shown in Fig. 4.15 (red arrows). Due to the bulk field variations introduced by the interpeduncular cistern, these venous structures are usually not enhanced in standard SWI (Fig.4.15 (a)). Venous structures between the superior and middle temporal gyrus near to the sinus regions are also seen enhanced in the magnitude SWI generated using the phase processed with URA prior (red arrow).

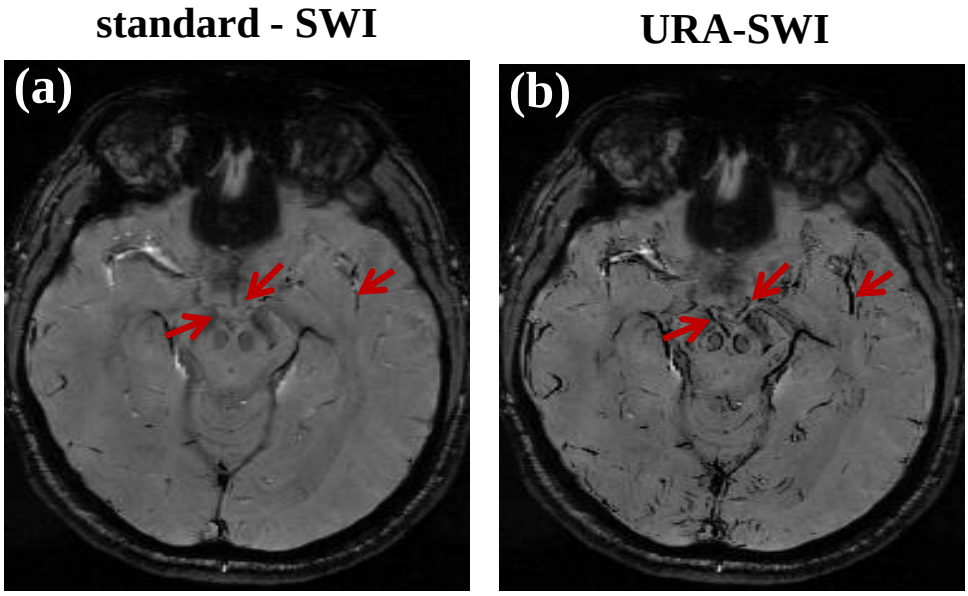

Fig. 4.16: Left and right panels show the magnitude SWI generated from the unprocessed phase image and phase image reconstructed with URA prior in a brain slice with dural sinus. Venous structures in the cerebral peduncle and choroid plexus (red arrows) which are obscured in standard SWI are restored in the magnitude SWI generated from the reconstructed phase image.

Contrast enhanced magnitude images are also compared with the susceptibility map weighted imaging (SMWI) and the standard SWI. In SMWI, susceptibility map based weighting provides an alternative SuR contrast to the magnitude images. Left-

to-right panels in Fig. 4.16 shows the reconstructed magnitude image, standard magnitude SWI, SMWI and URA-SWI using the data acquired from a healthy volunteer. For contrast enhancement in all three cases, the susceptibility mask is multiplied 4 times with the magnitude image. Among the three methods, standard SWI exhibits comparatively less contrast. Although GP appears more hypointense in SMWI, several fine structures are missing in SMWI. Red arrows indicate the subcortical and superficial medullary veins that are missed out in SMWI, and seen with good resolution in the SWI images generated using URA prior.

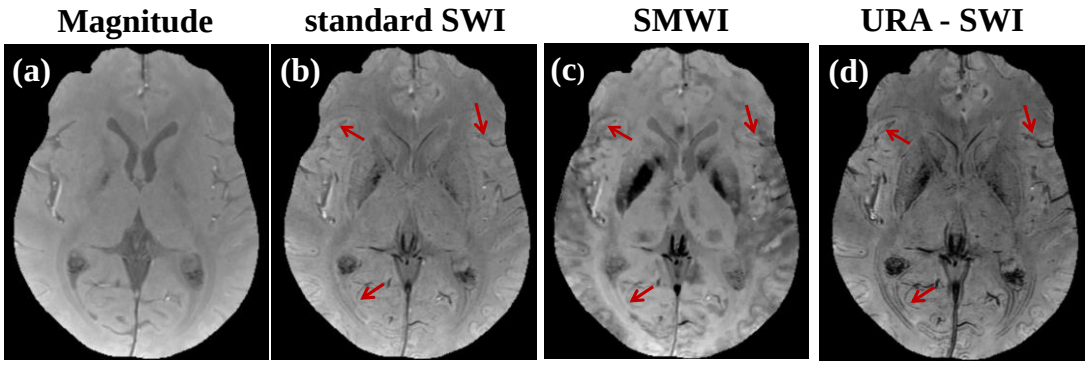

Fig.4.17: Contrast enhanced magnitude SWI generated using phase image reconstructed with URA prior is compared with standard SWI and SMWI. Left to right panels show the reconstructed magnitude image, standard SWI, SMWI and URA-SWI. Red arrows are used to indicate the sub cortical and superficial medullary veins that are missed out in standard SWI and SMWI.

CHAPTER 5
DISCUSSION

5.1 Granularity and high resolution SWI acquisition

The high spatial resolution GRE acquisition required in SWI results in reduced SNR. Thus denoising filters that reduces the noisy effect in the phase mask and simultaneously preserve the structural contrast is highly desirable in SWI processing. Reducing the granularities and preserving the structural information, using the same filter parameter make the proposed GRADER method suitable for SWI processing. Here the denoising method introduces enough smoothing to the image so that the effect of granularities is reduced and structural information in the phase is preserved. The main aim of all edge-preserving denoising filters is the preservation of structural information while denoising. A common way to perform this is by designing a cost function which has a fidelity term to maintain the consistency with the original data and a regularization term to introduce smoothness into the desired image. The desired image is obtained by minimizing the cost function. The regularization term is weighted by a free parameter λ. As the value of λ increases more smoothness will be introduced into the desired image and result in noise reduction at a cost of losing the structural information in the image. On the contrary, when the values of λ are small less amount of noise will be removed but it preserves all the structural information in the image. This indicates that there exist a trade-off between the amount of smoothness and preservation of structural information. Therefore a proper section of regularization parameter is necessary to preserve the structural information while denoising.

In this case, the granularities in the phase image needs to be controlled while enhancing the structural information in the phase image. This is achieved by introducing an additional parameter in the cost function which is automatically tuned according to the amount of noise present in the image. Since the fidelity and the regularization term shows an opposing behaviour with respect to the change in ts, the cost function will show a minimum for a particular value of the scale parameter. In practice it is observed that, the value of ts for which the cost is minimum when computed with input phase φ and a denoised phase $\widehat{\omega}^{(k)}$, will be less than the one computed with $\widehat{\omega}^{(k-1)}$. Using the AM technique the cost function is minimized for the ts and $\widehat{\omega}$ so that the high-pass filter is adaptively tuned. In this way the GRADER algorithm enhance the structural information without amplifying the granularities.

5.2 Effect of spatial high-pass filtering in SWI processing

The 3D GRE sequence used for SWI employs $T2^*$ decay which enhances the sensitivity to microscopic susceptibility differences. The filtered phase image exhibit phase values with different signs for the paramagnetic and diamagnetic substances. The phase polarity for iron deposition and calcification is inherently scanner dependent. In left handed systems like Siemens and Canon the paramagnetic components appears bright unlike the other (GE and Philips use a "right-handed) where the paramagnetic substance appears dark. Siemens Healthcare uses the SWI processing in resemblance to that described by Haacke (Haacke et al., 2004). A multi-echo proton density weighted post processing technique is used by GE. This technique is known as SWAN. A processing method called PADRE is used by Philips which works on phase difference-enhanced imaging technique. Here the

phase mask is created using a phase difference image and the polynomial fitting function. The CNR of the resultant SWI images is controlled by the degree of fitting. Here the filter parameter and the polynomial fitting term are adapted with the matrix size used for scanning to maintain the CNR of the image. As distinct from the post-processing capabilities of other scanners, Canon's flow-sensitive black blood (FSBB) sequence uses motion-probing gradients to generate additional signal dephasing in slow flowing vessels. This enables slow vessel contrast to develop at short TEs without sacrificing image quality.

When the SWI processing among different vendors are compared, PADRE shows a unique behaviour as the filter parameter and fittings are adjusted automatically to maintain the contrast as the resolution changes. The spatial WHP filter proposed in this thesis works similar to PADRE, as the neighborhood window size required for the WHP filter also changes with image resolution. The main difference observed between PADRE and WHP filter is that, in the former the contrast parameter is automatically chosen to maintain the contrast, but in WHP there is flexibility in choosing the contrast parameter. The addition of noise compensation enables usage of high value in contrast parameter. The WHP filter proposed here has three major additional features. The first feature of WHP is that spatial dependence of the filter using weights derived from the phase difference and the scale parameter. Here the window size for the spatial operation depends on the acquisition matrix. The second notable feature of WHP filter is the involvement of filter parameter to reduce the filter induced artifacts. The last is the addition of a new technique to reduce the effect of noise in the WHP filtering process.

The filter weight function serves to enhance the susceptibility-related change in phase across the vessel boundaries. As the value of t directly influences the means μ_w, μ_{C_1} and μ_{C_2}, it is possible to continuously tune the slope in order to adjust the proportion of false versus the actual venous structures. The weights are estimated using a scaled and shifted form of error function with an offset, whose slope is adjusted by varying the filter scale parameter. With this model, the filter strength can be varied by adjusting the slope. The process of decreasing the slope requires increasing the value of t, and accompanied by-: 1) an increase in μ_w and μ_{C_1}, and 2) more voxels with phase mask intensities in the range $[\mu_{C_1}, \mu_w]$ assuming values $> \mu_w$, thereby pushing the undesirable edges into the higher intensity region C_2. However, beyond a certain limit of increasing t, μ_w ceases to increase significantly. Since venous structures mostly assume low values in the phase mask, it is reasonable to argue that false venous structures are more likely represented by $\mathcal{W} > \mu_{C_1}$. As t is increased, more false structures assume intensities $\mathcal{W} > \mu_w$, and hence become part of C_2. This implies that the maximum number of voxels containing false edges has been flushed out to C_2, with only the faint venous structures remaining in the interval $[\mu_{C_1}, \mu_w]$. We obtain the greatest reduction of false edges in the mask, and retention of more venous structures, by choosing t at the point where μ_w is well separated from μ_{C_1}.

As the field strength increases, SWI signals show benefits in terms of it acquisition speed and SNR. This is due to the faster accumulation phase at higher field strength results in reduced TE and TR values. Separate experiments were performed to analyze the performance of spatial high-pass filter with noise compensation on

imaging resolution and SNR. Two sets of data were acquired at 1.5 T and 3.0 T with same in-plane resolution and slice thickness. It is seen that the t value corresponding to the maximum mean phase difference increases with SNR. Additionally WHPC filter introduces another step of increment to the value of t. The effect of scale parameter on field strength and SNR is shown in Fig.5.1. The effect of in-plane resolution is analyzed by examining the *VB-CNR* of images acquired at different resolution and same thickness. Mean phase difference is computed for the phase mask generated using WHP and WHPC filters. The in-plane resolution for two dataset scanned were 384×288 and 1024×832. Top and bottom row in Fig. 5.2 shows the magnitude SWI generated for low and high resolution data. It is observed that as the resolution increases the preferred window size for spatial operation also increases. The optimum window size for low and high resolution data is observed to be 3 and 7 respectively.

Dependence of N_r on filed strength is examined by computing the *VB-CNR* of the two dataset acquired at (a) 1.5 T and (b) 3.0 T by keeping the slice thickness ($2\ mm$) and image resolution (448×364) constant. Magnitude SWI generated for 1.5 T and 3.0 T data for different N_r is shown in Fig. 5.3. It is observed that, for both data the *VB-CNR* is maximum at the same $N_r = 3$. This indicates that the N_r depends only on image resolution and is independent of the field strength (448×364). Even though the applied spatial processing is same for both dataset acquired at 1.5 T and 3.0T, the mean *VB-CNR* of 3.0 T is 63.5% higher than the corresponding 1.5 T data.

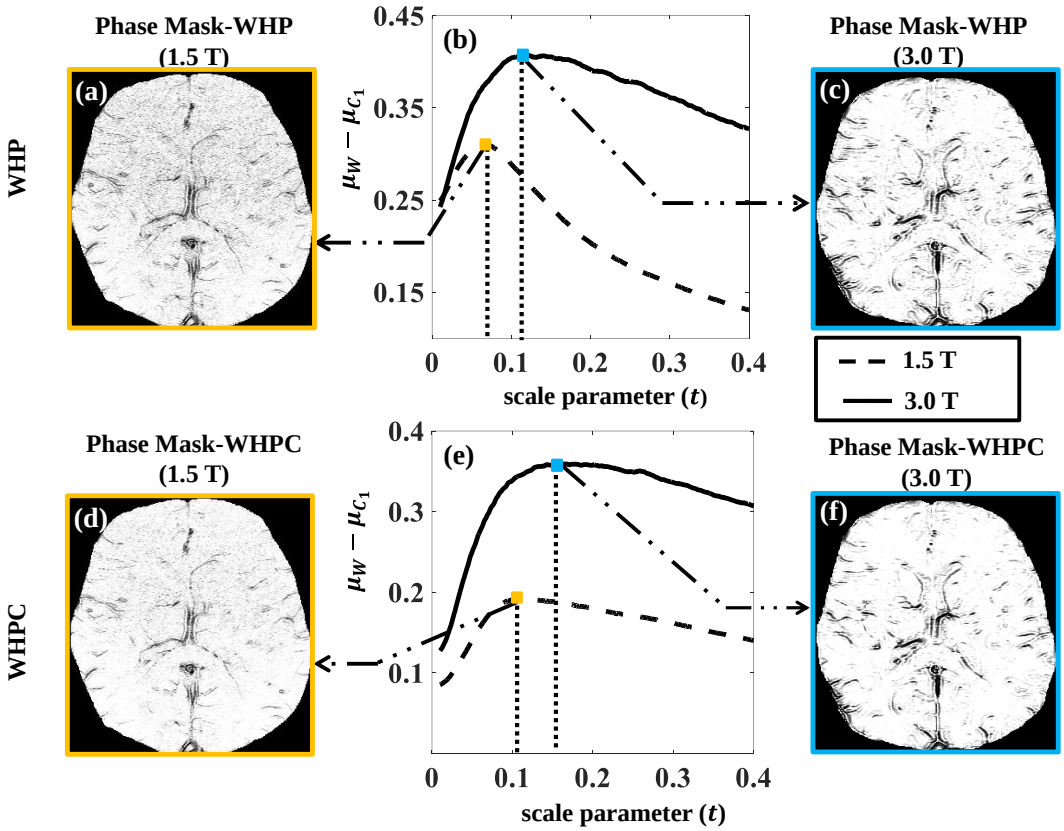

Fig. 5.1: Change in optimum scale parameter value with change in SNR.Since the high field strength data have more SNR than the lower one, both 1.5 T (dotted line) and 3.0 T (bold line) data were used in this study. Increase in scale parameter value is observed for 3.0 T data. Additional increase in scale parameter value is observed for WHPC filter due to noise compensation.

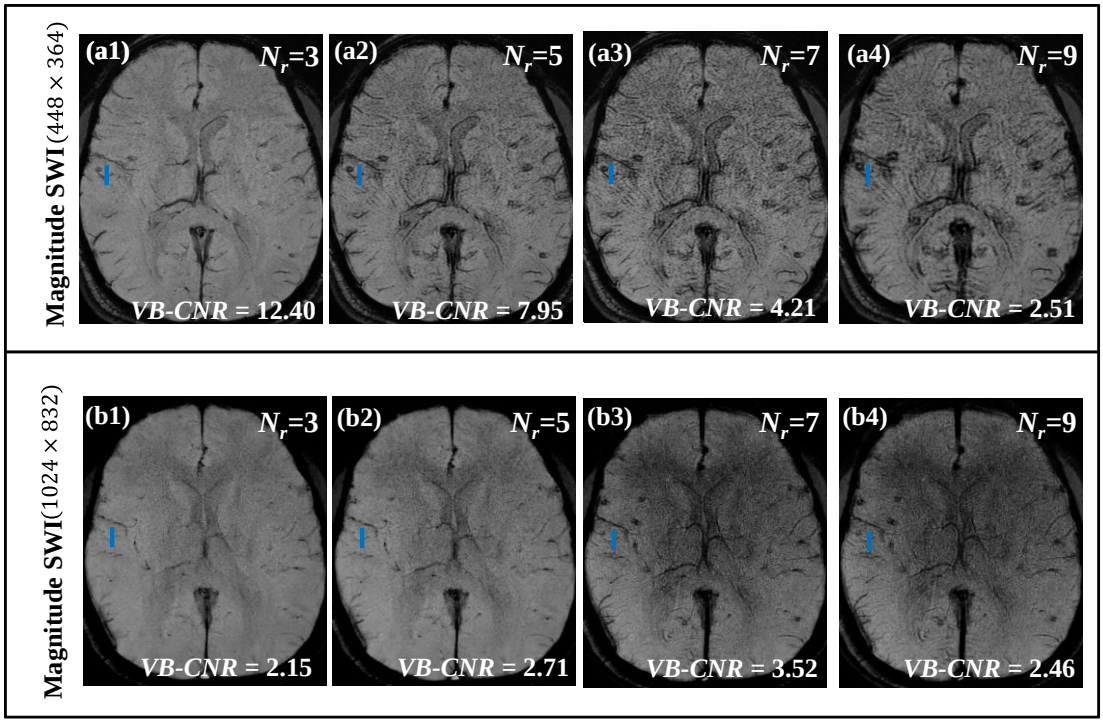

Fig.5.2: Magnitude SWI images of an volunteer scanned at 1.5 T for different resolution (a) 384×288 and (b) 1024×832 are shown in top and bottom panel. Left-right panel shows the SWI image with different neighbourhood size ($N_r = 3,5,7\ and\ 9$). ROI used to calculate the *VB-CNR* is indicated by blue line and the corresponding *VB-CNR* value is shown in insets.

One of the main advantage of noise compensation is the enhancement of CNR for a given contrast parameter. In standard SWI, contrast is increased by increase the number of phase masks multiplication. But beyond a limit CNR will decrease due to noise amplification. The optimal value of contrast parameter is the one for which the CNR is maximum. With a linear phase mask, contrast improvement in HHP filter is illustrated in Fig. 5.4.

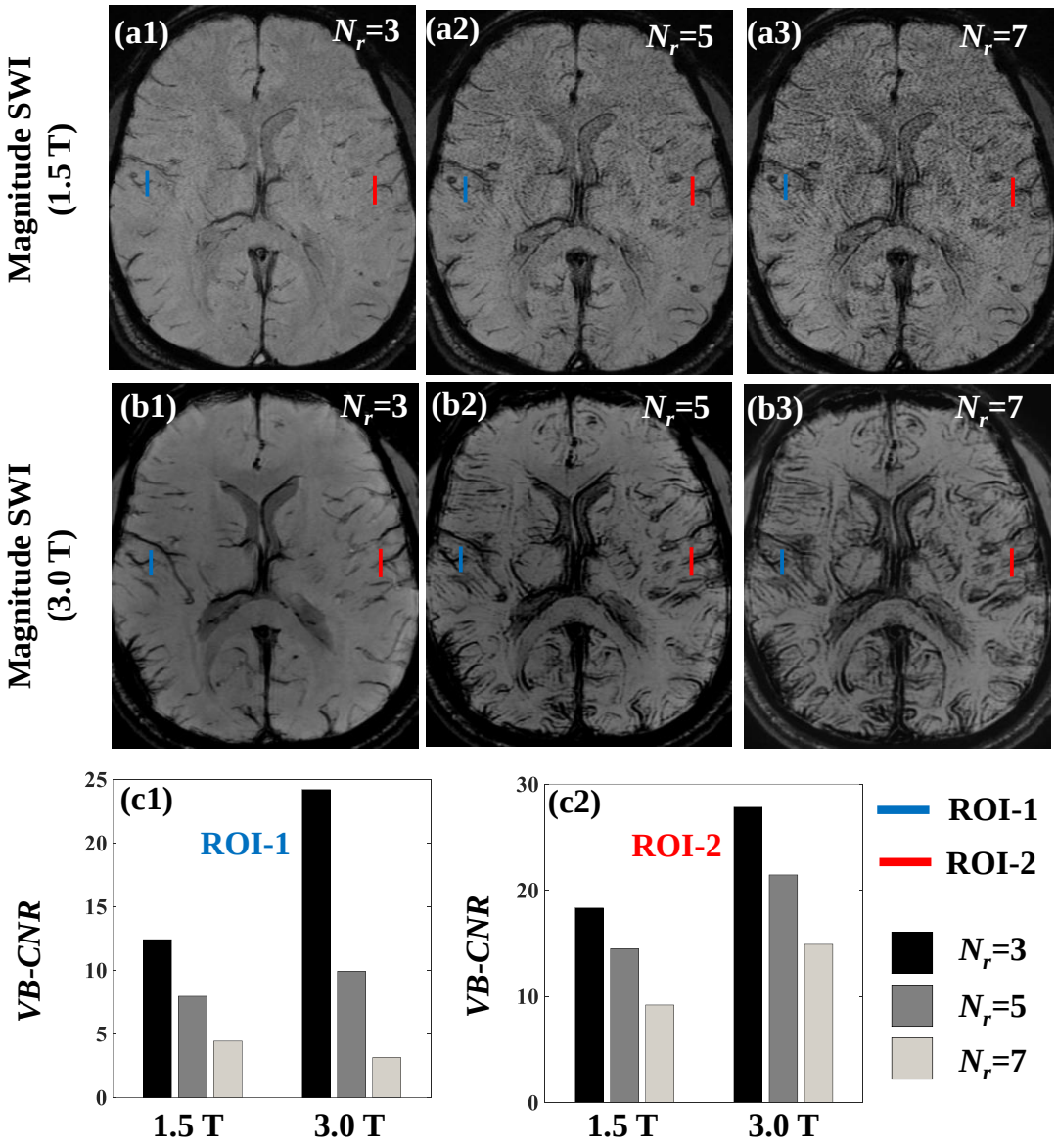

Fig.5.3: Top two rows show the magnitude SWI image generated at (a) 1. 5 T and (b) 3.0 T. In both these cases the slice thickness (2.0 mm) and in-plane resolutions (448×364) are kept constant. Left to right panel shows the magnitude SWI generated with different neighbourhood size. ROI-1 and ROI-2 used to compute the *VB-CNR* are indicated by blue and red lines. Bottom panel (c1) and (c2) shows the *VB-CNR* bar graphs at ROI-1 and ROI-2. In both the field strength magnitude SWI generated with $N_r = 3$ shows the highest *VB-CNR*.

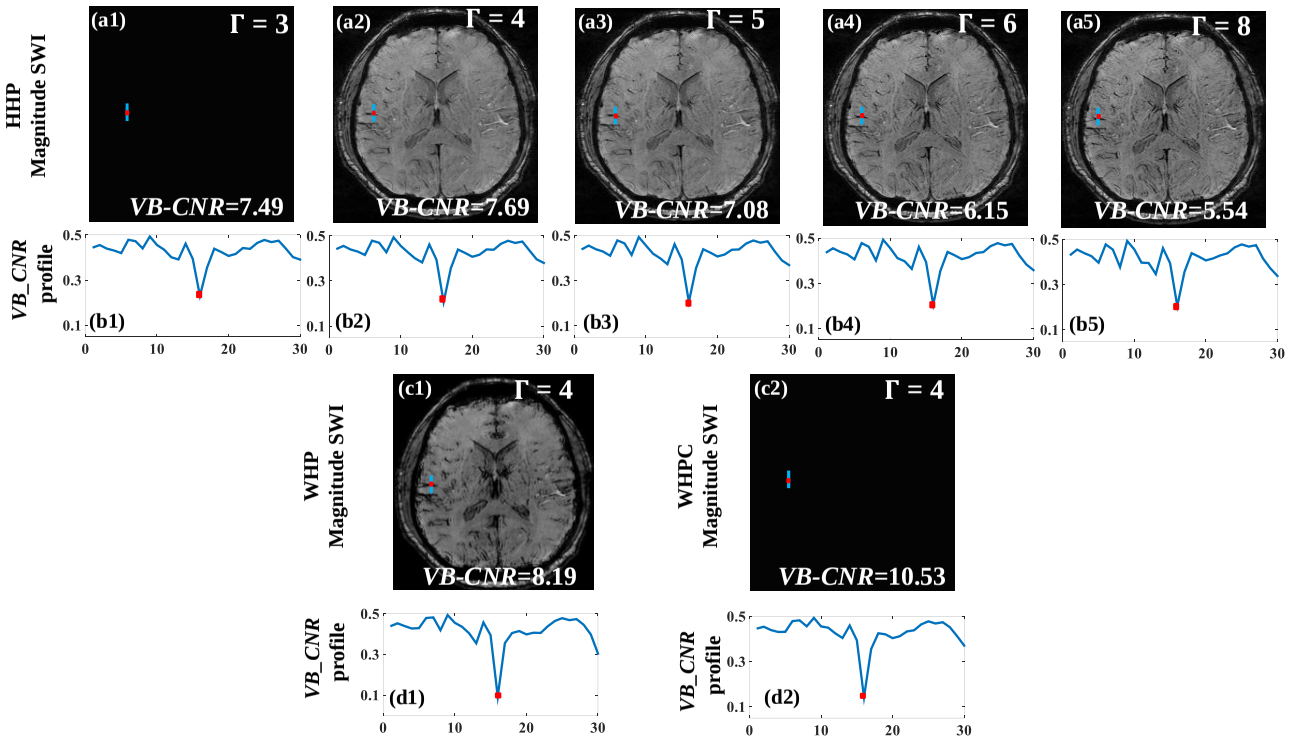

Fig.5.4: Effect of number of phase mask multiplication on *VB-CNR*. Column wise panel in the top row shows the magnitude SWI generated with increasing number (Γ) of phase mask multiplication. Panel (b1)-(b4) shows the *VB-CNR* profile at the ROI marked with blue line. It is observed that the *VB-CNR* reaches a maximum at an intermediate value of Γ=4. Magnitude SWI generated with WHP and WHPC are shown in panels (c1) and (c2).The *VB-CNR* profile for images in (c1) and (c2) are shown in (d1) and (d2).

Magnitude SWI image generated using HHP filter and different Γ value is shown in top row of Fig. 5.4. For each image *VB-CNR* is measured and shown in the insets. As the Γ value increases, the *VB-CNR* reaches a maximum and then start decreases due to the increase in effect of noise. The corresponding signal intensities at the ROI used for measuring the *VB-CNR* are shown in panels (b1)-(b4). It is observed that the *VB-CNR* is maximum for $\Gamma = 4$. Panels (c1) and (c2) show the magnitude SWI images associated with WHP and WHPC filters, respectively. For both the filter $\Gamma = 4$ is chosen for generating magnitude SWI. The *VB-CNR* profiles are shown in (d1) and (d2). The contrast improvement for WHP and WHPC filter as compared to HHP filter is 6.50% and 26.97% for $\Gamma = 4$. .

Another possible advantage of WHP filter is that, the acquisition parameter TE/TR can be shortened when compared to standard SWI. This is possible due to the increase in *VB-CNR* provided by the spatial high-pass filtering. To evaluate the contrast of SWI with change in TE/TR three sets of data with TE/TRs (a) $40/49$ ms, (b) $35/44$ ms and (c) 30/39 ms were acquired with same resolution and field strength. Magnitude SWI for the three dataset generated using HHP, WHP and WHPC filtering scheme is shown in Fig. 5.5. As expected, the *VB-CNR* value of SWI images obtained using WHP and WHPC filter is observed to be greater than the one acquired at longer TE/TR and processed with HHP filter. For illustration, when the TE is reduced by 12.5%, the *VB-CNR* of WHP and WHPC filter exhibit an improvement of 36% and 55% with all the structural information preserved when compared to the HHP filtered image at longer TE/TR. As the TE is shortened the *VB-CNR* of SWI image using HHP filter reduces by 7%. After shortening the TE by

more than 25%, the structural information loss is observed in SWI generated using WHP and WHPC filter, but it still exhibit a high *VB-CNR* for the retained structures.

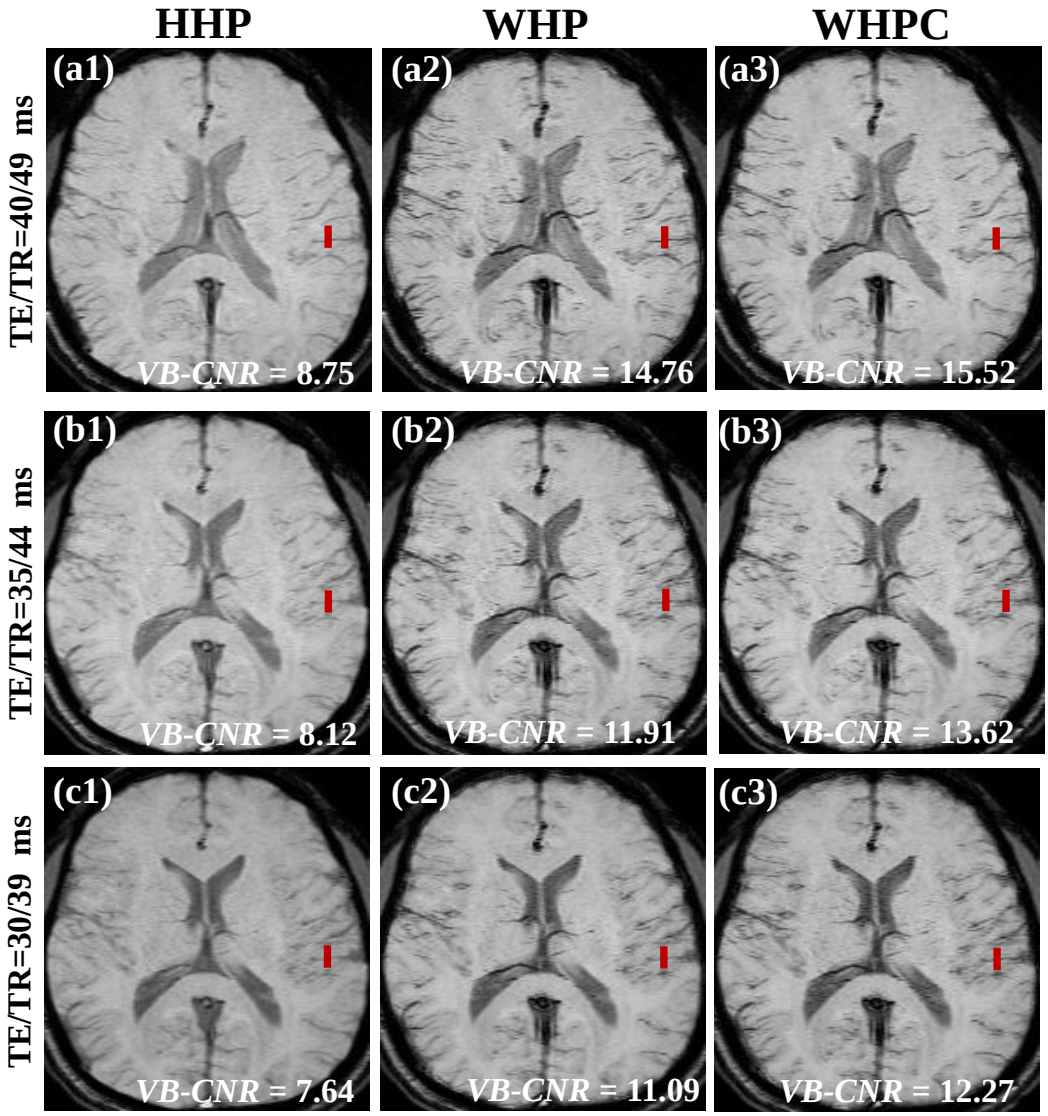

Fig.5.5: Magnitude SWI generated from 1.5 T SWI data acquired at three different TE/TR a) 40/49 ms, (b) 35/44 ms and (c) 30/39 ms is shown in the row-wise panels. Left –right panel corresponds to the filtering schemes HHP, WHP and WHPC filters. ROI used to measure the *VB-CNR* (shown in insets) is indicated by red line in each panel.

WHP and WHPC filter exhibits several benefits in clinical diagnosis, apart from the advantages discussed above. Easier identification of microbleed foci due to the increased blooming provided by WHPC is one among the major advantage of the

proposed filtering scheme. Even though there are certain disadvantages due to increased blooming, it is found to be useful in detecting the inhomogeneities due to various sources. For example, the main use of SWI sequence is to detect the presence of bleed and not to measure the exact size of the bleed. Therefore increased blooming is helpful to identify the bleed foci much easier. In the proposed filtering scheme (WHP and WHPC) blooming is controlled by the weighting function used to modulate the local phase difference. The other parameters that affect the blooming include TR, TE, image resolution, flip angle and main magnetic field strength.

In the case of mild cognitive impairment, WHP filter provided more hypo intense appearance of putamen structure indicative of the of iron depositions in these regions. In the standard SWI using HHP filter the hypo intense appearance is not evident. Moreover magnitude SWI generated after WHP filtering shows the basal ganglia structures more clearly than the standard SWI.

One of the main disadvantages of the proposed filtering scheme is the requirement for a training phase to estimate the optimum window size needed for the spatial operation. Moreover to perform noise compensation, phase unwrapping and background suppression need to be perform separately for each channel. This will increase the computation in acquisition with increased number of channel. In pMRI performance of noise compensation by estimating the noise from the region outside may not be accurate. The performance can be improved by an additional noise scan.

5.3 URA phase reconstruction algorithm on phase dispersion and SNR

In this study, a phase reconstruction scheme with URA prior was used for restoration of missing venous structures, especially in regions with high phase wraps and bulk

field variations. The incoherence in gradient refocusing due to presence of bulk field variations will lead to phase dispersion across voxels, resulting in magnitude intensity drop. With reference to the signal model in the temporal direction, the associated sinc function modulation makes the magnitude component unpredictable. Since the phase SNR is directly related to the magnitude signal intensity, the phase images have low SNR at locations where the signal intensity is low. This effect will be more severe in the regions with bulk field variations. Due to the imperfections in background suppression, phase dispersion is not completely eliminated from the phase image. The combined effect of reduced SNR and phase dispersion causes the voxel-wise signal model to deviate from the one consisting of a single complex exponential corresponding to the frequency relating to the susceptibility induced field. Thus by model fitting the unit magnitude complex exponential in the background suppressed phase image, it is possible to apply a unity rank approximation of the structured matrix along the temporal dimension.

The influence of phase reconstruction algorithm on phase dispersion and SNR is examined by a separate experiment. At each voxel, a singular value map of a non-principal singular value is first created from the structured Hankel matrix constructed from the unprocessed background suppressed phase. Here the second singular value is chosen from the Hankel matrix constructed using the complex exponential of the background suppressed phase for illustration. In the singular value map, those regions with values close to zero indicate voxels where the background suppression is more effective. Alternatively, it can also say that the magnitude signal intensity at this location maintains its predictability in the temporal dimension. On the contrary, increased magnitude of the singular value corresponds to regions where the

background suppression is less effective. The magnitude intensities at these locations deviate from the decaying exponential model. To validate the merit of the algorithm, the non-principal singular value map is generated once again after replacing the background suppressed phase with the reconstructed phase. The second map reveals reduced number of locations with higher singular value magnitudes as shown in Fig 5.6.

It is also seen that a large proportion of the high intensity voxels in the singular value map are seen in the brain boundary, and regions affected by bulk field inhomogeneities. For example, in a brain slice just above the dural sinus (first and second column), high singular values are seen in the Fornix and the frontal region including the superior and middle frontal gyrus. With reconstructed phase, numbers of high intensity pixels in these areas are considerably reduced. The third column shows the images of a slice with interpeduncular cistern. High values in singular value maps are seen in the region around cerebral peduncle which is further reduced with model fitting. For a deep brain slice (last column), most of the high intensity values are in the brain boundary, frontal and basal ganglia regions. From this it is clear that the effect of phase dispersion is high in regions with field inhomogeneity and model fitting the phase can substantially improve the quality of GRE phase images.

Fig. 5.7 compares the effect of applying SHARP, PDF and LBV to remove the bulk field inhomogeneities from the unwrapped phase. As expected, each method removes

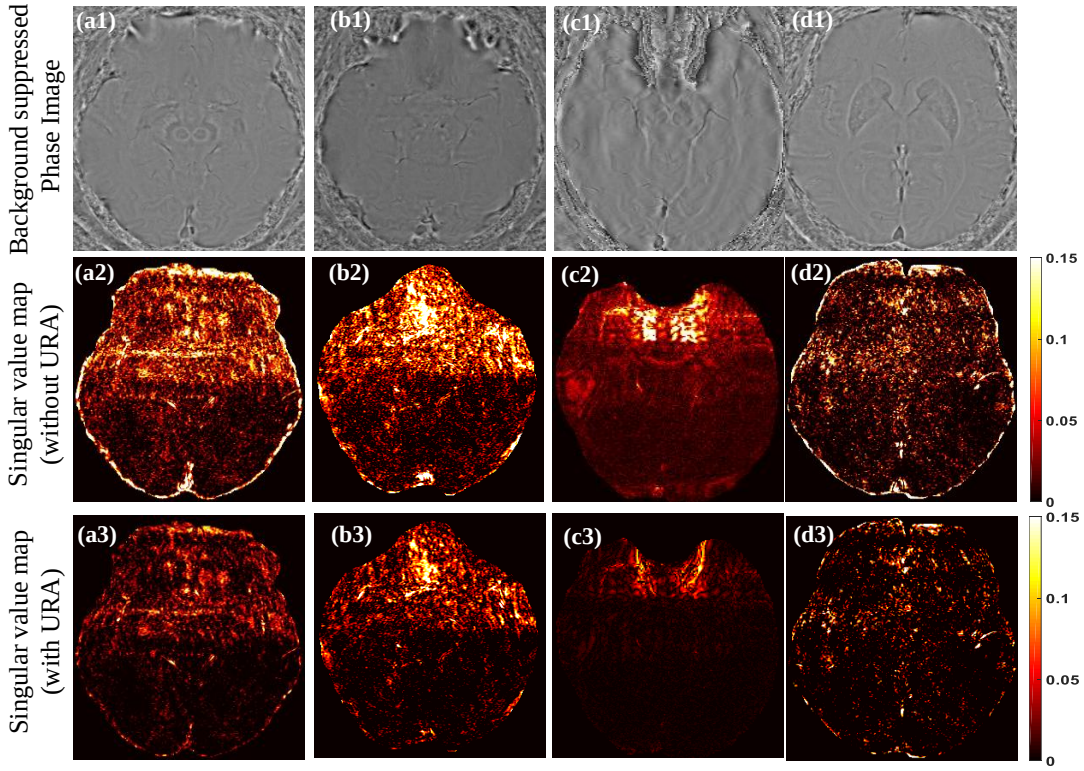

Fig.5.6: Background suppressed phase for different brain slices are shown inn first row. Second row shows the secondary singular value maps obtained from the Hankel matrix constructed from the complex exponential of the unprocessed phase. (Here, the complex exponential signal includes the magnitude information also, which is not same as the Hankel matrix constructed for phase reconstruction using URA prior. This is to evaluate the influence of URA priors in low SNR region). Similarly, third row shows the singular value map constructed from the phase image processed with URA priors. It is observed that the singular value maps obtained using phase image reconstructed with URA prior exhibit less number of high intensity pixels.

the bulk fields differently. The resultant singular value maps obtained from the unit magnitude complex exponential signal constructed using the unprocessed phase image after background suppression are shown in the first row of Fig. 5.7. White arrows are used to indicate the locations where singular value magnitudes change substantially with each method. An interesting observation is that the singular value maps obtained from the reconstructed phase image (bottom row), appears relatively same with no significant effect on the method used for background suppression.

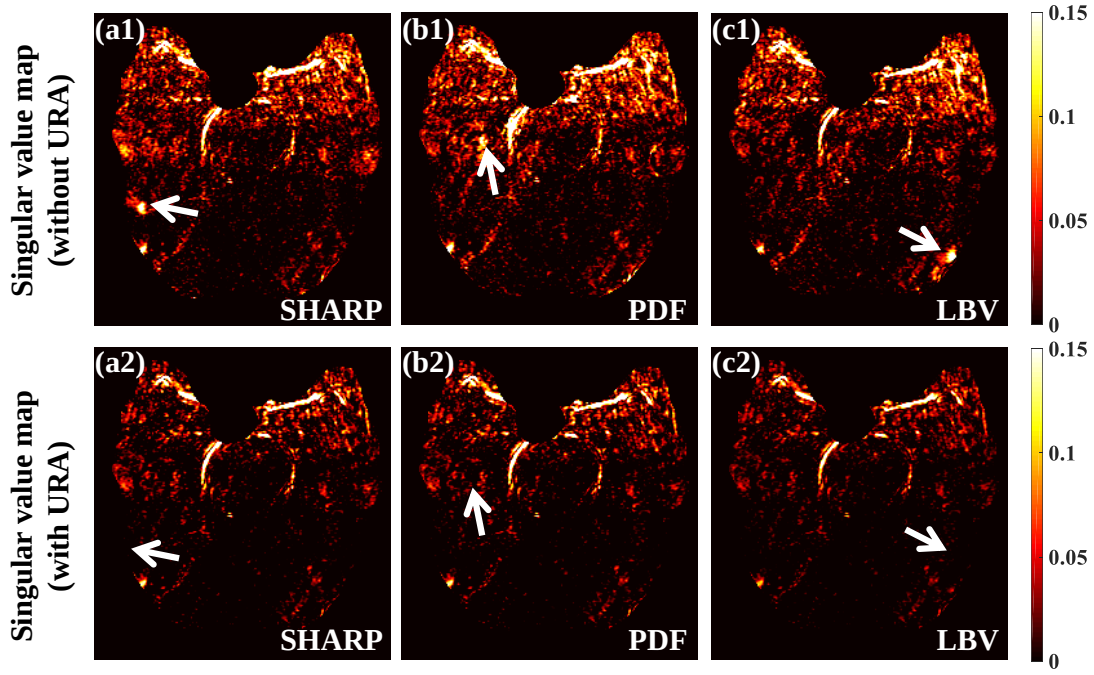

Fig.5.7: Effect of URA prior for phase reconstruction with different back ground suppression methods (a) SHARP, (b) PDF and (c) LBV. Row wise panels show the secondary singular value maps obtained using phase image processing without and with URA priors. (Singular value maps are constructed in the same way as discussed in the caption for Fig. 5.6). Arrow heads are used to indicate the positions where processing with URA prior reduces the magnitude of secondary singular value. Secondary singular value map obtained with URA priors appears relatively similar. This shows that the imperfection in background suppression is less affected in the reconstructed phase.

5.3.1 Empirical convergence

Fig. 5.8 shows empirical convergence of the phase reconstruction scheme for different values of λ. Bottom row (b-f) shows the combined reconstructed phase image obtained from each value of λ. It is observed that increase in value of λ leads to higher steady state errors. From numerical experiments, it is observed that λ in the range of (0.001-0.009) result in phase images with enhanced SuR information in slices with residual wraps and bulk field inhomogeneities.

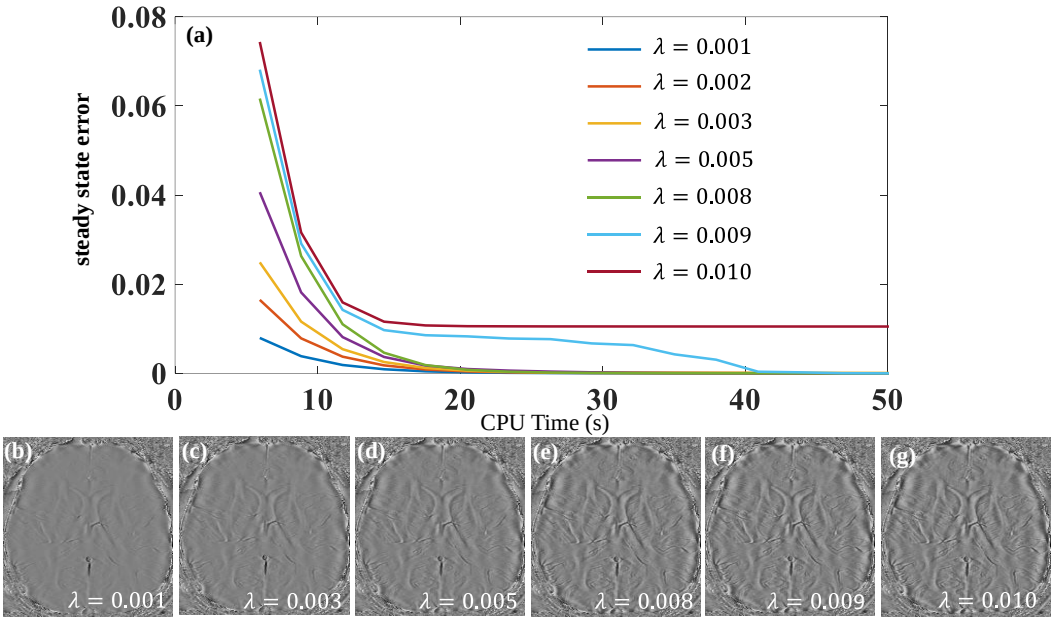

Fig.5.8: Convergence of the algorithm in terms of steady state error for different value of regularization parameter λ. Top panel shows the relative difference between phase images of two successive iterations with respect to CPU time. Panel (b-f) show the phase images obtained with different λ values.

It is observed that for a given choice of λ, RLNE plots for the reconstructed phase from lower echoes exhibit slower convergence as compared to those from higher echoes. Fig.5.9 (a) shows the empirical convergence for echoes acquired at TE values ranging from 5.7 ms to 29.3 ms, with an interval of 5.9 ms (five echoes). Irrespective of convergence rate, all echoes exhibit almost same steady state error. It is also observed that the steady state errors are low for a pre-determined range of λ, outside which the steady state errors increase exponentially, as shown in Fig. 5.9(b). According to (Candès et al., 2011), a preferred choice of λ depends directly on the dimension of the image. This is of the form $\lambda = \max(N_{row}, N_{col})^{-1/2}$, where N_{row} and N_{col} denote the number of rows and columns of the image. However, for a given application, the value of λ can be tailored by multiplying with a scale parameter $\varepsilon >$

0. The acceptable ranges of ε are observed to be (0.03-0.2) for all ten multi-echo data with three echoes and matrix size 384×202.

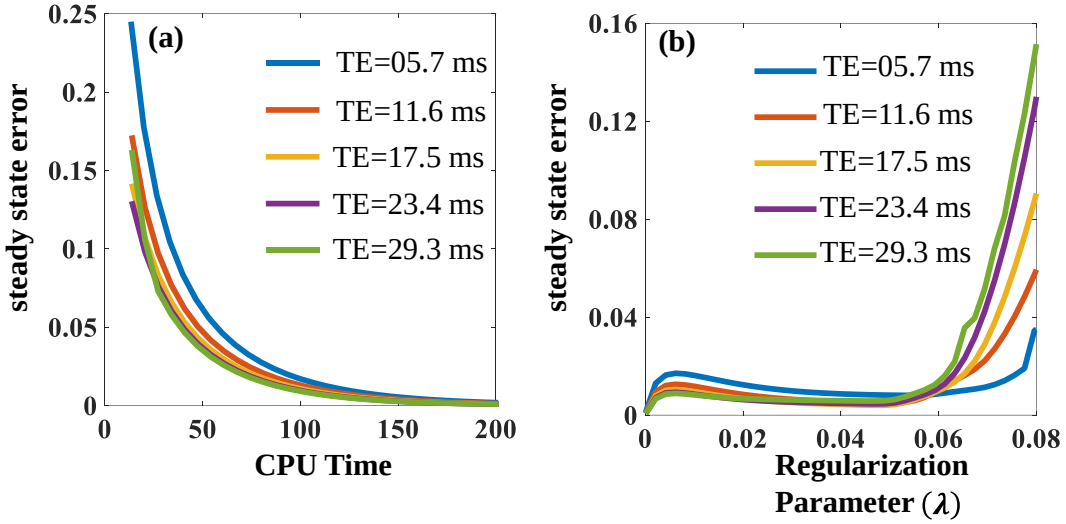

Fig. 5.9: (a) Empirical convergence of phase reconstruction algorithm for a multi-echo data with TE ranging from 5.7 ms to 29.3 ms with an interval of 5.9 ms. (b) Steady state error as a function of regularization parameter λ for five different echoes.

5.4 Future Work

It is foreseeable that the future of MR phase imaging is Quantitative Susceptibility Mapping (QSM) (de Rochefort et al., 2010, Schweser et al., 2011, Liu et al., 2011b), where the intensity variation have a definite physical meaning. In QSM the dipolar property of phase image is eliminated through an inversion and susceptibility maps are generated for quantification. QSM involves estimating the susceptibility map through dipole inversion of the measured phase data. For this, the measured phase data should be processed to remove the field inhomogeneity caused by the source outside the ROI. An inherent assumption is that, the background suppression methods impose a smoothness constraint on the measurement data, and thereby reduces the spatial resolution. To address this, a cohort of background suppression

methods has been proposed. Imperfections in the standard phase pre-processing are known to result in loss of spatial resolution and SuR information. Therefore, a major challenge in quantification of iron depositions is to recover the lost information in regions with high phase wraps and bulk field inhomogeneity. Although refinements in phase pre-processing have resulted in minimizing the signal errors, it is impossible to recover the lost information without introducing corrections in the signal model. Tweaking the signal model as shown in URA processing scheme will help to enables the visualization of obscured iron depositions that are not identified in standard QSM. This encourages investigating further and modifying the algorithm for QSM.

A second future application of the methods developed through this thesis is that it may improve the quality of QSM based oxymetry. After processing the phase as discussed in this thesis, the reconstructed images can be used for measuring the cerebral metabolic rate of oxygen and oxygen extraction fraction (OEF) map. Since susceptibility based oximetry is a suitable tool for studying the metabolic and degenerative disorders of the brain, knowledge of the metabolicrate of oxygen provides us with a direct measure of energy consumption. Another possible advantage of using the phase processing method in susceptibility based oximetry is the resultant high temporal resolution.

The URA-SWI processing algorithm can be integrated with the rapid acquisition schemes like compressed sensing / SPIRiT (Lustig et al., 2007, Lustig and Pauly, 2010) to develop a phase sensitive MR image reconstruction scheme. Since SPIRiT is an iterative algorithm, it comes with an exact match with the phase processing scheme discussed in this thesis. The inherent noise reduction in phase that can be

achieved by applying URA processing in the SPIRiT iteration loop will results in reduction of phase error relative to the standard SPIRiT. This will enable high-quality SWI/QSM images along with reduction in acquisition time.

CHAPTER 6

SUMMARY AND CONCLUSION

Phase images in MRI provide susceptibility related information about tissues that can be used to enhance the contrast of magnitude images. Clinical application of MRI phase is made possible by the development of magnetic field technology to provide homogeneous static magnetic field and advances in post processing technique which removes the non-local field variations. While enabling improved contrast and wide clinical applications for techniques like SWI, presence of artifacts and noise in phase provides opportunity for further investigating the possibilities to improve the quality. In this thesis, different aspects of SWI and MRI phase image were investigated and presented three novel post processing schemes for improving the quality of SWI.

The limitations of the standard SWI processing are addressed through three objectives. The granularity in the SWI image, when the SuR contrast is increased by the multiplication of the susceptibility mask caused a reduction in CNR of magnitude SWI. This is addressed by an edge preserved denoising method called GRADER. One main advantage of GRADER and its extension to IR-GRADER is that, granularities in the magnitude SWI is controlled by preserving the structural information in phase. In vivo experiments using multi-channel SWI data have illustrated the application of GRADER and IR-GRADER algorithms to enhance the SuR information of the phase and the processed SWI magnitude. The convergence of filter parameter to a steady state value shows the reliability of the high-pass filter.

The new spatial high-pass filtering scheme for SWI as proposed in this thesis enhances the SuR contrast by weighting the phase differences along each clique to

enhance the local SuR phase information at different scales of emphasis. The filter induced artifacts are removed using the filter parameter that is modulated according to the statistics of the phase mask. Inclusion of noise compensation weights estimated using prior information about the signal intensity and the noise variance employs further improvement in the CNR. The superiority of spatial high-pass filter with noise compensation, in respect of deducing more accurate clinical information is demonstrated for neurological conditions of stroke, tumor, microbleed and mild cognitive impairment.

As a third contribution of this thesis a processing scheme for GRE phase to enable restoration of SuR features in regions affected by imperfect background suppression and low SNR due to phase dispersion was developed. This work proposes incorporation of URA processing with data fidelity into the SWI pipeline for phase reconstruction to enable restoration of missing venous structures and susceptibility information. Using in vivo data, it is illustrated that this phase reconstruction method enables restoration of venous structures in cerebral peduncle and temporal gyrus that are obscured in magnitude SWI generated with the state-of-the-art methods.

BIBLIOGRAPHY

Abdi, H., Lewis-Beck, M., Bryman, A. & Futing, T. 2003. Encyclopedia for research methods for the social sciences. *by M. Lewis-Beck, A. Bryman, and T. Futing, Sage, Thousand Oaks, CA*, 792.

Abduljalil, A. M., Schmalbrock, P., Novak, V. & Chakeres, D. W. 2003. Enhanced gray and white matter contrast of phase susceptibility-weighted images in ultra-high-field magnetic resonance imaging. *Journal of Magnetic Resonance Imaging: An Official Journal of the International Society for Magnetic Resonance in Medicine,* 18**,** 284-290.

Abragam, A. & Abragam, A. 1961. *The principles of nuclear magnetism*, Oxford university press.

Aja-Fernández, S. & Tristán-Vega, A. 2013. A review on statistical noise models for magnetic resonance imaging. *LPI, ETSI Telecomunicacion, Universidad de Valladolid, Spain, Tech. Rep*.

Andrews, T., Lancaster, J. L., Dodd, S. J., Contreras-Sesvold, C. & Fox, P. T. 2005. Testing the three-pool white matter model adapted for use with T2 relaxometry. *Magnetic Resonance in Medicine: An Official Journal of the International Society for Magnetic Resonance in Medicine,* 54**,** 449-454.

Babikian, T., Freier, M. C., Tong, K. A., Nickerson, J. P., Wall, C. J., Holshouser, B. A., Burley, T., Riggs, M. L. & Ashwal, S. 2005. Susceptibility weighted imaging: neuropsychologic outcome and pediatric head injury. *Pediatric neurology,* 33**,** 184-194.

Bagher-Ebadian, H., Jiang, Q. & Ewing, J. R. 2008. A modified Fourier-based phase unwrapping algorithm with an application to MRI venography. *Journal of Magnetic Resonance Imaging: An Official Journal of the International Society for Magnetic Resonance in Medicine,* 27**,** 649-652.

Bagley, L. J., Grossman, R. I., Judy, K. D., Curtis, M., Loevner, L. A., Polansky, M. & Detre, J. 1997. Gliomas: correlation of magnetic susceptibility artifact with histologic grade. *Radiology,* 202**,** 511-516.

Barbosa, J. H. O., Santos, A. C. & Salmon, C. E. G. 2015. Susceptibility weighted imaging: differentiating between calcification and hemosiderin. *Radiologia brasileira,* 48**,** 93-100.

Baudrexel, S., Volz, S., Preibisch, C., Klein, J. C., Steinmetz, H., Hilker, R. & Deichmann, R. 2009. Rapid single-scan T-mapping using exponential excitation pulses and image-based correction for linear background gradients. *Magnetic Resonance in Medicine: An Official Journal of the International Society for Magnetic Resonance in Medicine,* 62**,** 263-268.

Beylkin, G. & Monzón, L. 2005. On approximation of functions by exponential sums. *Applied and Computational Harmonic Analysis,* 19**,** 17-48.

Borrelli, P., Palma, G., Tedeschi, E., Cocozza, S., Comerci, M., Alfano, B., Haacke, E. M. & Salvatore, M. 2015. Improving signal-to-noise ratio in susceptibility weighted imaging: a novel multicomponent non-local approach. *PloS one,* 10**,** e0126835.

Bottomley, P. A., Foster, T. H., Argersinger, R. E. & Pfeifer, L. M. 1984. A review of normal tissue hydrogen NMR relaxation times and relaxation mechanisms from 1–100 MHz: dependence on tissue type, NMR frequency, temperature, species, excision, and age. *Medical physics,* 11**,** 425-448.

Boxerman, J. L., Bandettini, P. A., Kwong, K. K., Baker, J. R., Davis, T. L., Rosen, B. R. & Weisskoff, R. M. 1995. The intravascular contribution to fMRI signal change: Monte Carlo modeling and diffusion-weighted studies in vivo. *Magnetic resonance in medicine,* 34**,** 4-10.

Boyd, S., Parikh, N., Chu, E., Peleato, B. & Eckstein, J. 2011. Distributed optimization and statistical learning via the alternating direction method of multipliers. *Foundations and Trends® in Machine learning,* 3**,** 1-122.

Brainovich, V., Sabatini, U. & Hagberg, G. E. 2009. Advantages of using multiple-echo image combination and asymmetric triangular phase masking in magnetic resonance venography at 3 T. *Magnetic resonance imaging,* 27**,** 23-37.

Brown, R. W., Cheng, Y.-C. N., Haacke, E. M., Thompson, M. R. & Venkatesan, R. 2014. *Magnetic resonance imaging: physical principles and sequence design*, John Wiley & Sons.

Bydder, M., Larkman, D. J. & Hajnal, J. V. 2002. Combination of signals from array coils using image-based estimation of coil sensitivity profiles. *Magnetic Resonance in Medicine: An Official Journal of the International Society for Magnetic Resonance in Medicine,* 47**,** 539-548.

Cadzow, J. A. 1988. Signal enhancement-a composite property mapping algorithm. *IEEE Transactions on Acoustics, Speech, and Signal Processing,* 36**,** 49-62.

Candès, E. J., Li, X., Ma, Y. & Wright, J. 2011. Robust principal component analysis? *Journal of the ACM (JACM),* 58**,** 11.

Casciaro, S., Bianco, R., Franchini, R., Casciaro, E. & Conversano, F. 2010. A new automatic phase mask filter for high-resolution brain venography at 3 T: theoretical background and experimental validation. *Magnetic resonance imaging,* 28**,** 511-519.

Charbonnier, P., Blanc-Féraud, L., Aubert, G. & Barlaud, M. 1997. Deterministic edge-preserving regularization in computed imaging. *IEEE Transactions on image processing,* 6**,** 298-311.

Chua, A. C. & Morgan, E. H. 1996. Effects of iron deficiency and iron overload on manganese uptake and deposition in the brain and other organs of the rat. *Biological trace element research,* 55**,** 39-54.

Chung, A. C., Noble, J. A. & Summers, P. 2002. Fusing speed and phase information for vascular segmentation of phase contrast MR angiograms. *Medical Image Analysis,* 6**,** 109-128.

Dagher, J., Reese, T. & Bilgin, A. 2014. High-resolution, large dynamic range field map estimation. *Magnetic resonance in medicine,* 71**,** 105-117.

de Rochefort, L., Liu, T., Kressler, B., Liu, J., Spincemaille, P., Lebon, V., Wu, J. & Wang, Y. 2010. Quantitative susceptibility map reconstruction from MR phase data using bayesian regularization: validation and application to brain imaging. *Magnetic resonance in medicine,* 63**,** 194-206.

Deistung, A., Dittrich, E., Sedlacik, J., Rauscher, A. & Reichenbach, J. R. 2009. ToF-SWI: simultaneous time of flight and fully flow compensated susceptibility weighted imaging. *Journal of Magnetic Resonance Imaging: An Official Journal of the International Society for Magnetic Resonance in Medicine,* 29**,** 1478-1484.

Deistung, A., Rauscher, A., Sedlacik, J., Witoszynskyj, S. & Reichenbach, J. 2005. Optimization of data processing in susceptibility-weighted imaging. *Biomed Tech,* 50**,** 1168-1169.

Denk, C. & Rauscher, A. 2010. Susceptibility weighted imaging with multiple echoes. *Journal of Magnetic Resonance Imaging,* 31**,** 185-191.

Duyn, J. H., van Gelderen, P., Li, T.-Q., de Zwart, J. A., Koretsky, A. P. & Fukunaga, M. 2007. High-field MRI of brain cortical substructure based on signal phase. *Proceedings of the National Academy of Sciences,* 104**,** 11796-11801.

Edelstein, W. A. & Bottomley, P. A. 1984. Method of NMR imaging which overcomes T2* effects in an inhomogeneous static magnetic field. Google Patents.

FanJQ, G. 1996. LocalPolynomialModelingandItsApplications. *London: Chapmanand*.

Fernandez-Seara, M. & Wehrli, F. 2000. Postprocessing technique to correct for background gradients in image-based R* 2 measurements. *Magnetic Resonance in Medicine: An Official Journal of the International Society for Magnetic Resonance in Medicine,* 44**,** 358-366.

Frahm, J., Merboldt, K. D. & Hänicke, W. 1988. Direct FLASH MR imaging of magnetic field inhomogeneities by gradient compensation. *Magnetic resonance in medicine,* 6**,** 474-480.

Funai, A. K., Fessler, J. A., Yeo, D. T., Olafsson, V. T. & Noll, D. C. 2008. Regularized field map estimation in MRI. *IEEE transactions on medical imaging,* 27**,** 1484-1494.

Gabay, D. & Mercier, B. 1975. *A dual algorithm for the solution of non linear variational problems via finite element approximation*, Institut de recherche d'informatique et d'automatique.

Ghiglia, D. C. & Romero, L. A. 1994. Robust two-dimensional weighted and unweighted phase unwrapping that uses fast transforms and iterative methods. *JOSA A,* 11**,** 107-117.

Gho, S. M., Liu, C., Li, W., Jang, U., Kim, E. Y., Hwang, D. & Kim, D. H. 2014. Susceptibility map-weighted imaging (SMWI) for neuroimaging. *Magnetic resonance in medicine,* 72**,** 337-346.

Gillard, J. 2010. Cadzow's basic algorithm, alternating projections and singular spectrum analysis. *Statistics and its interface,* 3**,** 335-343.

Glover, G. H. 1999. 3D z-shim method for reduction of susceptibility effects in BOLD fMRI. *Magnetic Resonance in Medicine: An Official Journal of the International Society for Magnetic Resonance in Medicine,* 42**,** 290-299.

Goldstein, R. M., Zebker, H. A. & Werner, C. L. 1988. Satellite radar interferometry: Two-dimensional phase unwrapping. *Radio science,* 23**,** 713-720.

Golyandina, N., Nekrutkin, V. & Zhigljavsky, A. A. 2001. *Analysis of time series structure: SSA and related techniques*, Chapman and Hall/CRC.

Griswold, M. A., Jakob, P. M., Heidemann, R. M., Nittka, M., Jellus, V., Wang, J., Kiefer, B. & Haase, A. 2002. Generalized autocalibrating partially parallel acquisitions (GRAPPA). *Magnetic Resonance in Medicine: An Official Journal of the International Society for Magnetic Resonance in Medicine,* 47**,** 1202-1210.

Haacke, E., Tang, J., Neelavalli, J. & Cheng, Y. 2010a. Susceptibility mapping as a means to visualize veins and quantify oxygen saturation. *Journal of Magnetic Resonance Imaging,* 32**,** 663-676.

Haacke, E. M., Ayaz, M., Khan, A., Manova, E. S., Krishnamurthy, B., Gollapalli, L., Ciulla, C., Kim, I., Petersen, F. & Kirsch, W. 2007. Establishing a baseline phase behavior in magnetic resonance imaging to determine normal vs. abnormal iron content in the brain. *Journal of Magnetic Resonance Imaging: An Official Journal of the International Society for Magnetic Resonance in Medicine,* 26**,** 256-264.

Haacke, E. M., Brown, R. W., Thompson, M. R. & Venkatesan, R. 1999. *Magnetic resonance imaging: physical principles and sequence design*, Wiley-Liss New York:.

Haacke, E. M., Cheng, N. Y., House, M. J., Liu, Q., Neelavalli, J., Ogg, R. J., Khan, A., Ayaz, M., Kirsch, W. & Obenaus, A. 2005. Imaging iron stores in the brain using magnetic resonance imaging. *Magnetic resonance imaging,* 23**,** 1-25.

Haacke, E. M., Lai, S., Yablonskiy, D. A. & Lin, W. 1995. In vivo validation of the BOLD mechanism: a review of signal changes in gradient echo functional MRI in the presence of flow. *International Journal of Imaging Systems and Technology,* 6**,** 153-163.

Haacke, E. M., Liu, S., Buch, S., Zheng, W., Wu, D. & Ye, Y. 2015. Quantitative susceptibility mapping: current status and future directions. *Magnetic resonance imaging,* 33**,** 1-25.

Haacke, E. M., Miao, Y., Liu, M., Habib, C. A., Katkuri, Y., Liu, T., Yang, Z., Lang, Z., Hu, J. & Wu, J. 2010b. Correlation of putative iron content as represented by changes in R2* and phase with age in deep gray matter of healthy adults. *Journal of Magnetic Resonance Imaging,* 32**,** 561-576.

Haacke, E. M., Mittal, S., Wu, Z., Neelavalli, J. & Cheng, Y.-C. 2009. Susceptibility-weighted imaging: technical aspects and clinical applications, part 1. *American Journal of Neuroradiology,* 30**,** 19-30.

Haacke, E. M. & Reichenbach, J. R. 2014. *Susceptibility weighted imaging in MRI: basic concepts and clinical applications*, John Wiley & Sons.

Haacke, E. M., Xu, Y., Cheng, Y. C. N. & Reichenbach, J. R. 2004. Susceptibility weighted imaging (SWI). *Magnetic Resonance in Medicine: An Official Journal of the International Society for Magnetic Resonance in Medicine,* 52**,** 612-618.

Hammond, K. E., Lupo, J. M., Xu, D., Metcalf, M., Kelley, D. A., Pelletier, D., Chang, S. M., Mukherjee, P., Vigneron, D. B. & Nelson, S. J. 2008. Development of a robust method for generating 7.0 T multichannel phase images of the brain with application to normal volunteers and patients with neurological diseases. *Neuroimage,* 39**,** 1682-1692.

Helms, G. & Dechent, P. 2009. Increased SNR and reduced distortions by averaging multiple gradient echo signals in 3D FLASH imaging of the human brain at 3T. *Journal of Magnetic Resonance Imaging: An Official Journal of the International Society for Magnetic Resonance in Medicine,* 29**,** 198-204.

Hernando, D., Vigen, K. K., Shimakawa, A. & Reeder, S. B. 2012. R mapping in the presence of macroscopic B0 field variations. *Magnetic resonance in medicine,* 68**,** 830-840.

Hinshaw, W. S. & Lent, A. H. 1983. An introduction to NMR imaging: From the Bloch equation to the imaging equation. *Proceedings of the IEEE,* 71**,** 338-350.

Hoult, D. & Chen, C. 1989. Biomedical magnetic resonance technology. *Bristol and New York: IOP Publishing***,** 168-70.

Hwang, D. & Du, Y. P. 2009. Improved myelin water quantification using spatially regularized non-negative least squares algorithm. *Journal of Magnetic Resonance Imaging: An Official Journal of the International Society for Magnetic Resonance in Medicine,* 30**,** 203-208.

Iordache, M.-D., Bioucas-Dias, J. M. & Plaza, A. 2013. Collaborative sparse regression for hyperspectral unmixing. *IEEE Transactions on geoscience and remote sensing,* 52**,** 341-354.

Jang, U. & Hwang, D. 2011. High-Quality Venography from Multi-echo MR Dataset using T2* Relaxation Model.

Jang, U. & Hwang, D. 2012. High-quality multiple T2 (*) contrast MR images from low-quality multi-echo images using temporal-domain denoising methods. *Medical physics,* 39**,** 468-474.

Jang, U., Nam, Y., Kim, D.-H. & Hwang, D. 2013. Improvement of the SNR and resolution of susceptibility-weighted venography by model-based multi-echo denoising. *Neuroimage,* 70**,** 308-316.

Jenkinson, M. 2003. Fast, automated, N-dimensional phase-unwrapping algorithm. *Magnetic Resonance in Medicine: An Official Journal of the International Society for Magnetic Resonance in Medicine,* 49**,** 193-197.

Jin, Z., Xia, L. & Du, Y. P. 2008. Reduction of artifacts in susceptibility-weighted MR venography of the brain. *Journal of Magnetic Resonance Imaging: An Official Journal of the International Society for Magnetic Resonance in Medicine,* 28**,** 327-333.

Kumar, A., Welti, D. & Ernst, R. R. 1975. NMR Fourier zeugmatography. *Journal of Magnetic Resonance (1969),* 18**,** 69-83.

Lancaster, J. L., Andrews, T., Hardies, L. J., Dodd, S. & Fox, P. T. 2003. Three-pool model of white matter. *Journal of Magnetic Resonance Imaging: An Official Journal of the International Society for Magnetic Resonance in Medicine,* 17**,** 1-10.

Langkammer, C., Krebs, N., Goessler, W., Scheurer, E., Yen, K., Fazekas, F. & Ropele, S. 2012. Susceptibility induced gray–white matter MRI contrast in the human brain. *Neuroimage,* 59**,** 1413-1419.

Larsen, J. P., Britt III, W., Kido, D., Olson, B. L. B., Holshouser, B. A. & Kirsch, W. M. 2007. Susceptibility-Weighted Magnetic Resonance imaging in the evaluation of dementia. *Radiology Case Reports,* 2**,** 102.

Lee, B. C., Vo, K. D., Kido, D. K., Mukherjee, P., Reichenbach, J., Lin, W., Yoon, M. S. & Haacke, M. 1999. MR high-resolution blood oxygenation level–dependent venography of occult (low-flow) vascular lesions. *American Journal of Neuroradiology,* 20**,** 1239-1242.

Li, N., Wang, W. T., Pham, D. L. & Butman, J. A. 2015. Artifactual microhemorrhage generated by susceptibility weighted image processing. *Journal of Magnetic Resonance Imaging,* 41**,** 1695-1700.

Li, N., Wang, W. T., Sati, P., Pham, D. L. & Butman, J. A. 2014a. Quantitative assessment of susceptibility-weighted imaging processing methods. *Journal of Magnetic Resonance Imaging,* 40**,** 1463-1473.

Li, W., Avram, A. V., Wu, B., Xiao, X. & Liu, C. 2014b. Integrated Laplacian-based phase unwrapping and background phase removal for quantitative susceptibility mapping. *NMR in Biomedicine,* 27**,** 219-227.

Liang, Z.-P. & Lauterbur, P. C. 2000. *Principles of magnetic resonance imaging: a signal processing perspective*, SPIE Optical Engineering Press.

Lin, W., Mukherjee, P., An, H., Yu, Y., Wang, Y., Vo, K., Lee, B., Kido, D. & Haacke, E. 1999. Improving high-resolution MR bold venographic imaging using a T1 reducing contrast agent. *Journal of Magnetic Resonance Imaging: An Official Journal of the International Society for Magnetic Resonance in Medicine,* 10**,** 118-123.

Liu, S. 2014. *Technical improvements in quantitative susceptibility mapping.*

Liu, S., Buch, S., Chen, Y., Choi, H. S., Dai, Y., Habib, C., Hu, J., Jung, J. Y., Luo, Y. & Utriainen, D. 2017. Susceptibility-weighted imaging: current status and future directions. *NMR in Biomedicine,* 30**,** e3552.

Liu, S., Mok, K., Neelavalli, J., Cheng, Y. C. N., Tang, J., Ye, Y. & Haacke, E. M. 2014. Improved MR venography using quantitative susceptibility-weighted imaging. *Journal of Magnetic Resonance Imaging,* 40**,** 698-708.

Liu, S., Ye, Y., Buch, S. & Haacke, E. Multi-channel data combination with linear phase baseline correction. Proceedings of the 23rd Annual Meeting of ISMRM, 2015. 3309.

Liu, T., Khalidov, I., de Rochefort, L., Spincemaille, P., Liu, J., Tsiouris, A. J. & Wang, Y. 2011a. A novel background field removal method for MRI using projection onto dipole fields. *NMR in Biomedicine,* 24**,** 1129-1136.

Liu, T., Liu, J., De Rochefort, L., Spincemaille, P., Khalidov, I., Ledoux, J. R. & Wang, Y. 2011b. Morphology enabled dipole inversion (MEDI) from a single-angle acquisition: comparison with COSMOS in human brain imaging. *Magnetic resonance in medicine,* 66**,** 777-783.

Liu, T., Wisnieff, C., Lou, M., Chen, W., Spincemaille, P. & Wang, Y. 2013a. Nonlinear formulation of the magnetic field to source relationship for robust quantitative susceptibility mapping. *Magnetic resonance in medicine,* 69**,** 467-476.

Liu, Z., Hansson, A. & Vandenberghe, L. 2013b. Nuclear norm system identification with missing inputs and outputs. *Systems & Control Letters,* 62**,** 605-612.

Lustig, M., Donoho, D. & Pauly, J. M. 2007. Sparse MRI: The application of compressed sensing for rapid MR imaging. *Magnetic Resonance in Medicine: An Official Journal of the International Society for Magnetic Resonance in Medicine,* 58**,** 1182-1195.

Lustig, M. & Pauly, J. M. 2010. SPIRiT: iterative self-consistent parallel imaging reconstruction from arbitrary k-space. *Magnetic resonance in medicine,* 64**,** 457-471.

Ma, Y. J., Liu, W., Zhao, X., Tang, W., Zhang, Z., Tang, X., Fan, Y., Li, H. & Gao, J. H. 2015. Improved adaptive reconstruction of multichannel MR images. *Medical physics,* 42**,** 637-644.

Madhusoodhanan, S., Kesavadas, C. & Paul, J. S. 2019. SWI processing using a local phase difference modulated venous enhancement filter with noise compensation. *Magnetic resonance imaging,* 59**,** 17-30.

Mammen, E. F. 1992. Pathogenesis of venous thrombosis. *Chest,* 102**,** 640S-644S.

Mehemed, T. & Yamamoto, A. 2013. High-pass-filtered phase image: left-versus right-handed MR imaging systems. *AJNR Am J Neuroradiol,* 34**,** E72.

Meng, Y. & Lei, H. 2008. A single-scan T mapping method based on two gradient-echo images with compensation for macroscopic field inhomogeneity. *Magnetic Resonance in Medicine: An Official Journal of the International Society for Magnetic Resonance in Medicine,* 60**,** 1388-1395.

Menon, R. S., Gati, J. S., Goodyear, B. G., Luknowsky, D. C. & Thomas, C. G. 1998. Spatial and temporal resolution of functional magnetic resonance imaging. *Biochemistry and cell biology,* 76**,** 560-571.

Mittal, S., Wu, Z., Neelavalli, J. & Haacke, E. M. 2009. Susceptibility-weighted imaging: technical aspects and clinical applications, part 2. *American Journal of neuroradiology,* 30**,** 232-252.

Nam, Y., Han, D. & Kim, D.-H. 2012. Single-scan R2$*$ measurement with macroscopic field inhomogeneity correction. *Neuroimage,* 63**,** 1790-1799.

Neelavalli, J., Cheng, Y. C. N., Jiang, J. & Haacke, E. M. 2009. Removing background phase variations in susceptibility-weighted imaging using a fast, forward-field calculation. *Journal of Magnetic Resonance Imaging: An Official Journal of the International Society for Magnetic Resonance in Medicine,* 29**,** 937-948.

Nguyen, H. M., Sutton, B. P., Morrison Jr, R. L. & Do, M. N. 2009. Joint estimation and correction of geometric distortions for EPI functional MRI using harmonic retrieval. *IEEE transactions on medical imaging,* 28**,** 423-434.

Noll, D. C., Nishimura, D. G. & Macovski, A. 1991. Homodyne detection in magnetic resonance imaging. *IEEE transactions on medical imaging,* 10**,** 154-163.

Ogawa, S., Lee, T.-M., Kay, A. R. & Tank, D. W. 1990a. Brain magnetic resonance imaging with contrast dependent on blood oxygenation. *proceedings of the National Academy of Sciences,* 87**,** 9868-9872.

Ogawa, S., Lee, T. M., Nayak, A. S. & Glynn, P. 1990b. Oxygenation-sensitive contrast in magnetic resonance image of rodent brain at high magnetic fields. *Magnetic resonance in medicine,* 14**,** 68-78.

Ogawa, S., Menon, R., Tank, D. W., Kim, S., Merkle, H., Ellermann, J. & Ugurbil, K. 1993. Functional brain mapping by blood oxygenation level-dependent contrast magnetic resonance imaging. A comparison of signal characteristics with a biophysical model. *Biophysical journal,* 64**,** 803-812.

Ogg, R. J., Langston, J. W., Haacke, E. M., Steen, R. G. & Taylor, J. S. 1999. The correlation between phase shifts in gradient-echo MR images and regional brain iron concentration. *Magnetic resonance imaging,* 17**,** 1141-1148.

Parker, D. L., Payne, A., Todd, N. & Hadley, J. R. 2014. Phase reconstruction from multiple coil data using a virtual reference coil. *Magnetic resonance in medicine,* 72**,** 563-569.

Peng, X., Ying, L., Liu, Y., Yuan, J., Liu, X. & Liang, D. 2016. Accelerated exponential parameterization of T2 relaxation with model-driven low rank and sparsity priors (MORASA). *Magnetic resonance in medicine,* 76**,** 1865-1878.

Port, J. D. & Pomper, M. G. 2000. Quantification and minimization of magnetic susceptibility artifacts on GRE images. *Journal of computer assisted tomography,* 24**,** 958-964.

Prell, T., Hartung, V., Tietz, F., Penzlin, S., Ilse, B., Schweser, F., Deistung, A., Bokemeyer, M., Reichenbach, J. R. & Witte, O. W. 2015. Susceptibility-weighted imaging provides insight into white matter damage in amyotrophic lateral sclerosis. *PloS one,* 10**,** e0131114.

Pruessmann, K. P., Weiger, M., Scheidegger, M. B. & Boesiger, P. 1999. SENSE: sensitivity encoding for fast MRI. *Magnetic resonance in medicine,* 42**,** 952-962.

Quinn, M., Gati, J., Klassen, L., Lin, A., Bird, J., Leung, S. & Menon, R. 2014. Comparison of multiecho postprocessing schemes for SWI with use of linear and nonlinear mask functions. *American Journal of Neuroradiology,* 35**,** 38-44.

Radwan, M. M., Darwish, R. A., El Nekiedy, A. & Shama, S. A. 2011. Role of magnetic susceptibility weighted imaging in evaluation of brain lesions. *Alexandria Journal of Medicine,* 47.

Rauscher, A., Barth, M., Herrmann, K.-H., Witoszynskyj, S., Deistung, A. & Reichenbach, J. R. 2008. Improved elimination of phase effects from background field inhomogeneities for susceptibility weighted imaging at high magnetic field strengths. *Magnetic resonance imaging,* 26**,** 1145-1151.

Rauscher, A., Barth, M., Reichenbach, J. R., Stollberger, R. & Moser, E. 2003. Automated unwrapping of MR phase images applied to BOLD MR-venography at 3 Tesla. *Journal of Magnetic Resonance Imaging: An Official Journal of the International Society for Magnetic Resonance in Medicine,* 18**,** 175-180.

Rauscher, A., Sedlacik, J., Barth, M., Haacke, E. M. & R. Reichenbach, J. 2005a. Nonnvasive assessment of vascular architecture and function during modulated blood oxygenation using susceptibility weighted magnetic resonance imaging. *Magnetic Resonance in Medicine: An Official Journal of the International Society for Magnetic Resonance in Medicine,* 54**,** 87-95.

Rauscher, A., Sedlacik, J., Barth, M., Mentzel, H.-J. & Reichenbach, J. R. 2005b. Magnetic susceptibility-weighted MR phase imaging of the human brain. *American Journal of Neuroradiology,* 26**,** 736-742.

Reichenbach, J., Jonetz-Mentzel, L., Fitzek, C., Haacke, E., Kido, D., Lee, B. & Kaiser, W. 2001. High-resolution blood oxygen-level dependent MR venography (HRBV): a new technique. *Neuroradiology,* 43**,** 364-369.

Reichenbach, J., Schweser, F., Serres, B. & Deistung, A. 2015. Quantitative susceptibility mapping: concepts and applications. *Clinical neuroradiology,* 25**,** 225-230.

Reichenbach, J. R., Barth, M., Haacke, E. M., Klarhöfer, M., Kaiser, W. A. & Moser, E. 2000. High-resolution MR venography at 3.0 Tesla. *Journal of computer assisted tomography,* 24**,** 949-957.

Reichenbach, J. R., Venkatesan, R., Schillinger, D. J., Kido, D. K. & Haacke, E. M. 1997. Small vessels in the human brain: MR venography with deoxyhemoglobin as an intrinsic contrast agent. *Radiology,* 204**,** 272-277.

Rivera, M. & Marroquin, J. L. 2003. Efficient half-quadratic regularization with granularity control. *Image and Vision Computing,* 21**,** 345-357.

Robinson, S., Grabner, G., Witoszynskyj, S. & Trattnig, S. 2011. Combining phase images from multi-channel RF coils using 3D phase offset maps derived from a dual-echo scan. *Magnetic resonance in medicine,* 65**,** 1638-1648.

Roemer, P. B., Edelstein, W. A., Hayes, C. E., Souza, S. P. & Mueller, O. M. 1990. The NMR phased array. *Magnetic resonance in medicine,* 16**,** 192-225.

Ros, C., Witoszynskyj, S., Herrmann, K.-H. & Reichenbach, J. Reconstruction of phase images for GRAPPA accelerated Magnetic Resonance Imaging. 4th European Conference of the International Federation for Medical and Biological Engineering, 2009. Springer, 803-806.

Rudin, L. I., Osher, S. & Fatemi, E. 1992. Nonlinear total variation based noise removal algorithms. *Physica D: nonlinear phenomena,* 60**,** 259-268.

Samsonov, A. A. & Johnson, C. R. 2004. Noise-adaptive nonlinear diffusion filtering of MR images with spatially varying noise levels. *Magnetic Resonance in Medicine: An Official Journal of the International Society for Magnetic Resonance in Medicine,* 52**,** 798-806.

Schenck, J. F. 1996. The role of magnetic susceptibility in magnetic resonance imaging: MRI magnetic compatibility of the first and second kinds. *Medical physics,* 23**,** 815-850.

Schenck, J. F. & Zimmerman, E. A. 2004. High-field magnetic resonance imaging of brain iron: birth of a biomarker? *NMR in Biomedicine: An International Journal Devoted to the Development and Application of Magnetic Resonance In Vivo,* 17**,** 433-445.

Schofield, M. A. & Zhu, Y. 2003. Fast phase unwrapping algorithm for interferometric applications. *Optics letters,* 28**,** 1194-1196.

Schweser, F., Deistung, A., Sommer, K. & Reichenbach, J. R. 2013. Toward online reconstruction of quantitative susceptibility maps: superfast dipole inversion. *Magnetic resonance in medicine,* 69**,** 1581-1593.

Schweser, F., Herrmann, K., Deistung, A., Atterbury, M., Baltzer, P., Burmeister, H., Kaiser, W. & Reichenbach, J. R. Quantitative magnetic susceptibility mapping (QSM) in breast disease reveals additional information for MR-based characterization of carcinoma and calcification. Proceedings of the International Society for Magnetic Resonance in Medicine, 2011.

Schweser, F., Lehr, B. W., Andreas, D. & Rainer, R. J. 2010. Sophisticated harmonic artifact reduction for phase data (SHARP). *Proceeding Proc GC Intl Soc Mag Reson Med*.

Sehgal, V., Delproposto, Z., Haacke, E. M., Tong, K. A., Wycliffe, N., Kido, D. K., Xu, Y., Neelavalli, J., Haddar, D. & Reichenbach, J. R. 2005. Clinical applications of neuroimaging with susceptibility-weighted imaging. *Journal of Magnetic Resonance Imaging: An Official Journal of the International Society for Magnetic Resonance in Medicine,* 22**,** 439-450.

Sehgal, V., Delproposto, Z., Haddar, D., Haacke, E. M., Sloan, A. E., Zamorano, L. J., Barger, G., Hu, J., Xu, Y. & Prabhakaran, K. P. 2006. Susceptibility-weighted imaging to visualize blood products and improve tumor contrast in the study of brain masses. *Journal of Magnetic Resonance Imaging: An Official Journal of the International Society for Magnetic Resonance in Medicine,* 24**,** 41-51.

Sheelakumari, R., Kesavadas, C., Varghese, T., Sreedharan, R. M., Thomas, B., Verghese, J. & Mathuranath, P. 2017. Assessment of iron deposition in the brain in frontotemporal dementia and its correlation with behavioral traits. *American Journal of Neuroradiology,* 38**,** 1953-1958.

Sheelakumari, R., Madhusoodanan, M., Radhakrishnan, A., Ranjith, G. & Thomas, B. 2016. A potential biomarker in amyotrophic lateral sclerosis: can assessment of brain iron deposition with SWI and corticospinal tract degeneration with DTI help? *American Journal of Neuroradiology,* 37**,** 252-258.

Shmueli, K., de Zwart, J. A., van Gelderen, P., Li, T. Q., Dodd, S. J. & Duyn, J. H. 2009. Magnetic susceptibility mapping of brain tissue in vivo using MRI phase data. *Magnetic Resonance in Medicine: An Official Journal of the International Society for Magnetic Resonance in Medicine,* 62**,** 1510-1522.

Song, S. M.-H., Napel, S., Pelc, N. J. & Glover, G. H. 1995. Phase unwrapping of MR phase images using Poisson equation. *IEEE Transactions on Image Processing,* 4**,** 667-676.

Teboul, S., Blanc-Feraud, L., Aubert, G. & Barlaud, M. 1998. Variational approach for edge-preserving regularization using coupled PDEs. *IEEE Transactions on Image Processing,* 7**,** 387-397.

Thomas, B., Somasundaram, S., Thamburaj, K., Kesavadas, C., Gupta, A. K., Bodhey, N. K. & Kapilamoorthy, T. R. 2008. Clinical applications of susceptibility weighted MR imaging of the brain–a pictorial review. *Neuroradiology,* 50**,** 105-116.

Tong, K. A., Ashwal, S., Holshouser, B. A., Nickerson, J. P., Wall, C. J., Shutter, L. A., Osterdock, R. J., Haacke, E. & Kido, D. 2004. Diffuse axonal injury in children: clinical correlation with hemorrhagic lesions. *Annals of neurology,* 56**,** 36-50.

Trémoulhéac, B. R. 2015. *Low-rank and sparse reconstruction in dynamic magnetic resonance imaging via proximal splitting methods.* UCL (University College London).

Truong, T. K., Chakeres, D. W., Scharre, D. W., Beversdorf, D. Q. & Schmalbrock, P. 2006. Blipped multi gradient-echo slice excitation profile imaging (bmGESEPI) for fast T measurements with macroscopic B0 inhomogeneity compensation. *Magnetic Resonance in Medicine: An Official Journal of the International Society for Magnetic Resonance in Medicine,* 55**,** 1390-1395.

Valentine, H. L., Does, M. D., Marshall, V., Tonkin, E. G. & Valentine, W. M. 2007. Multicomponent T2 analysis of dithiocarbamate-mediated peripheral nerve demyelination. *Neurotoxicology,* 28**,** 645-654.

Vlaardingerbroek, M. T. & Boer, J. A. 2013. *Magnetic resonance imaging: theory and practice*, Springer Science & Business Media.

Vogel, C. R. & Oman, M. E. 1996. Iterative methods for total variation denoising. *SIAM Journal on Scientific Computing,* 17**,** 227-238.

Volkov, V. V. & Zhu, Y. 2003. Deterministic phase unwrapping in the presence of noise. *Optics letters,* 28**,** 2156-2158.

Wachowicz, K. & Snyder, R. E. 2002. Assignment of the T2 components of amphibian peripheral nerve to their microanatomical compartments. *Magnetic Resonance in Medicine: An Official Journal of the International Society for Magnetic Resonance in Medicine,* 47**,** 239-245.

Walsh, D. O., Gmitro, A. F. & Marcellin, M. W. 2000. Adaptive reconstruction of phased array MR imagery. *Magnetic Resonance in Medicine: An Official Journal of the International Society for Magnetic Resonance in Medicine,* 43**,** 682-690.

Wang, D., Li, W.-B., Wei, X.-E., Li, Y.-H. & Dai, Y.-M. 2012. An investigation of age-related iron deposition using susceptibility weighted imaging. *PLoS One,* 7**,** e50706.

Wang, W.-H., Reutens, D. C., Yang, Z., Nguyen, G. & Vegh, V. 2014. Modified human contrast sensitivity function based phase mask for susceptibility-weighted imaging. *NeuroImage: Clinical,* 4**,** 765-778.

Wang, Y., Yu, Y., Li, D., Bae, K., Brown, J., Lin, W. & Haacke, E. 2000. Artery and vein separation using susceptibility-dependent phase in contrast-enhanced MRA. *Journal of Magnetic Resonance Imaging,* 12**,** 661-670.

Wang, Z., Luo, X.-G. & Gao, C. 2016. Utility of susceptibility-weighted imaging in Parkinson's disease and atypical Parkinsonian disorders. *Translational neurodegeneration,* 5**,** 17.

Weisskoff, R. M. & Kiihne, S. 1992. MRI susceptometry: image-based measurement of absolute susceptibility of MR contrast agents and human blood. *Magnetic resonance in medicine,* 24**,** 375-383.

Wink, A. M. & Roerdink, J. B. 2004. Denoising functional MR images: a comparison of wavelet denoising and Gaussian smoothing. *IEEE transactions on medical imaging,* 23**,** 374-387.

Wycliffe, N. D., Choe, J., Holshouser, B., Oyoyo, U. E., Haacke, E. M. & Kido, D. K. 2004. Reliability in detection of hemorrhage in acute stroke by a new three-dimensional gradient recalled echo susceptibility-weighted imaging technique compared to computed tomography: a retrospective study. *Journal of Magnetic Resonance Imaging: An Official Journal of the International Society for Magnetic Resonance in Medicine,* 20**,** 372-377.

Xu, W. & Qiao, S. 2008. A fast symmetric SVD algorithm for square Hankel matrices. *Linear Algebra and its Applications,* 428**,** 550-563.

Yablonskiy, D. A. & Haacke, E. M. 1994. Theory of NMR signal behavior in magnetically inhomogeneous tissues: the static dephasing regime. *Magnetic resonance in medicine,* 32**,** 749-763.

Yang, Q. X., Williams, G. D., Demeure, R. J., Mosher, T. J. & Smith, M. B. 1998. Removal of local field gradient artifacts in T2*-weighted images at high fields by gradient-echo slice excitation profile imaging. *Magnetic resonance in medicine,* 39**,** 402-409.

Ying, K., Clymer, B. D. & Schmalbrock, P. 1996. Adaptive filtering for high resolution magnetic resonance images. *Journal of Magnetic Resonance Imaging,* 6**,** 367-377.

Zhao, F., Noll, D. C., Nielsen, J.-F. & Fessler, J. A. 2012. Separate magnitude and phase regularization via compressed sensing. *IEEE transactions on medical imaging,* 31**,** 1713-1723.

Zhong, K., Leupold, J., von Elverfeldt, D. & Speck, O. 2008. The molecular basis for gray and white matter contrast in phase imaging. *Neuroimage,* 40**,** 1561-1566.

Zhou, D., Liu, T., Spincemaille, P. & Wang, Y. 2014. Background field removal by solving the Laplacian boundary value problem. *NMR in Biomedicine,* 27**,** 312-319.

Zhou, K., Zaitsev, M. & Bao, S. 2009. Reliable two-dimensional phase unwrapping method using region growing and local linear estimation. *Magnetic Resonance in Medicine:*

An Official Journal of the International Society for Magnetic Resonance in Medicine, 62**,** 1085-1090.

LIST OF PUBLICATIONS

JOURNAL PUBLICATIONS

Sreekanth Madhusoodhanan, and Joseph Suresh Paul. "A quantitative survey of GRAPPA reconstruction in parallel MRI: impact on noise reduction and aliasing." Concepts in Magnetic Resonance Part A 44.6 (2015): 287-305.

Sreekanth Madhusoodhanan, Chandrasekharan Kesavadas, and Joseph S. Paul. "SWI post processing using granularity controlled edge-preserved denoising of multichannel GRE images." International Journal of Imaging Systems and Technology 29.3 (2019): 311-322.

Sreekanth Madhusoodhanan, ChandrasekharanKesavadas, and Joseph Suresh Paul. "SWI processing using a local phase difference modulated venous enhancement filter with noise compensation." Magnetic resonance imaging 59 (2019): 17-30.

CONFERENCE PAPERS

Sreekanth Madhusoodhanan, and Joseph Suresh Paul. "A Phase Noise Correction Scheme for Multi-channel Multi-echo SWI processing." In the proceedings of the International Conference on Machine Intelligence and Signal Processing (MISP-2019), Allahabad, September 2019.

Sreekanth Madhusoodhanan, and Joseph Suresh Paul. "On the Choice of Coil Combination Weights for Phase-Sensitive GRAPPA Reconstruction in multi-channel SWI." In Proceedings of 3rd International Conference on Computer Vision & Image Processing (CVIP), Jabalpur, India, September 2018.